

TABLE OF CONTENTS

I	Introduction and Motivation	6
1	Introduction	7
1.1	The Basics of Nuclear Fusion and Tritium Breeding	7
1.2	The Role of Breeding Blankets	11
1.3	Blanket Concept: Solid Breeder	12
1.4	Pebble bed integrity and thermophysics	13
1.5	Scope of the work	16
1.5.1	DEM	17
1.5.2	CFD-DEM	17
1.5.3	Applied CFD-DEM	18
1.5.4	LBM	19
1.5.5	Other kinds of studies and shit	19
II	Literature Review	21
2	Status of Ceramic Breeder Modeling and Analysis	22
2.1	Status of Continuum Modeling Approaches	25
2.1.1	Mechanical constitutive equations	25
2.1.2	Mechanics and heat transfer coupling	28
2.2	Discrete Element Method	29
2.3	Experimental Pebble Bed Thermomechanics Studies	32
2.3.1	Out-of-pile experiments	32

2.3.2	Pebble bed assemblies experiment	39
2.3.3	Other thermomechanics characterization experiments	40
2.4	Pebble Bed Thermomechanics Summary & Framework	41
3	Pebble Interaction Analysis: Theory	44
3.1	Hertz theory for normal contact of spheres	44
4	Pressure drop across packed beds	50
5	Heat transfer in packed beds	51
5.1	Inter-particle heat conduction	53
5.2	Nusselt number for spheres in packed beds	55
5.2.1	Packed bed correlations: Nellis and Klein	56
5.2.2	Packed beds correlation: Whitaker	57
5.2.3	Single pebble correlations	58
5.3	Radiative transfer with neighboring particles	58
III	Methodology	60
6	Modeling Discrete Element Method (DEM)	61
6.1	Background	61
6.2	Particle dynamics	62
6.2.1	Particle kinematics	62
6.2.2	Linear spring-dashpot model	63
6.2.3	Hertzian non-linear spring dashpot model	65
6.2.4	Time integration	66

6.3	Granular heat transfer	67
6.3.1	Thermal expansion	68
6.4	DEM solver	69
6.4.1	Numerical Implementation Overview	69
7	Modeling coupled computational fluid dynamics and discrete element method (CFD-DEM)	71
7.1	Numerical Methodology	71
7.1.1	DEM	72
7.1.2	Volume-averaged CFD Helium	74
7.1.3	Modeling Setup and Procedure	75
8	Modeling lattice-Boltzmann Method (LBM)	77
IV	Cases studied	78
9	DEM studies	79
9.1	DEM study: effective conductivity with disrupted packing	79
9.1.1	Model Setup & Methodology	79
9.1.2	Effective Thermal Conductivity from Analytic Analogy	82
9.1.3	Results	83
9.2	Conclusions	93
10	CFD-DEM studies	95
10.1	Pressure Drop	95
10.2	Effective thermal conductivity from CFD-DEM	95

10.2.1	Stagnant interstitial fluid	95
10.2.2	Purge gas	97
11	LBM studies	101
12	CFD-DEM Application	102
13	Background experimental studies	103
13.1	Elasticity reduction factor	103
13.1.1	Elasticity reduction factor	104
13.2	Strain energy measurements	112
13.3	Linking interactions with strain energy	112
13.3.1	Pebble crushing predictions	115
14	Background numerical studies	116
14.1	Study of Young's Modulus	116
14.1.1	Numerical experiments setup	117
14.1.2	Results	117
14.1.3	Conclusions	121
14.2	Jeffreson correction to lumped capacitance method	122
14.2.1	Lumped capacitance solution for sphere	123
14.2.2	Exact solution for sphere	125
14.2.3	Jeffreson correction for sphere	129
14.3	Pebble failure modeling	133
14.4	Stability study	134
14.4.1	Critical dynamic timestep	134

14.4.2 Critical thermal timestep	136
14.4.3 Simulation acceleration with scaled material properties	137
V Future Work	138
VI Appendices	139
A Sphere with heat generation	140
A.1 Transformations	141
A.2 Solution	142
A.3 Energy	146
B History of solid breeder design	148
References	150

Part I

Introduction and Motivation

CHAPTER 1

Introduction

The thermomechanical loads on solid breeders, etc etc etc. For a fusion power plant to produce electricity and be self-sustaining in terms of its limiting fuel. The feasibility depends on the ability to engineer a device that surrounds the fusion reaction, captures the ejected neutron to breed tritium, allows recovery of that tritium to attain self-sufficiency, and delivers the energy deposited in the blanket as high quality heat into a power cycle to create electricity. Blanket designs of solid breeders have evolved significantly since their introduction in the 1970s. Some features of current breeder designs will be discussed next.

In this chapter we will present some of the basics of thermonuclear fusion of hydrogen and the need to artificially breed tritium. Then we do some of the functions of a solid breeder / the role a solid breeder plays in the fusion power plant. Then introduce the solid breeder as a concept for the blanket. In § 1.4, we will go into more of the physics and engineering behind the need for- and approaches for maintaining- temperature control in a solid breeder. Finally in § 1.5, the scope of this work will be outlined.

1.1 The Basics of Nuclear Fusion and Tritium Breeding

The controlled, sustained thermonuclear fusion of light elements is the ultimate energy source for humanity. Fusion is an energy source that is inexhaustable (on our planetary scales), produces none of the greenhouse gases that are altering the climate of our planet in potentially devastating ways, and avoids many of the dangers of nuclear fission. But overcoming

the engineering obstacles to tame the fusion reaction is the greatest technological challenge of our generation.

The most favorable fusion reaction for first generation fusion reactors involves the two hydrogen isotopes of deuterium and tritium. The deuterium-tritium (DT) reaction has a high reaction probability at the lowest ion temperature with high energy yield. Alternative fusion reactions of two deuterium atoms or a deuterium atom with helium-3 are advantageous in other regards, such as no radioactive byproducts or fuel availability, but their relatively higher ion temperature preclude them from current consideration. The DT reaction proceeds as



Of the two isotopes fused, deuterium (D , or 2H) is a stable isotope and is naturally occurring in an average abundance of 0.015 mole percent in water on Earth. To demonstrate just how plentiful deuterium is as a fuel source, there is approximately 100 million billion kilograms of deuterium in the Earth's oceans. If all energy on Earth were produced from DT fusion power plants, there would be enough deuterium to outlast the lifetime of our sun. We will not run out of peak deuterium.

Tritium (T , or 3H), however, is radioactive with a half-life of only about 12.32 years; any naturally occurring tritium decays at such a rapid pace it will never accumulate to an appreciable amount on Earth. If tritium is to be used as a fuel in a fusion power plant, it must be generated artificially.

A method of in-situ generation of tritium in a fusion reactor is to include a so-called tritium breeding blanket that surrounds the plasma with a phase of lithium. Natural lithium will interact with neutrons as



where we have used the common short-hand of α in place of the helium nucleus. The cross-sections of the lithium reactions are given in Fig. 1.1. Note the exothermic lithium-6

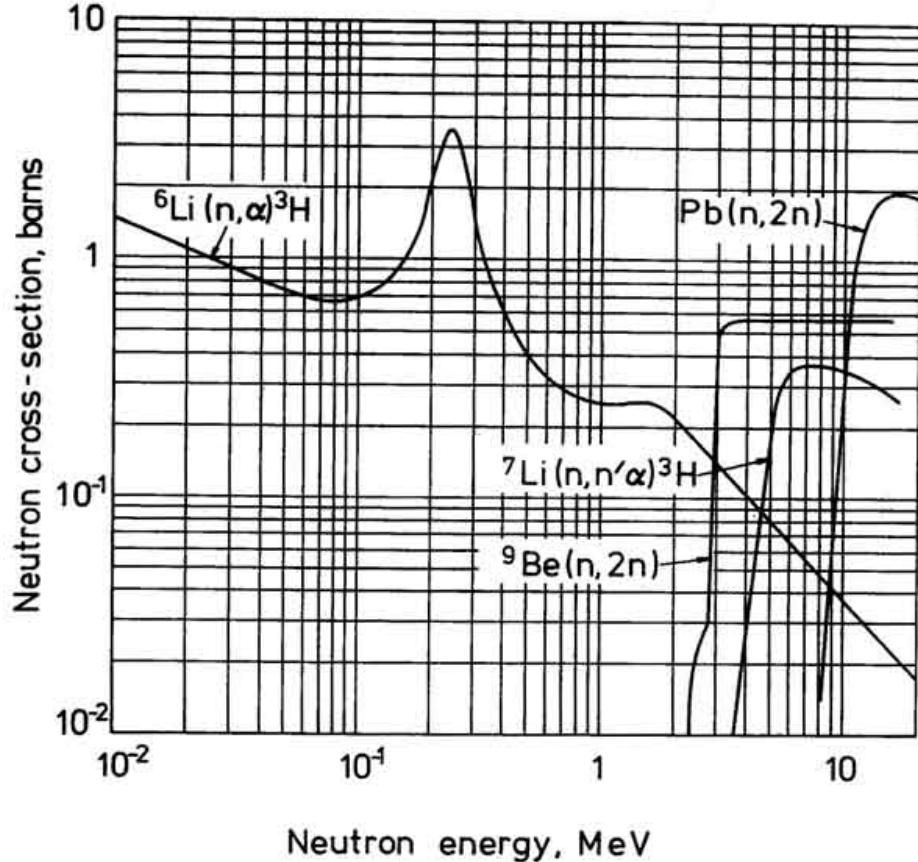


Figure 1.1: Cross-sections of various blanket materials. Note the threshold for the ^7Li and neutron multiplying reactions.

reaction (a neutron of any energy will incite the transmutation) and the threshold energy required of the incident neutron in the endothermic lithium-7 reaction.

Lithium, like deuterium, is quite abundant on Earth. As noted in Francis Chen's book on the fusion, there is enough lithium available on land to generate tritium for 30 million years of DT reactions providing all of humanity's electricity.⁷

To reiterate, neither the fusion reaction of Eq. 1.1 nor the necessary transmutations of lithium in Eqs. 1.2 produce any greenhouse gases. The nature of fusion requires a constant supply of fuel (and extremely careful engineering) to keep the plasma burning; there is no risk of the fusion reactor going into melt-down. For even the first generation fusion reactors, the necessary fuel will last beyond the timeline of humanity on Earth. Furthermore, the

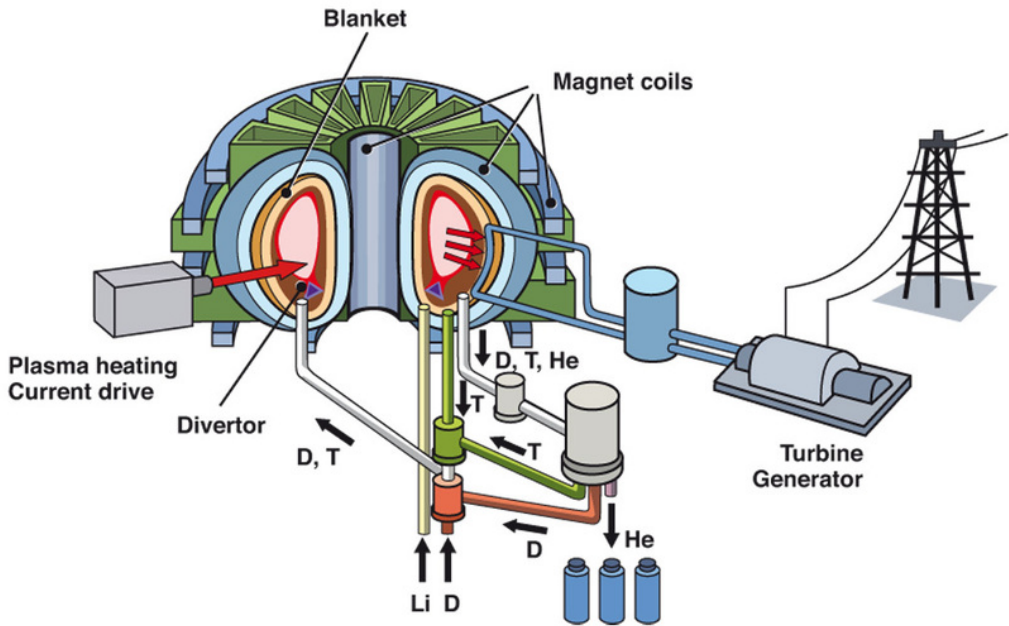


Figure 1.2: Schematic of a tokamak power plant showing the role of the blanket in both energy production and tritium breeding. (reproduced from the Max-Planck-Institut für Plasmaphysik)

next generation fusion reactors will likely move away from tritium and will have virtually no concern of radioactive waste. Fusion power is unarguably the ultimate energy source for humans on Earth and, if we continue to live the lives of comfort we currently enjoy, is in absolutely critical step in humanity's march forward.

In Fig. 1.1, a schematic of a potential magnetically-confined fusion power plant is shown. In the illustration, we see the blanket surrounding the toroidally-shaped plasma and how the tritium generated in the blanket is recycled on-site to be fed back into the burning plasma. Also apparent in the sketch is the role of the breeding blanket as power generator. In § 1.3, we will go into more detail on the complete function of a breeding blanket in a fusion reactor.

1.2 The Role of Breeding Blankets

As was shown in § 1.1, the blanket surrounding the plasma must perform the critical role of breeding tritium from lithium. The measure of a blanket design's effectiveness at breeding tritium is commonly done with the metric of the tritium breeding ratio (TBR). The TBR is defined as the number of tritium atoms produced in the blanket per fusion neutron. When the fusion neutron is ejected it may stream through gaps in the blanket that are necessary for instrumentation, plasma heating, etc. The neutron may also collide with supporting structure or other elements in the breeding material. Due to the neutron leakage and parasitic interactions, only 60-80% of the fusion neutrons may react with lithium. Furthermore, once tritium is actually generated, it is retained in structural material or lost to the fuel cycle simply from inefficiencies in handling. It becomes quickly obvious self-sufficiency of the fuel cycle is clearly not possible unless we produce more than one tritium per fusion neutron.

One scheme for increasing the TBR of breeder blankets is to introduce beryllium as a neutron multiplier. Beryllium has a very high nuclide density while also being very light, with a high melting temperature, and has a high thermal conductivity. The incident neutron smashes beryllium into two α particles and an additional two neutrons. Therefore, in order to breed tritium, the blanket will first generate more neutrons for every neutron spit out by the fusion reaction.

In addition to breeding tritium, the blanket will be responsible for power extraction in the fusion reactor. The blanket must function to capture the kinetic energy of neutrons (80% of the fusion energy is carried by the neutron), secondary γ rays, and the plasma radiation on the plasma-facing first wall (an integral component to the blanket). The blanket must also be able to convert the fusion's energy into high quality heat that can be extracted into the power cycle connected to the fusion reactor.

Finally, the last function of the breeding blanket is to provide radiation shielding of the vacuum vessel and super-conducting magnets that are containing the plasma.

1.3 Blanket Concept: Solid Breeder

Material and Form As each individual tritium breeding region is small, in a typical solid breeder blanket design there are several alternating layers of breeding zone, cooling plate, and neutron multiplier.

TBM unit design

In typical solid breeder modules, coolant fluid runs through the containing structure surrounding the pebble bed. A low-pressure, low-speed purge gas is pumped through the pebble bed to extract the tritium generated and transport it out of the blanket for processing. As nuclear energy is deposited into the poorly-conductive ceramic breeder material, the temperature climbs well above the containing structure. Heat is removed from the pebble bed predominately through inter-particle conduction (with a small contribution from convection of the purge gas) and contact conductance of many pebbles pressed against the containing surface.

The packed bed will be contained in a structure of ferritic or austenitic steel. The energy of the packed bed is carried away by coolant channels in the structure that have flowing in them high pressure helium gas. Because the structural material is held cooler than the breeding zone, it will confine the thermal expansion of the lithium ceramic and lead to mechanical stresses at the points of contact of the individual pebbles in the packed bed. Engineering design issues surrounding this thermal stress is of great concern to researchers and will be the focus of much of this report.

Once in operation, the ceramic pebble beds will have a specified operating temperature window that is dictated by tritium release characteristics. The low end of the temperature window is governed by a minimum temperature for acceptable release rates of tritium from the ceramic to the purge gas; the value is generally set around 300 °C. The upper limit of the temperature window is chosen to avoid sintering of the lithiated ceramic. Sintering of the ceramics, as grains in individual pebbles meld, is predicted to reduce the rate of tritium release. The upper end of the temperature window is generally set around 900 °C.

The size of breeder regions is limited by the temperature window combined with the poor effective conductivity of packed beds of ceramic pebbles. The conductivity is a weak function of external pressure but can generally be approximated as about 1W/mK . Because the effective conductivity and packed bed-wall interface conductance is predominately a contact conduction, disruptions to the packing structure will have considerable impact on the heat transfer of the packed bed.

The fusion reaction deposits a great deal of surface radiation on the first wall of the breeding blanket and the blanket will be absorbing energy deposited from neutron interactions and γ rays. The blanket must be capable of converting and then recovering the energy at high temperatures for efficient power production in the fusion power plant. The nuclear heat generated in the pebble bed solid breeder will heat the ceramic pebbles to maximum temperatures of approximately $900\text{ }^{\circ}\text{C}$. The heat of the pebbles is transported through them via conduction through inter-particle contacts, conduction through the purge gas into neighboring particles, and ultimately through contact with the containing structure. The box structure surrounding the solid breeder will have high pressure (8 MPa in many current designs) helium flowing through channels that remove the heat from the blanket, with the helium reaching temperatures of $500\text{ }^{\circ}\text{C}$, and into a power generation cycle.

1.4 Pebble bed integrity and thermophysics

A common problem plaguing those who study packed beds is the multi-scale of physics dictating the behavior of the packed bed. In the realm of engineering continuum mechanics, packed beds cannot be adequately described as a solid or liquid (or obviously gas) alone. Under compression, a packed bed responds like a solid with non-linear elasticity and a plasticity that is history-dependent. The packed bed can obviously not support any tensile pressure and will often behave like a liquid as it may fill in voids under just the force of gravity. Experiments on packed beds provide effective material properties that are often specific to the material, packing fraction, moisture content, or level of polydispersity.

In packed beds of ceramics for tritium breeding, phenomenological models have been

developed based on the controlled environment of laboratory experiments. The models provide reliable information on the initial states of breeder volumes in the fusion reactor environment and allow reasonable design predictions of the thermomechanics of the breeding blanket. Unfortunately, a certain measurable quantity in an experiment may arise due to vastly different pebble-scale physics. Furthermore, it is unavoidable that other morphological changes of the pebble bed may arise due to individual pebble cracking, inter-particle creep, or inter-particle sintering. Designers of solid breeder blankets must have predictive capabilities for the initiation of morphological changes in the packed bed as well as how those changes impact the thermophysics of the bed.

The solid breeder in many current designs feature sub-module units of packed beds. From the point of view of pebble bed thermomechanical properties, this has the advantage of producing units individually that can be tested and qualified to desired packing states (and therefore thermomechanics) during the design phase.

The thermophysical and thermomechanical properties of pebble beds have been studied extensively [cite many of the experimental papers]. From experimental measurements, and the assumption that a pebble bed can be treated as a continuous media, researchers have developed phenomenological formulas relating properties of pebble bed to other, measurable, macroscopic properties [cite many of the modeling papers]. For instance, an effective thermal conductivity can be given for the packed bed given a certain gas and stress on the bed. These effective material properties are useful for the design and qualification of tritium breeding modules. But it must be understood that the material properties of a pebble bed are a function of their history and will evolve in time as the morphological features of the pebble bed likewise evolve in time. Therefore there is a need to predict the morphological changes to the pebble bed and the subsequent impact on the bed's thermophysical properties so that solid breeder designers may have reliable temperature control of the pebble bed over the duration of the use of the breeder in the reactor.

Stresses in the pebble bed (the origins of the stresses will be discussed in § 1.4) may lead to the cracking or crushing of individual pebbles which disrupts the physical contact

of pebbles and may thereby disrupt the heat transport out of the pebble bed. Even in the absence of crushed pebbles, at the high temperatures expected in the tritium breeding zone, thermal creep between the small contact regions of pebbles may itself alter thermophysical properties

In typical solid breeder modules,

Alleviating any of the issues that may plague the ceramic breeder all boil down to requiring temperature control via an understanding and of the morphological changes of the ceramic packed beds and their interaction with the interstitial purge gas and structural container. In this work we introduce enhancements and new elements to build upon the understanding from ceramic breeder models of past research efforts.

As such, heat transfer out of the pebble bed relies on maintaining strong contact both between pebbles in the bed and pebbles with the container.

The pebble bed will experience a constrained thermal expansion as the hot ceramic pebbles press against the relatively cooler container. The restricted thermal expansion of the pebble bed gives rise to stresses which may crush individual pebbles as the stress at the walls propagates through contact forces between pebbles in the ensemble. With the potential accumulation of many cracked/crushed individual pebbles, the overall packing structure of the pebble bed is altered as they are cracked or crushed packing structure response depends on the extent and modes of cracking and the thermophysical properties likewise change. Second, thermal ratcheting or thermally-induced bed creep can lead to evolutions in thermophysical properties even in the absence of cracked pebbles. Finally, as the thermophysical properties evolve, global or local bed temperatures change and ultimately the tritium release characteristics of the bed deviate from any prediction one may have had from the initial packing of the ceramic pebble bed.

1.5 Scope of the work

To develop a complete numerical model for a pebble bed requires completing many interacting sub-models. To demonstrate, we give here the path of a possible analysis scheme of these models. To begin, one must have knowledge of the interaction of the pebble bed with the containing structure as they exist in a fusion environment. The interactions are generally analyzed via the finite element method to find internal stresses and temperature fields of the entirety of the pebble bed and surrounding container. After the internal fields are mapped into the bed, one would use the discrete element method (DEM) to interpret the macroscopic stress fields into the inter-particle forces. With the inter-particle forces and total absorbed thermal energy calculated, a prediction of the initiation and evolution of morphological changes (i.e. crushed pebbles, sintering, creep, etc.) to each computational volume. Following this, DEM would calculate new effective properties as a result of the morphological changes to the pebble bed region. Finally, the updated bed properties would feed back into the FEM formulation to update calculations in the macroscopic stress fields. A suite of integrated numerical tools that follows this example algorithm is the goal of the Fusion Science adn Technology Center at UCLA, but we are far from that at this time. The work of this dissertation is focused entirely on the development of pebble-scale simulations that are predominately in the realm of the discrete element method.

We aim to provide designers of packed beds with tools to understand how packing states may evolve from time-dependent phenomena (e.g. sintering, creep, pebble cracking, etc.). These phenomena may, for instance: decrease the effective thermal conductivity which will raise bed temperatures beyond initial predictions, produce isolated pebbles which will sinter and potentially decrease tritium release rates, or even form gaps between pebble beds and containing structures leading to divergence from properties of the initial packing of the bed.

Modeling research on ceramic pebble beds should have as its main objective a thorough understanding of the evolution of pebble bed morphology and the impact on thermophysical properties; allowing for temperature control of breeder pebble beds over the entire lifetime of the blanket. To accomplish that goal, this current study is aimed at developing a

methodology for coupling established discrete element models of individual pebbles in the ensemble with thermo-fluid simulations of the interstitial helium purge gas. Specifically, we will address the impact of helium on the thermal transport in a bed experiencing evolving morphology due to cracked pebbles.

Specifically, much of the work in this dissertation concerns the evolution of thermophysical properties of a pebble bed in the presence of crushed individual pebbles. When a pebble in an ensemble is crushed or cracked it loses contact with its neighboring pebbles and subsequently breaks any thermal or mechanical transport that the pebble was providing – ultimately this is manifest in measurable changes to thermophysical properties. We attempt to quantify the evolving thermophysical changes with increasingly sophisticated DEM models of ceramic pebble beds.

1.5.1 DEM

In the first study of § 9, we analyze the effective thermal conductivity of a pebble bed assuming different fractions of pebbles in the ensemble are completely crushed. The focus of this study is to determine the extent of change in aggregate ensemble properties due to individual pebble crushing, relate the changes in effective conductivity to quantifiable pebble-scale properties (e.g. contact force, coordination number, etc.), as well as help designers anticipate acceptable limits of pebble loss from a thermal management point of view. For the DEM tools used in this study, the only mode of heat transfer is conduction between the solid particles.

1.5.2 CFD-DEM

In a fusion breeder, the helium purge gas winding through the interstitial gaps of the pebbles has a substantial contribution to overall heat transfer.^{1,49} The model of § 9 is improved to include the flowing interstitial gas. In § 10, we continue to employ our DEM tools to provide particle-scale information such as contact force, but couple the pebbles to a volume-averaged

computational fluid dynamics (CFD) code. The coupled CFD-DEM model is again used to simulate the heat transfer in packed beds of ceramic spheres that experience pebble crushing – but now investigate the impact of a flowing interstitial helium purge gas when pebbles are crushed.

1.5.3 Applied CFD-DEM

In the study of § 12, we apply our coupled CFD-DEM computational tools to the analysis of ITER-relevant solid breeder geometries. In this study we consider the combined effects of pebble crushing, packing restructuring due to both gravity and the unbalanced force network in the pebble bed, and convection from helium purge gas on temperature profiles in solid breeders for different breeding configurations. In typical solid breeder modules, coolant fluid runs through the containing structure surrounding the pebble bed. Heat is removed from the pebble bed predominately through inter-particle conduction and contact conductance of many pebbles pressed against the containing surface. As such, heat transfer out of the pebble bed relies on maintaining good pebble-pebble and pebble-wall contact. However, physical contact is interrupted to different degrees when a pebble bed responds to various amounts of individual crushed pebbles. Furthermore, the restructuring of the pebble bed after a pebble crushing event is, in part, dependent on gravity forces acting upon each pebble in the ensemble. We investigate two representative pebble bed configurations where heat is removed from the bed via inter-particle conduction, convection of purge gas, and contact between the pebble bed and its container. In the first, the coolant containing structural walls (heat transfer walls) are oriented parallel to the gravity vector. In the second configuration, the heat transfer walls are perpendicular to the direction of gravity. To simulate a crushed pebble, we replace the pebble with many smaller, non-cohesive elements while maintaining mass-conservation between the original solid pebble and crushed fragments. The fragments are then free to resettle into interstitial gaps and the rest of the bed resettles as determined by forces from gravity, contact of neighboring particles, and even the small influence of the moving purge gas. The thermofluid interaction with the helium purge gas will be included

with volume-averaged Navier-Stokes and energy equations. The representative solid breeder volumes will be compared with respect to their temperature peaks and profiles and how those temperatures vary as a function of the percentage of crushed pebbles in the ensemble. The results can be used to optimize solid breeder pebble bed designs through the choice of breeding zone orientation relative to the gravity vector.

1.5.4 LBM

The models used to account for helium purge gas in the studies of §§ 10 and 12 assume effective drag or heat transfer coefficients for pebbles in a computational volume and then include the pebble influence through effective source/sink terms in the momentum and energy equations. The volume-averaged approach allows for simpler meshing of the fluid volume while still retaining much of the physical realism of the system. Complete models of the conjugate heat transfer of both the fluid moving through the tortuous interstitial gaps pebble beds pressing each other with small contact areas are intractable with current computational hardware and finite-element modeling techniques. To overcome deficiencies in computational power, in § 8, we apply the lattice-Boltzmann algorithm to our pebble bed with helium. The lattice-Boltzmann method (LBM) is a non-traditional fluid simulation technique that allows us to resolve pebble-scale interactions with bed-scale conjugate heat transfer with flowing gas on realistic simulation time scales. The LBM approach is applied to the same pebble beds analyzed in § 10 to provide comparison between the two modeling techniques. Furthermore the LBM model, accounting for the complex helium purge gas pathways, provides more insight to the influence of helium on the heat transfer in the heat transfer of packed beds.

1.5.5 Other kinds of studies and shit

§ 13 § 14

In Part II (§§ 3 to 5) we survey the state of the art in analysis of ceramic pebble beds, contact mechanics, and modeling thermal and mechanical interactions of packed beds. In

Part III (§§ 6 to 8) we outline the numerical methodology of the models and tools used in this study, namely: the discrete element method (DEM), coupled computational fluid dynamics and the discrete element method (CFD-DEM), and an integrated lattice-Boltzmann method (LBM). We employ our physics knowledge and numerical tools to cover a range of studies in Part IV (§§ 9 to 11 and 13). Finally, in Part V, we discuss the future of the current work and any limitations or interesting work that was beyond the scope of this dissertation.

Part II

Literature Review

CHAPTER 2

Status of Ceramic Breeder Modeling and Analysis

Ceramic breeders, by their nature, are brittle and prone to cracking under external mechanical loadings. These breeders, in the form of packed beds of pebbles, are loaded into a box-like structure for tritium fuel production in a fusion reactor. When subjected to nuclear heating in a reactor, a strong mechanical loading arises from the differential thermal expansion between breeder pebbles and their containing structure. Research efforts have therefore been aimed at developing a thorough understanding and characterization of the ceramic breeder pebble bed thermomechanics. Such an understanding is essential to providing confidence in the performance and lifetime of a ceramic breeder blanket design. In particular, a significant effort of the pebble bed thermomechanics study is on the development of modeling simulation tools.

Reimann, et al. have conducted an extensive experimental study of the stress-strain relations of the ceramic breeder pebble beds using an oedometric test apparatus.^{?, ?, 48–50} The most significant macroscopic experimental phenomena witnessed in the pebble bed are an irreversible plastic strain when the load is removed, a non-linear elasticity, a pressure-dependent plasticity, and a volumetric creep. A particularly noticeable feature, clearly demonstrated in Fig. 2.1, is the reduced amount of irreversible strain when subjected to additional loading cycles after the first unloading. This may suggest the existence of a semi-equilibrium packing state in the pebble bed which can be reached after applying a pre-load to account for the large strain in the first cycle of a pebble bed. This semi-equilibrium packing state is a feature which may be advantageous for use in a fusion reactor.

To study the temperature effect in Reimann’s studies, the bed is freely heated to the

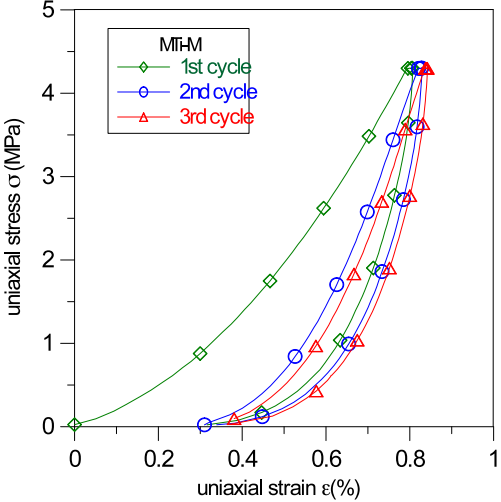


Figure 2.1: Example of uniaxial compression testing results for lithium metatitanate pebble bed.[?]

desired working temperature before the pressure load is applied. Under the same loading condition, the bed behaves much softer at higher temperatures. The bed stiffens as the pressure increases. An illustration of this phenomenon is presented in Fig. 2.2 for a lithium orthosilicate pebble bed between 50 – 850°C. At higher temperatures (such as > 650°C), a creep-like behavior becomes apparent. The creep behavior allows the pebble bed to relax and sustain higher stresses, however one needs to avoid sintering. The data was used to correlate creep rate as a function of temperature, stress, and time for both lithium orthosilicate, lithium metatitanate, and beryllium pebble beds.^{?,8,50}

Phenomenological models, derived from the volumes of collected data, have been proposed to describe the aforementioned mechanical behavior of the pebble beds with a conventional continuum-based approach. The continuum approach allows treatment of the pebble beds with standard finite element modeling (FEM). To employ FEM, mathematical models written in terms of average quantities and containing effective parameters are used. These models deduce a set of constitutive equations to be implemented in the framework of a finite element code. There are two major variants of phenomenological modeling approaches developed among institutions, including: (1) A non-linear elastic model and a modified Drucker-

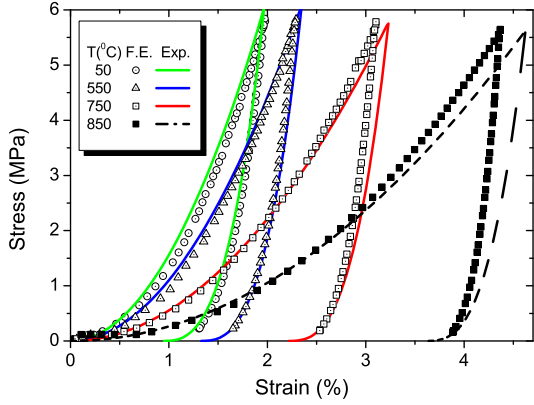


Figure 2.2: Example of uniaxial compression testing results compared with predictions from material constitutive equations for lithium orthosilicate pebble beds at different temperatures.²³

Prager-Cap theory for plastic strain;^{?,²²} and (2) A hyperporous non-linear elastic model and a Gurson model for plastic model.^{?,²³,¹⁶} The readers are referred to the additional efforts used in a third method[?] which employed two different elasticity laws for the loading and unloading branches but will not be discussed here. Alongside the development of the modeling techniques, several large scale pebble bed thermomechanics experiments were conducted in parallel. These experiments were intended to reveal the underlined thermo-mechanical characteristics of ceramic breeder pebble beds, and provide data for benchmarking the developed models. The validation statuses as well as the features of the models are briefly described in the following section.

Another modeling strategy is to model the pebble bed as a system of distinct interacting bodies that are subject to forces and resulting motions. This modeling approach called discrete element modeling (DEM) considers the mechanical interaction between pebbles and numerically solves the associated equations of motion.^{?,²⁴,²⁵,²⁶,²⁷} The DEM approach has recently received increased attention and the progress will be summarized to follow.

The review of the current status of development on the ceramic breeder pebble bed

thermomechanics is organized as follows. In Section 2, current continuum modeling approaches and constitutive models for mechanical and thermal interactions are presented. In Section 3, a review of recent advancements on DEM is presented. A brief discussion on recently-initiated benchmarking efforts, in-pile experimental results, and other experimental observations relevant to pebble bed thermomechanics are given in Section 4. A proposed framework and a few conclusions on the outlook are drawn in Section 5.

2.1 Status of Continuum Modeling Approaches

2.1.1 Mechanical constitutive equations

Continuum models focus on predicting global behavior, including volumetric strain and stress and the impact on the effective thermal conductivity, etc. Two institutions in Europe have spearheaded modeling efforts. One being Karlsruhe Institute of Technology, formerly FZK and referred to as such throughout this paper, and the other being ENEA-Brasimone with the Department of Nuclear Engineering at the University of Palermo, referred to as DIN throughout this paper. These two institutions have published a great deal of detail in regards to the specific details of their modeling techniques and the reader is referred to these publications for the fine points of the models.^{?, ?, 17, 22} The discussion here calls attention to differences between models and attempts to serve as a reference basis for future modeling efforts.

The models from FZK and DIN share a common treatment of the mechanical interaction between the pebble beds with structural walls. In models from the two institutes, interfacial contact and friction forces are taken into account by application of the Coulomb friction law. This frictional contact law can be simply implemented in finite element code without considerable computation effort.

2.1.1.1 FZK mechanical model

In the FZK approach, the corresponding phenomenological constitutive models were developed based on the soil mechanics models implemented in the finite element code ABAQUS. This includes a non-linear elasticity model, which was originally developed for powder die compaction; a plastic strain model via a modified Drucker-Prager-Cap model, which was originally developed for soil mechanics; time-dependence via a consolidation creep law; and global thermal-mechanical coupling from material parameters.

The Drucker-Prager-Cap model captures the plasticity of the pebble beds and predicts the yielding and hardening behavior. A feature of the classic Drucker-Prager-Cap model, as implemented in ABAQUS, is the ability to describe the plastic behavior of pebble beds under hydrostatic compression; a feature which is not present in classical metal plasticity models. However, researchers at FZK recognized that for materials with large creep strain amplitudes (e.g. beryllium pebble beds), hardening laws defined by default in ABAQUS were insufficient. Therefore, unique hardening laws were developed and implemented in place of the standard equations referenced in ABAQUS. An advantage gained from the redefined hardening laws is their capture of the creep behavior witnessed in pebble beds at high temperatures. The disadvantage of the Drucker-Prager-Cap model is the computational resources necessary for convergence of solutions. This has so far limited the FZK model to spatially two-dimensional simulations.

The main distinguishing feature unique to the continuum model developed in FZK is in their treatment of the material parameters that feed into the models described above. In particular, the hardening law in the model is manipulated to accommodate direct fitting to the oedometric tests. Unlike other continuum models, which require a trial-and-error method of optimizing numeric elasto-plastic parameters, the FZK model can be directly and clearly linked to experimental data. In this way, the model may be most adept at predicting behavior of a pebble beds where stress and temperature fields are very different from the controlled experiments which produced the constitutive relationships.^{?, 22, 24, 26}

2.1.1.2 DIN mechanical model

The mechanical model established in the DIN model similarly assumes a non-linear elasticity model and a plasticity model. The non-linear elastic model assumes that during the reversible straining of a pebble bed, its effective logarithmic bulk modulus depends on the equivalent pressure according to a hypothesized power law. From this assumption as the foundation, DIN proceeds through a semi-theoretical derivation to relate the bed deformation modulus to the equivalent pressure; and stress state to volumetric strain. Included in the derivation are a number of effective parameter values. Values of all material parameters are chosen on an iterative trial-and-error basis until the model agreed well with the non-linear, elastic curves seen in oedometric experiments.

Attempting to resolve large computing time required when using the Drucker-Prager-Cap model for plastic deformation, DIN instead used a Gurson model. The Gurson model was originally developed for the analysis of pressure-dependent plastic behavior of mildly voided materials. The Gurson model postulates that the pebble bed behavior can be modeled as a continuous matrix in which stochastically-distributed voids are contained. In the Gurson model, compaction-related plastic deformation of the bed can be reproduced. For material parameters in the Gurson model, again an iterative procedure was used until the model reproduced the results of relevant experimental tests. Lastly, in the consideration of the effective hardening law in pebble beds, a fifth order polynomial function was hypothesized. It should be noted that in the model's current form, it is incapable of directly capturing the creep behavior of pebble beds. However, the model was designed such that a future creep law could readily be implemented.^{?, ?, 17}

The main advantage of the approach taken by DIN in their model is apparent when considering computational demand. DIN is currently able to model three-dimensional experiments with modest computer time. The most apparent drawback is the ad-hoc procedure of determining effective parameters used in the model. Without a direct link to experimental data, the applicability of the chosen effective parameters at predicting behavior beyond the

range of the experimental conditions is unknown.

2.1.2 Mechanics and heat transfer coupling

Maintaining the breeder temperature within its temperature window is crucial for predictable performance and lifetime of the breeder unit. Proper temperature analysis requires careful characterization of thermal properties of the pebble beds.

The pebble-bed experiments demonstrated that the effective thermal conductivity depends on the volumetric compressive strain; changes in thermal conductivity occurred between compacted and un-compacted systems. These measured phenomena indicate that thermo-mechanical modeling must also consider full, non-linear coupling between thermal and mechanical analysis.

The thermal models of the two institutions are fundamentally similar. The form of thermal model used by FZK follows from the experimental work carried out by J. Reimann from FZK in which empirical equations have been reported where the temperature and volumetric inelastic strain-dependence is incorporated into the bulk thermal conductivity. The thermal conductivity for a lithiated ceramic pebble bed over a specified range of temperature is reported in Ref.²² as:

$$\begin{aligned} k (W/m \cdot K) = & 1.81 + 0.0012 T - 5 \times 10^{-7} T^2 + \\ & + (9.03 - 1.386 \times 10^{-3} T - 7.6 \times 10^{-6} T^2 + \\ & + 2.1 \times 10^{-9} T^3) \epsilon \end{aligned} \quad (2.1)$$

where T and ϵ are the local temperature and strain, respectively. The formula for thermal conductivity owes its functional form to the widely used Schlunder, Zehner, and Bauer (SZB) model. The coefficients in Eq. (2.1) are empirically derived from experiments. The FZK model has linked its constitutive equations directly to experimental data.

In the DIN thermal model, the effective thermal conductivity has a quasi-linear dependence on volumetric strain and temperature. DIN reports the equation for determining

thermal conductivity in Ref.,⁷ it is:

$$k \text{ (W/m} \cdot \text{K)} = \lambda_0 (1 + \gamma T + \delta \epsilon) \quad (2.2)$$

where T and ϵ are the local temperature and strain, respectively. The relationship of Eq. (2.2) introduces several effective parameters, λ_0 , γ , and δ , that are determined from iterative fits to experimental data. Values of these effective parameters have been determined thus far for beryllium and certain lithium orthosilicate pebble beds.¹⁷ The thermal conductivity, being a function of both thermal and mechanical parameters endows the models with a full coupling between thermo-mechanical analyses.

2.1.2.1 Thermal interface model

The thermal interaction at the interface between pebble bed and containment wall is represented in both models as an effective heat transfer conductance, with only slight variations between the two approaches. In the FZK model, the thermal interaction is simulated with an effective heat transfer coefficient. The heat transfer coefficient (HTC) incorporates the combined effects of radiation heat transfer, pebble-solid conduction, and solid-gas heat transfer. Furthermore, in the event of a gap formation at the interface between pebble bed and containing surface, a separate heat transfer coefficient is employed. The researchers at DIN noted that interface conductance is affected by parallel paths of heat flow: pebble-wall conduction at contact areas and gas-wall convection. DIN therefore posits that the macroscopic phenomena can be modeled as a pressure-dependent thermal gap at the interface. They therefore have a thermal interface conductance that is a function of temperature, pressure, and local volumetric strain. An iterative trial-and-error method was also used to determine the effective parameters in this term.

2.2 Discrete Element Method

Discrete Element Method (DEM) introduced by¹⁵ has been shown to be a promising tool to study the behavior of granular systems through the interaction between the individual

particles. DEM has been used successfully to study the micromechanical aspects of pebble bed thermo-mechanics in the past.^{7,8} Furthermore, DEM can be used to establish a relation between the microscopic interactions and the macroscopic response of the granular assemblies. Reference⁷ studied the pebble assemblies in rectangular and cylindrical containers bounded by elastic walls. The effect of packing factor, geometry of the assembly on the overall stress-strain response under uni-axial compression tests (UCT) has been thoroughly investigated.⁷ have studied similar pebble assemblies in a cubic box with periodic boundary conditions. In both the above studies, a non-linear stress-strain response and a characteristic residual strain after unloading (analogous to plastic strain in continuum systems) has been observed akin to the experimental results.⁷ It has been shown that the average coordination number, average normal contact force and the maximum normal contact force in the assembly has a unique functional relation (nonlinear, linear and linear, respectively) with the hydrostatic pressure or the applied pressure independent of the packing factor.^{7,2} These functional relations may be used as master curves for the micro-macro correspondence in the pebble bed thermo-mechanics studies. A first attempt to include the creep mechanism in DEM has been made by² showing the experimentally observed phenomenon such as the reduction of creep strain rate over time under constant load, albeit qualitatively. Further advances in the thermo-mechanics of pebble beds using DEM are under progress at KIT and UCLA in collaboration with experiments.

Recently, the effect of the pebble size distribution on the overall thermo-mechanical behavior of the pebble assembly is studied by⁷ considering the pebble size distribution of ceramic breeder pebbles (Orthosilicate (OSi) pebbles) with a diameter range of 0.25 mm-0.65 mm. Figure 2.3 shows a binary pebble assembly in a periodic box. The colors indicate stored elastic strain energy of the pebble (red: maximum and blue: zero). The assembly has a maximum pebble radius $r_g = 0.25$ mm with the pebble size ratio $r^* = r_s/r_g = 0.6$, relative volume fraction $V^* = V_g/V = 0.7$ and a packing factor $\eta = 0.643$. The average stress in a granular assembly can be deduced from the contact forces between individual grains.

Another aspect of interest in the study of mechanics of pebble beds is the crush behavior

of individual pebbles and their impact on the over all pebble bed response. DEM is used to study the behavior of a crushable pebble assembly with the crush load data for OSi pebbles (for individual pebbles) measured at KIT for pebbles of diameter 0.5 mm.

A probabilistic method for analyzing the crush events of individual pebbles and a procedure with the combination of DEM and experimental data to obtain crush load probability has been reported by.⁷ Figure 2.4 shows the cumulative distribution function as a function of the hydrostatic pressure placed on the bed. The probability analysis, derived from DEM calculations, provides quantitative report of pebble crushing as a function of a specific hydrostatic pressure. The results of this analysis exemplify the growing strength of DEM techniques for analyses connecting global pebble bed loads to individual pebbles.

However, it has been shown^{?,68} that a criterion based on critical stored elastic energy is the most suitable criterion for describing the OSi pebble failure. Hence, the crush load data (provided by fusion materials laboratory at KIT) has been transformed into equivalent elastic strain energy showing a Weibull distribution.⁶⁸ This critical energy (randomly generated distribution) is used as the criterion for failure of pebbles in the DEM simulations. First, the assembly is loaded up to 3% strain in uniaxial compression and then unloaded to a stress-free state. The elastic modulus of the pebble is reduced (from initial value to a small value of 1 kPa) with increase in elastic strain energy of the pebble according to a phenomenological damage accumulation law.[?] The damage state is frozen at the end of loading step and hence there will be no further damage accumulation in the unloading step.

Figure. 2.5 shows the results for two types of damage law each with three different realizations. Each realization corresponds to a different random distribution of critical energies assigned to the pebbles in the assembly. The results do not show appreciable sensitivity to random distribution of energies. In the case of gradual damage law, the reduction of the elastic modulus of the pebble starts when the stored elastic energy reaches 50% of the critical energy for that pebble and the elastic modulus reaches exponentially to its minimum value when the stored elastic energy reaches the critical energy prescribed. In the case of sudden damage this reduction starts at a much later stage when the stored elastic energy

reaches 95% of the critical energy of the pebble. Clearly, the assembly with a sudden damage accumulation shows a higher maximum strength compared to the gradual damage. In the case of the gradual damage, the pebbles start to degrade much earlier (at small strain) than in the case of sudden damage. Hence the critical number of pebbles to fail for the onset of maximum strength is reached earlier (at small strain) in gradual damage. It turns out that a mere 0.2% pebbles is the critical number for the onset of maximum strength (stress plateau) observed.

The nature of damage evolution influences the maximum strength and strain at which the maximum strength is attained while the critical number of failed pebbles for this saturation is independent of the damage evolution law (also see⁶⁸). Also note that the high frequency oscillations during loading in the stress-plateau region represent the failure of new pebbles. The current analysis also shows a creep-like behavior of the stress-strain response and hence the stress-plateaus observed in the experiments⁷ may indicate the presence of pebble crushing in addition to the thermal creep mechanism. Furthermore, the residual strain after unloading is large for the system with sudden damage than the system with gradual damage. It should be noted that the assembly with gradual damage has more number of damaged pebbles at the end of loading (at 3% strain) making the assembly more compliant than in the case of sudden damage.

2.3 Experimental Pebble Bed Thermomechanics Studies

2.3.1 Out-of-pile experiments

The constitutive equations developed for finite element models were derived from the uniaxial compression experiments, which are not fully representative of fusion operating conditions. A more prototypical experiment should subject a pebble bed to isostatic loading. This could be generated by either an in-pile pebble bed experiment or by making use of differential thermal expansion between a pebble bed and its containing structure. The latter has been

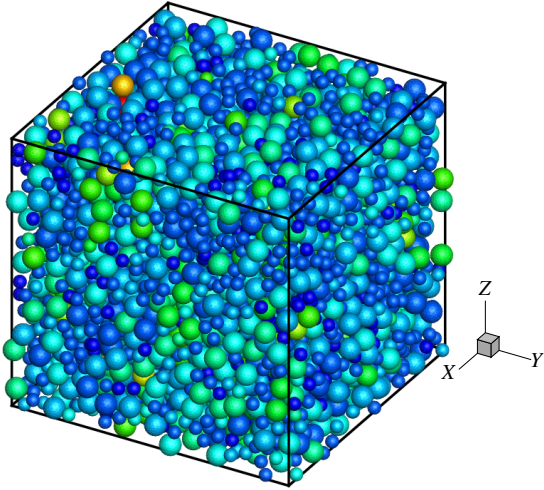


Figure 2.3: (color online) A binary pebble assembly with $r^* = 0.6$ and $V^* = 0.7$ showing the stored elastic energy of the pebbles at $\epsilon_{33} = 1.5\%$; pebbles of radius r_s (small) and r_g (large).

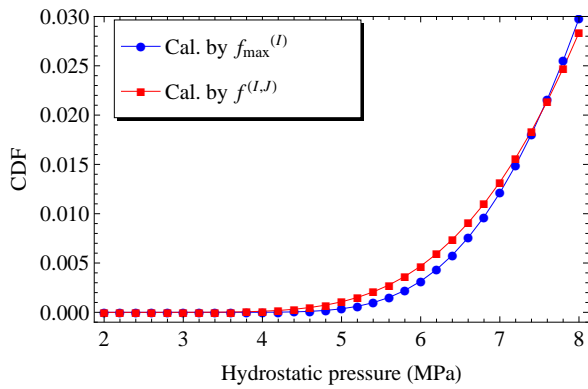


Figure 2.4: (color online) Cumulative distribution functions for crushing of individual pebbles inside the bed for as-fabricated pebbles, calculated by (1) maximum contact forces and (2) all inter-particle contact forces.[?]

attempted with several out-of-pile experiments launched by the HE-FUS 3 facility at ENEA Brasimone. The experiments investigated the thermo-mechanical behavior of pebble beds within geometry much more representative of current breeder designs. These include the medium-scale mock-up exercises of HELICA (HE-FUS3 Lithium Cassette) and HEXCAL-

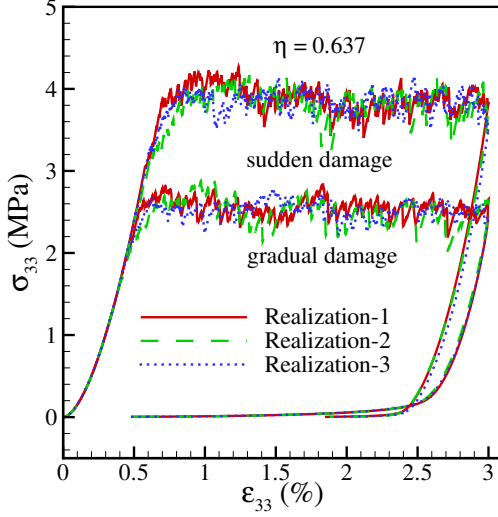


Figure 2.5: (color online) Stress-Strain response of a granular assembly under uni-axial compression for two different damage evolution laws (gradual and sudden). Each damage evolution criterion is simulated with three different realizations of randomly prescribed critical failure energy for individual pebbles following Weibull distribution.

IBER (HE-FUS3 Experimental Cassette of Lithium Beryllium Pebble Beds).^{?,16} For those experiments, the pebble layers are heated by electric heaters, and temperature and displacement were measured.

2.3.1.1 FZK Benchmarking

FZK has performed validation of their FEM code against the data collected from the HELICA experiment.²³ They have also reported the results of simulations of HEXCALIBER but have, as yet, not directly validated against the collected experimental data.²⁴

In the HELICA experiment, the pebble beds experienced six thermal ramps, each applied for an hour, and then the pebble beds were actively cooled with a helium flow. After cooling, the pebble beds were subjected to the another thermal ramp and the process was repeated. DIN reports[?] that the pebble bed temperatures exhibited cyclical behavior. FZK simulated two cycles of the HELICA test and an example of the calculated results and experimental

data are shown in Fig. 2.6 and Fig. 2.7. In Fig. 2.6 we see temperature histories at a particular location (100 mm from the first wall) during a loading-unloading cycle. The simulation results follow the temperature increase during the thermal ramps up until the seventh hour, then again follow the experimental data as the test rig is cooled with the helium coolant. Even with the two-dimensional simplification of the model, there is excellent agreement between calculations and measurements. In Fig. 2.7 the displacement calculated by FZK is also in strong agreement with the average of measured displacements for the entire duration of the heating-cooling cycle. Because of the overwhelming amount of computer time necessary for the FZK model to complete a fully three-dimensional and transient simulation, the FZK computations of HELICA and HEXCALIBER are carried out in two dimensions; the helium temperature is chosen at an average value of measured inlet and outlet temperatures.

From FZK's numeric simulation arise several important observations: (i) a three-dimensional analysis would provide more detail, spatial temperature variation of e.g. coolants would likely explain much of the deviation between temperature profiles predicted by the simulation and measured in the HELICA experiment; (ii) gap formations, with sizes on the order of a pebble diameter, were detected at the interface of the first wall in ceramic beds; (iii) the maximum hydrostatic pressures seen in the ceramic bed are anticipated to be above the fracturing limit of the lithium ceramic. The consequences of some of these observations, if true and real, are severe enough that they merit careful attention. Gap formation and pebble failure (crush or fracturing) are important topics that must be considered in validation with future experiments.

2.3.1.2 DIN Benchmarking

Because of the characteristics of the DIN model, full three-dimensional simulations were capable of being relatively easily performed. In the framework of benchmarking efforts, DIN has performed validation of their model against experimental results of HELICA, shown in Fig. 2.8 as well as HEXCALIBER, shown in Fig. 2.9.

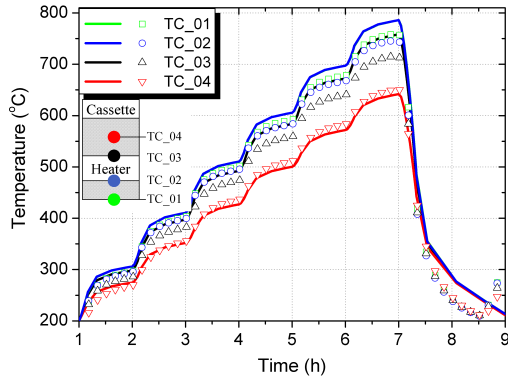


Figure 2.6: Results of the FZK benchmarking with HELICA²⁴ showing temperature variations with time during a loading cycle (T in $^{\circ}\text{C}$) at 100 mm from FW.

The results of the DIN model show also strong agreement to the experimental results of HELICA as demonstrated in one example of temperature histories shown in Fig. 2.8. In this profile, the same location as that modeled by FZK (100 mm from the first wall) is simulated by DIN. The FEM simulations from DIN (Fig. 2.8) are reported over the six-hour heating portion of a single heating ramp cycle of HELICA. When comparing the results from DIN with those of FZK (in Fig. 2.6 and Fig. 2.7) we see the DIN model has slightly better predictive capabilities for the temperature histories. This may be due attributed to the three-dimensional variations in coolant temperature being captured by the DIN model.

Unfortunately, the ambitions of HEXCALIBER were limited due to the crippling of several heaters. Nevertheless, the limited data was still used in efforts to validate the constitutive relationships of the DIN model. The temperature variations with time were the only major result reported by the ENEA Brasimone team, such as that shown in Fig. 2.9; mechanical results are still forthcoming from the research group. From the comparisons to experimental measurements in HELICA and HEXCALIBER it is encouraging to notice that even in the absence of a creep model, satisfactorily close agreement were seen between computation and measurement. So far, no detailed displacement comparisons have been made to experimental data.

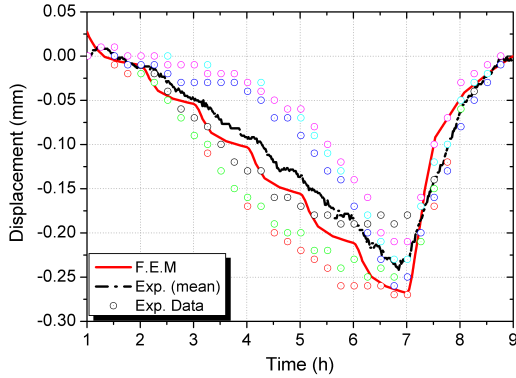


Figure 2.7: Results of the FZK benchmarking with HELICA²⁴ showing a comparison of displacements (in mm) in HELICA between calculated and measured LVDT values.

Several important observations are also made from the results of the DIN simulation: (i) three-dimensional effects were important to calculations of the convective energy transport of the helium coolant; future models should continue to be analyzed in three-dimensions; (ii) DIN reports that in HELICA all ceramic beds experience a compressive force everywhere and no gap formation is ever detected.

In summary, the benchmarking efforts have only recently begun in Europe. A typical pebble bed thermomechanics simulation involves first calculating overall temperature fields of the blanket unit as it undergoes volumetric nuclear heating as well as cooling at the boundaries. The non-linear mechanical analysis is then performed for stress and strain estimations. However, since the effective thermal conductivity of the ceramic breeder pebble bed is, to some degree, dependent on strain, a coupled thermal and mechanical analysis is needed. Additional details on modeling steps can be found in Refs.^{?, ?, 16, 17, 24, 26} The two most developed models, from FZK and DIN, have had their results compared to experimental data and have thus far shown great promise.

However, it must be noted that the benchmarking efforts are incomplete and inconsistencies between the two models must be explained as they move forward. For example, the model of FZK concluded that a gap appeared between the pebble bed and structural wall,

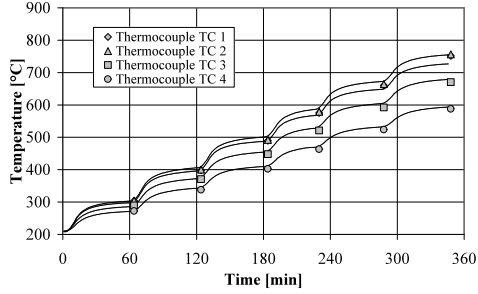


Figure 2.8: Exemplary results of the DIN benchmarking with HELICA: Temperature variations with time during a loading cycle at 100 mm from FW.?

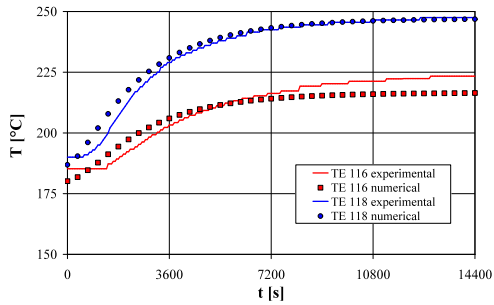


Figure 2.9: Exemplary results of the DIN benchmarking with HEXCALIBER : Temperature variations with time during a loading cycle within the first lithium-orthosilicate cell.?

however the model from DIN reported no gap formation. The existence of a gap between pebble bed and structural wall will negatively affect the ability to cool the pebble bed and thereby impact structural and tritium release properties of the bed. That such a discrepancy exists between calculated results of the models on such a critical feature warrants either more benchmarking efforts or a careful deconstruction of the constitutive equations to discover the source of the inconsistency. Future experiments aimed at benchmarking ought to focus on creating apparatus capable of expressing, among other things, when gap formation or pebble failure occurs.

2.3.2 Pebble bed assemblies experiment

The pebble bed assemblies (PBA) experiment is designed to study the effect of neutron irradiation on the thermo-mechanical behavior of a ceramic breeder pebble-bed under DEMO representative thermo-mechanical loads.^{?, ?, ?} This was accomplished via analysis of changes of the in-pile temperature profiles during irradiation as well as from the post irradiation examination of the pebble bed in the Hot Cells. Within the assemblies, there are four test elements; each resembling a small-scale mock-up of a HCPB TBM with a ceramic breeder pebble bed sandwiched between two beryllium pebble beds. Before irradiation, the beds are pre-compacted with a compressive load of 3 MPa to ensure good settling and contact.

FEM analysis was performed to study pre-compaction procedures. During progressive irradiation, temperatures are recorded at several locations in the ceramic breeder bed as well as other critical positions. Reviewing the recorded temperature data, when comparing the temperature in the center of the ceramic breeder pebble bed during later cycles and earlier cycles there appears to be a decrease in temperature for the exact same environmental conditions. Changes in the pebble beds and their characteristics are examined both in-pile by neutron radiography and out-of-pile by e.g. SEM during post-irradiation examination (PIE). The estimated bed height reduction from neutron radiographies over the course of the irradiation has shown 3% of creep compaction.

A pebble bed experiencing creep compaction is both becoming more dense as well seeing more-developed inter-pebble conduction paths. The effective thermal conductivity for a creep-compacted ceramic pebble bed is thus expected to be higher than a standard ceramic pebble bed. This phenomenon results in lower temperature gradients and a lower overall temperature magnitude, which is precisely what was observed in the experiment over the course of the cycling.

During PIE, various microscopy preparation techniques are used to study the deformation state of the pebble beds (signs of creep compaction and sintering), formation of gas gaps between the pebble beds and structural materials, and the interaction layers between eurofer-

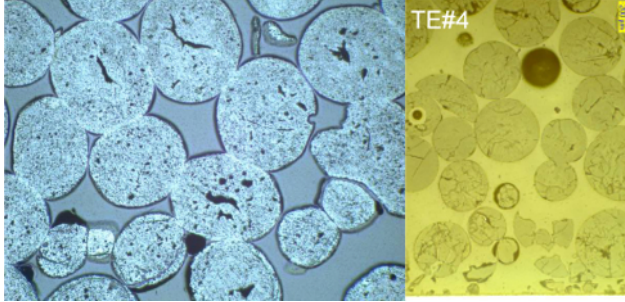


Figure 2.10: Notable features of irradiated Li_2TiO_3 and Li_4SiO_4 pebble beds from PBA.[?] (Left) Demonstration of significant sintering of Li_2TiO_3 pebbles with no fracturing; the visible cracks originated from production and handling. (Right) Demonstration of cracking of Li_4SiO_4 pebbles.

ceramic and eurofer-beryllium.

Figure 2.10 shows the cross-section of Li_2TiO_3 pebbles (left) and Li_4SiO_4 pebbles (right) post irradiation. Evident in the images is sintering of the lithium titanite and significant fracturing of the lithium orthosilicate pebbles. Importantly, however, it must be noted that the pebble beds performed reliably in spite of the changes displayed in these images.[?]

2.3.3 Other thermomechanics characterization experiments

Coming from the standpoint that strain in a pebble bed is induced by thermal expansion, an experiment was conducted to characterize the pebble bed thermal expansion coefficient.[?] The thermal expansion coefficient of a packed Li_2TiO_3 pebble bed is measured under a compressive load of 0.1 MPa. The study concludes that for beds with packing factors of 65.3 to 68.5%, the average thermal expansion coefficient was $(1.4 \pm 0.2) \times 10^{-5} K^{-1}$. This thermal expansion coefficient of the pebble bed was equal to 78% of that for the bulk material under the conditions used in the study. The reduction in thermal expansion coefficient is less significant than that of the effective modulus, which is more than 2 orders of magnitude smaller than the bulk value.

The effect of thermal cycling on the packing state is of interest; in particular, it is foreseen

that the ITER TBM will be subjected to such conditions. The question that arises is whether a void region will be created under thermal-cyclic loading due to the differential rates of expansion and contraction of the pebble bed and structural containing wall. This uncertainty was first addressed in an experimental set-up involving Li_2TiO_3 pebbles enclosed by two Kovar flanges while sandwiched between two commercial-grade CVD silicon carbide discs.⁹ The set-up allows for generating a high stress through large differential in thermal expansion coefficients. The experimental results indicate that high thermal stresses and deformations are present during the initial thermal cycle of the assembled test article, but are successively alleviated due to a combination of pebble re-arrangement within the bed and creep induced deformation. This suggests that a few thermal cycles under a controlled atmosphere and a compressive load before final assembly of blanket sections would mitigate the severity of the thermal stresses during start-up. This is also shown in a later experiment, in which the increment of compression decreased with each heating cycle and became negligible after 30 cycles.⁵⁵ Extrapolating the finding to a prototypical blanket breeder pebble bed design, the study concludes that for a height of 1 m long pebble bed, a 51 mm high cavity may be generated at the top of the bed with an initial packing of 65% under thermal cyclic operations.

2.4 Pebble Bed Thermomechanics Summary & Framework

The progress already achieved holds the promise of a pebble bed thermomechanics framework that will contribute substantially to the success of the ceramic breeder blanket development. In this framework, the continuum modeling approach using FEM and empirically derived material constitutive equations is capable of correctly characterizing the stress load to which a breeder pebble bed unit may be subject during the operations as shown in Fig. 2.11. The DEM approach analyzes this load and determines the possibility fraction of pebble cracking based on the crush load data of pebbles or the degree of sintering depending on the local

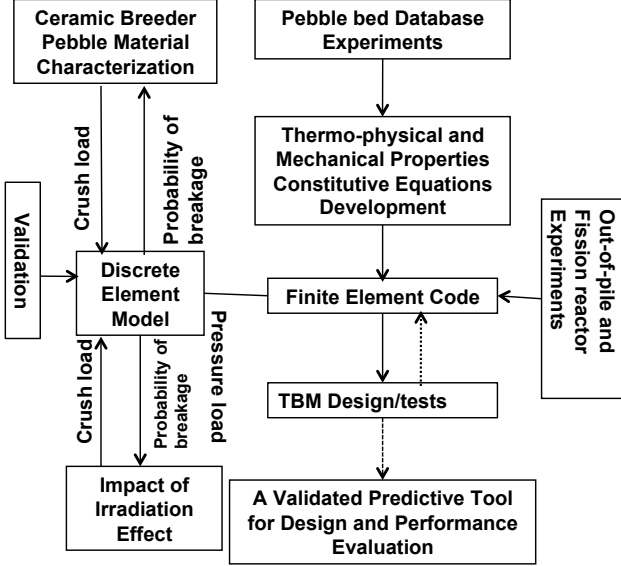


Figure 2.11: Example Pebble Bed Thermo-mechanics Research Framework.

contact stress. The combined analyses warrants a high confidence of success to the assembly and design of breeder units in a blanket. Experiments should also be conducted to assess the manner of pebble relocations and packing rearrangement when pebble cracking occurs. Since there is no perfect packing state, it is important to learn if the breeder unit will continue to function in accord with the original design goals under all complex operating conditions. The ultimate objectives of the pebble bed thermomechanics include to delineate a near-equilibrium packing state as the initial state, quantify breeder unit thermomechanics parameters during operations, understand how these properties vary as packing state alters and the degree of variation, and ensure breeder functions as it is intended to in the fusion operational phase spaces.

This leads to a more reliable blanket design. The analysis has preliminarily defined what peak stress values the breeder unit may be subjected to under the operations (e.g. $< 2 - 3$ MPa for Li_4SiO_4 or < 5 MPa for Li_2TiO_3). Since creep will lead to stress relaxation, further development incorporating creep models for high temperature DEM simulation is desired. This may increase the peak stress margin if stress relaxation is taken into account. Despite the scale of the experiments conducted so far, validation experiments are still necessary in

regards to current continuum FEM models. Moreover, validation and refinement of simulations with regards to pebble damage crush properties are desired in particular in view of damage mechanisms. There may be merits to perform crush load tests for irradiated pebbles at operating temperature ranges (room to 850/900 °C). It holds forth promising on the continued pebble bed thermomechanics study in fine details a higher confidence to the ceramic breeder lifetime performance in a blanket. The quest is to define and search a persistent ceramic breeder packing state throughout the blanket lifetime.

CHAPTER 3

Pebble Interaction Analysis: Theory

In § 6.2, we will lay out the contact interaction mechanics implemented in the discrete element method which include normal and tangential forces and damping. While all the mechanics are important for the fidelity and stability of the DEM simulation, we will focus here purely on the normal elastic contact of two interacting bodies, the analysis which was first performed by Heinrich Hertz in 1882. The results of the so-called Hertzian contact law is vital to many other sections of this work so it is instructive to have the analysis laid out.

3.1 Hertz theory for normal contact of spheres

[DRAW SOME COORDINATE DIAGRAMS TO SHOW HOW Z R AND X-Y WHAT-EVER ARE ACTUALLY RELATED AND CAN BE VISUALIZED] We consider two non-conforming solids approaching and then contacting under load. Picture a line connecting the centerpoints of the two bodies and an $x - y$ plane existing at the midpoint between the bodies and oriented normal to their connecting line. On that surface, there is a radius, r extending from the connecting line that is related to the $x - y$ coordinates as $r^2 = x^2 + y^2$.

Because we are restricting ourselves to two spheres, the surface of curvature of the two bodies may be written as

$$z_1 = \frac{1}{2R_1}r^2 \quad (3.1a)$$

$$z_2 = \frac{1}{2R_2}r^2 \quad (3.1b)$$

respectively. As the two bodies approach, just before the surfaces are in contact, points on the two surfaces are separated by a distance $h(r)$,

$$\begin{aligned} h &= z_1 - z_2 \\ h &= \left(\frac{1}{R_1} + \frac{1}{R_2} \right) \frac{r^2}{2} \end{aligned} \quad (3.2)$$

Noticing this term in the separation, we define the relative radius of curvature as

$$\frac{1}{R^*} = \frac{1}{R_1} + \frac{1}{R_2} \quad (3.3)$$

and then the separation is simply $h = (1/2R^*)r^2$.

The two bodies continue their approach towards each other until finally, under an external load F , come into contact. The cross-section of these bodies after contact are shown in Fig. 3.1. If we first imagine that the two surfaces do not interact and their surfaces pass through each other unimpeded, their surfaces would be overlapped to a distance δ . In such a case, we examine two points deep within the bodies, along the axis of contact, calling them T_1 and T_2 . These points will have moved δ_1 and δ_2 , respectively. The total overlap is obviously related to these displacements by $\delta = \delta_1 + \delta_2$.

However, under actual interaction, the two surfaces are going to deform as the load F presses them into contact. So now we consider two points on the surfaces, such as S_1 and S_2 . Before contact, these two points are initially separated by a distance h (from Eq. 3.2), then displace by \bar{u}_{z1} and \bar{u}_{z2} due to contact pressure.

If the points S_1 and S_2 are inside of the contact region under load, these distances are related by

$$\bar{u}_{z1} + \bar{u}_{z2} + h = \delta \quad (3.4)$$

Then using Eq. 3.2, we have an expression for the elastic displacements as

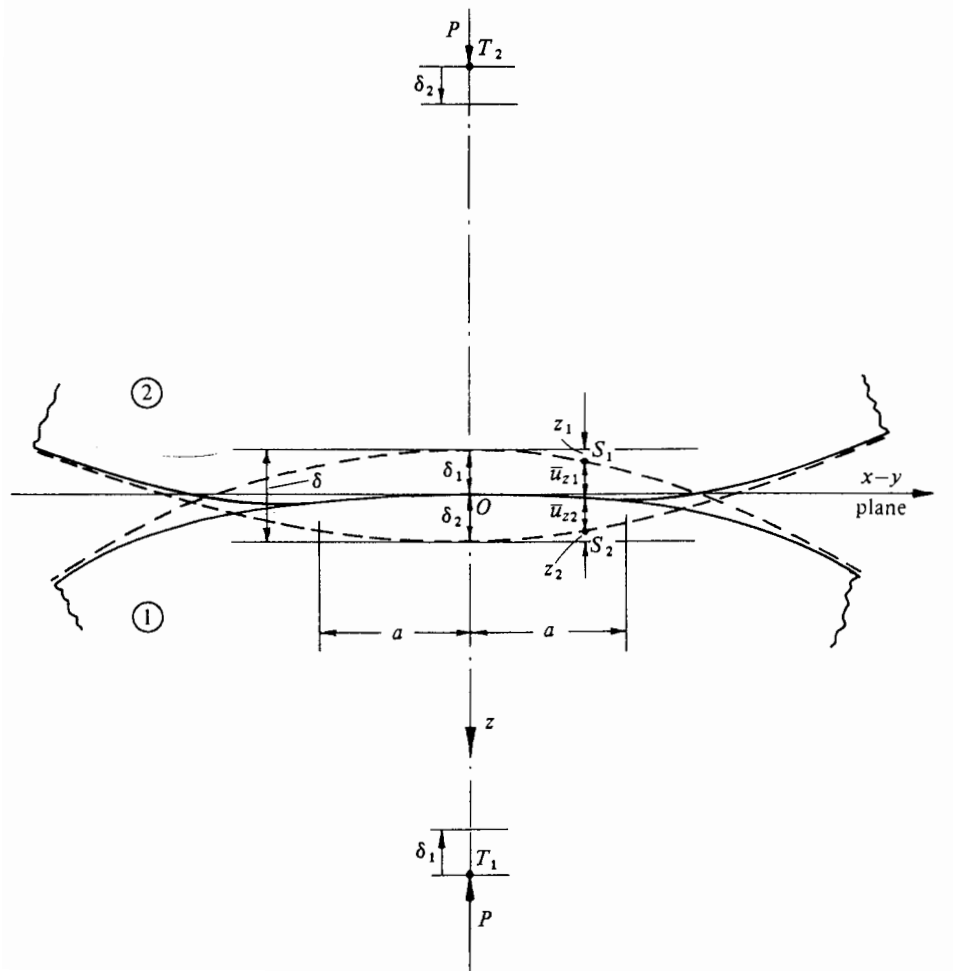


Figure 3.1: default

$$\bar{u}_{z1} + \bar{u}_{z2} = \delta - \frac{1}{2R^*} r^2 \quad (3.5)$$

Alternatively, if after deformation the points S_1 and S_2 are outside of the contact region, this is simply

$$\bar{u}_{z1} + \bar{u}_{z2} > \delta - \frac{1}{2R^*} r^2 \quad (3.6)$$

It now is necessary to find a pressure distribution that satisfies these boundary conditions of displacement. Hertz's great contribution was to simplify the solution of expressions

Eqs. 3.5 and 3.6 by regarding each body as an elastic half-space upon which the load is applied over a small, elliptical region (the contact area). This simplification allows for treatment of the highly concentrated stresses near the region of contact without consideration of either the general response of stresses in the bulk of the body or the manner in which they are supporting the load. This assumption is justifiable if the dimensions of each body as well as the relative radii of curvature are very large compared to the contact area. These assumptions are sufficient to proceed with the analysis, but the curious are pointed to an excellent discussion and background of Hertz's theory as given in KE Johnson's textbook.³²

For solids of revolution, a distribution of pressure to satisfy the displacements of Eq. 3.6 is proposed by Hertz as

$$p = p_0 \left[1 - \left(\frac{r}{a} \right)^2 \right]^{1/2} \quad (3.7)$$

where a is the radius of the contact area.

The total load, F is found from the pressure distribution as

$$\begin{aligned} F &= \int_0^a p(r) 2\pi r \, dr \\ F &= \frac{2}{3} p_0 \pi a^2 \end{aligned} \quad (3.8)$$

From the distributed load over the circular region, stresses and deflections are found from superposition of point loads. The pressure is integrated (see Ref.³²) to find the normal displacement for either solid body as

$$\bar{u}_z = \frac{1 - \nu^2}{E} \frac{\pi p_0}{4a} (2a^2 - r^2) \quad (3.9)$$

This is applied to both bodies and plugged into Eq. 3.5 to yield

$$\frac{\pi p_0}{4a E^*} (2a^2 - r^2) = \delta - \left(\frac{1}{2R^*} \right) r^2 \quad (3.10)$$

where we have introduced the now-common term of pair Young's modulus,

$$\frac{1}{E^*} = \frac{1 - \nu_1^2}{E_1} + \frac{1 - \nu_2^2}{E_2} \quad (3.11)$$

for simplification.

With the solution of Eq. 3.10, if we consider $r = a$ and $\delta(a) = 0$, we find the radius of the contact circle is

$$a = \frac{\pi p_0 R^*}{2 E^*} \quad (3.12)$$

and when $r = 0$, we find the overlap as

$$\delta = \frac{\pi a p_0}{2 E^*} \quad (3.13)$$

and alternatively we find the pressure as a function of overlap

$$p_0 = \frac{2 E^* \delta}{\pi a} \quad (3.14)$$

The radius, overlap, and pressure relations are inserted into Eq. 3.8 to find the force (from now on referred to as the Hertz force) as a function of overlap, relative radius, and pair Young's modulus,

$$F = \frac{4}{3} E^* \sqrt{R^*} \delta^{3/2} \quad (3.15)$$

as a last step, to differentiate the force from other terms to be derived later, we specify it as the normal force between sphere i and sphere j as

$$F_{n,ij} = \frac{4}{3} E_{ij}^* \sqrt{R_{ij}^*} \delta_{n,ij}^{3/2} \quad (3.16)$$

Equation 3.16 defines the normal contact forces between any two contacting, elastic spheres. This extremely important result acts as the basis of all discrete element method

codes since the concept was first introduced for granular materials by Cundall & Strack in 1979.¹⁵

It is very appealing to use the Hertz force in a numerical model such as DEM because there are very few assumptions built in to the theory; the material must be elastic and satisfy

$$\frac{a}{R^*} \ll 1 \quad (3.17)$$

In which case the force of Eq. 3.16 is calculated from material and geometric properties alone and no phenomenological, empirical fits are necessary.

CHAPTER 4

Pressure drop across packed beds

CHAPTER 5

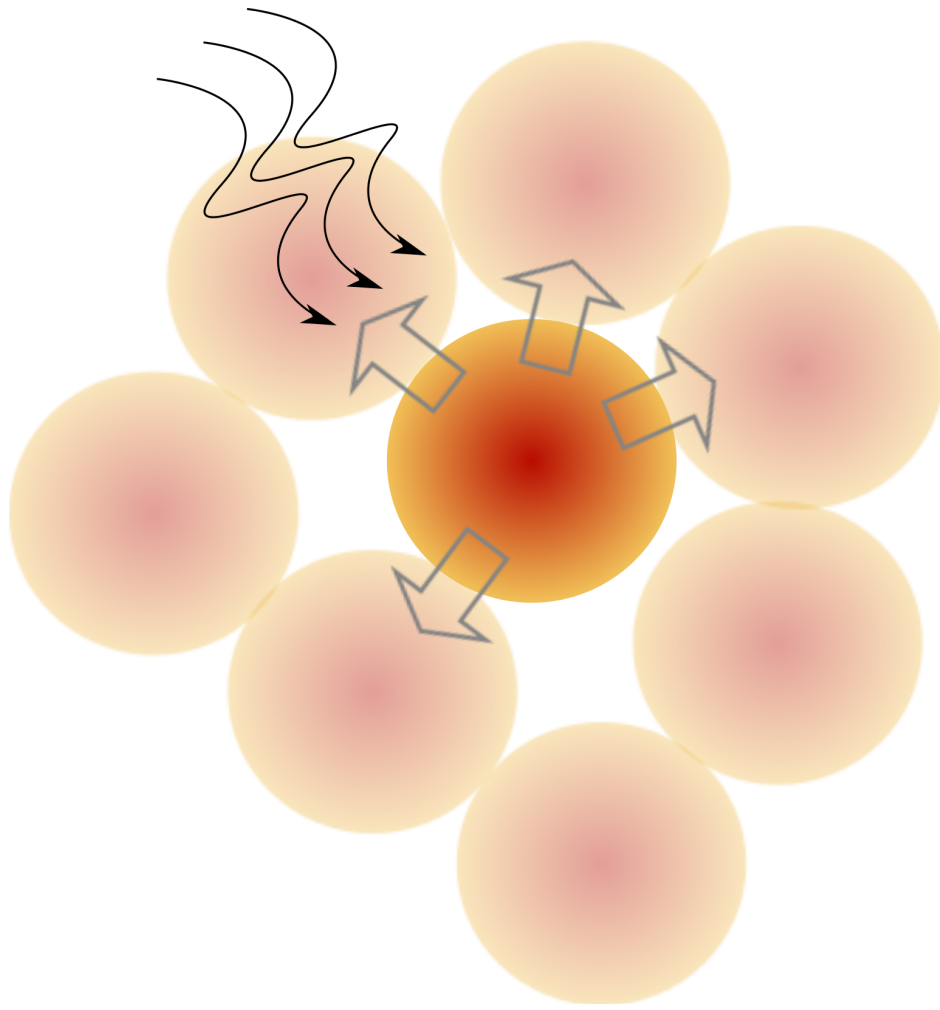
Heat transfer in packed beds

To begin this section, we begin with a general discussion on the thermal interaction of a single particle inside the packed beds of tritium solid breeders of a fusion reactor. In Fig. 5.1, the different modes of heat transfer are drawn.

1. Conduction through the contact area between contacting particles.
2. Conduction through the stagnant fluid between near, non-contacting particles.
3. Conduction through the stagnant fluid between contacting particles.
4. Conduction through the interstitial fluid.
5. Advection of the fluid to contacting- and downstream particles.
6. Radiation between the surfaces of contacting particles.
7. Radiation between particles of adjacent voids.
8. Heat generation internally in the particle.

The first mode of transfer will be addressed in § 5.1 where we will go through the development of a form of heat conductance between contacting, elastic spheres. Ideally, modes 2-5 would each receive separate treatment but we will wrap up all of their influences with heat transfer coefficients that are functions of local packing fraction to account for both the fluid and the neighboring particles; this is done in § 5.2. For the present study, we will entirely neglect the modes 6, and 7 because of their added complexity. Finally, the last mode of heat transfer is trivially accounted for with a heat source term,

Figure 5.1: Each ceramic pebble in a fusion reactor will experience multiple modes of heat transfer.



$$Q_g = q'''V \quad (5.1)$$

where q''' is a known volumetric heating rate and V is the volume of our particle. In practice, we will know a volumetric heating rate from the location and geometry of the solid breeder volume. The volume of the sphere is $V = \frac{4}{3}\pi R^3$.

In the following sections we will expand upon the details of the modes of heat transfer considered for our packed beds. They forms of equations used will be written in a way to be implemented directly into the DEM computational framework, to be discussed later in § 6.

5.1 Inter-particle heat conduction

When two particles come into contact, energy is transmitted through their region of contact. For this discussion, we assume the particles are spherical, elastic, in vacuum, and we neglect radiation transfer between them. The resistance to heat flowing between the two objects is quantified through a contact conductance, H_c . The amount of energy passing between the two particles (labeled i and j) is then

$$Q_{ij} = H_c(T_i - T_j) \quad (5.2)$$

where each contacting pair has a specific value of H_c . We note that the heat conductance, unlike standard heat transfer coefficients, has units of W/K.

Batchelor and O'Brien⁴ developed a formulation of similar form and then made the brilliant observation that the temperature fields in the near-region of contacting spheres are analogous to the velocity potential of the an (incompressible, irrotational) fluid passing from one reservoir to another through a circular hole in a planar wall separating the two reservoirs. With the analogy, they could make use of the fluid flow solution to write the total flux across the circle of contact as Eq. 5.2 with the heat conductance as

$$H_c = 2k_r a \quad (5.3)$$

where k_r is the conductivity of the contacting solids and a is the radius of contact. In § 3.1, with Hertz theory we found the contact radius in terms of the contact pressure. Here, we give the radius in terms of the compression force acting on the bodies,

$$a = \left(\frac{3}{4} \frac{R^*}{E^*} \right)^{1/3} F_n^{1/3} \quad (5.4)$$

as before, $\frac{1}{E^*} = \frac{1-\nu_1^2}{E_1} + \frac{1-\nu_2^2}{E_2}$ and $\frac{1}{R^*} = \frac{1}{R_1} + \frac{1}{R_2}$.

In Eq. 5.3, Batchelor and O'Brien had assumed the two contacting spheres to be of equal conductivity, k_r . Cheng, et al.¹² proposed a slightly modified conductance which allows for

contacting materials of different thermal conductivity. They have,

$$H_c = 2k^*a = 2k^* \left(\frac{3}{4} \frac{R^*}{E^*} \right)^{1/3} F_n^{1/3} \quad (5.5)$$

where $\frac{1}{k^*} = \frac{1}{k_i} + \frac{1}{k_j}$. As well as being a more general, flexible formulation, the models analyzed by Cheng, et al.¹² are in good agreement with experiments. In the DEM numerical structure, we use the form given by Eq. 5.5.

Batchelor and O'Brien developed Eq. 5.3 with the assumption of two contacting particles in vacuum but, once developed, showed⁴ that this form is still valid when immersed in a fluid providing that the thermal conductivity ratio of solid and fluid is well above unity. The condition is expressed as,

$$\frac{k_r}{k_f} \frac{a}{R^*} \gg 1 \quad (5.6)$$

The term $\frac{a}{R^*}$, from § 3.1, is necessarily much less than 1 for Hertz theory to be applicable. Thus for fluid in vacuum, the condition is identically satisfied but we must consider inaccuracies if we introduce an interstitial fluid with low conductivity ratios.

For lithium ceramics in helium, the ratio is approximately $\frac{k_r}{k_f} \approx 10$ which is not necessarily large enough to satisfy the requirement of Eq. 5.6.

As we step back from the contact of a single pair of particles and consider a particle in an ensemble with many contacts, we must again consider the validity of applying Eq. 5.5 at each contact. [give a better description here of why this equation is valid] Vargas and McCarthy,⁶² proposed introducing a conduction Biot number to relate resistance to heat transfer internal to the particle with the resistance between particles. We use the following form

$$\text{Bi}_c = \frac{H_c}{k^* d_p} = 2 \frac{a}{d_p} \quad (5.7)$$

Then if $\text{Bi}_c \ll 1$, the individual energy transferred between each point of contact can be decoupled. The Biot number criteria is already satisfied for Hertz theory to be valid; having

assumed that $\frac{a}{d_p} \ll 1$. Therefore the total heat transferred out of a single particle with Z contacts is summed from the individual contacts as

$$Q_i = \sum_j^Z Q_{ij} \quad (5.8)$$

The form of contact conductance used in our study, built upon the solution of Batchelor and O'Brien,⁴ has been implemented by others in a variety of studies.^{10, 12, 61, 71} However, in many other fields, the researchers are interested in such things as the parallel conduction through a stagnant interstitial gas⁷ or the temporary conduction during impact of fluidized beds.^{38, 64, 67, 73} In such cases, the formula for conductance can be quite different.

Nevertheless, for the packed beds of ceramic spheres we intend to model, the heat conductance of Eq. 5.5 is an appropriate and valid form. When we incorporate the influence of an interstitial gas, it will be done in such a way as to leave the DEM heat transfer intact and only add an energy source term to stand in for the interaction with the fluid. The details will be discussed in § 7.1.1, but for now we conclude with a solid conduction theory that will be implemented in the discrete element method computations.

5.2 Nusselt number for spheres in packed beds

Historically, in the treatment of packed beds for heat transfer, engineers developed relationships between overall heat transfer coefficients to the log-mean temperature of the bed. The Nusselt number correlation was applicable to the bed overall rather than any discrete particle inside of the bed. The correlations will be useful for validating our models of helium flow through packed beds of lithium ceramics.

Recently, however, experimental and numerical research has focused on the heat transfer at the scale of a particle as a component of dilute or dense packed beds. These correlations will be useful for applying to single discrete elements in our DEM framework.

$$Q_{\text{convection}} = -hA_r(T_r - T_f) \quad (5.9)$$

where T_r is the temperature of the solid with surface area, A_r , and T_f is the local bulk temperature of the passing fluid.

5.2.1 Packed bed correlations: Nellis and Klein

A heat transfer coefficient for a packed bed of spheres, as given by Nellis and Klein, is determined strictly on geometric details of the packed bed. Necessary values are the porosity, or void fraction, ϵ , and the cross-sectional surface area of the bed, A_t .

The average heat transfer coefficient is correlated in terms of the Colburn j_h factor.

$$j_h = \frac{\bar{h}}{GC_f} \text{Pr}^{2/3} \quad (5.10)$$

The mass flux, G , is evaluated in terms of the specific surface area and mass flow rate:

$$G = \frac{\dot{m}}{\epsilon A_t} \quad (5.11)$$

where C_f is the specific heat capacity of the fluid and Pr the Prandtl number of the fluid. For a packed bed of spheres, Nellis & Klein used the modified Reynolds number suggested by Kays and London (1984), defined as,

$$\text{Re}_G = \frac{4Gr_{char}}{\mu_f} \quad (5.12)$$

where μ_f is the viscosity of the fluid. The characteristic radius r_{char} is given as:

$$r_{char} = \frac{\epsilon d_p}{4(1 - \epsilon)} \quad (5.13)$$

where d_p is the average diameter of the packed bed particle. The relationship between Colburn j_h factor and mass-flux Reynolds number was provided in Nellis and Klein. The interpolation of their data yields a functional relationship of,

$$jh = 0.191 \text{Re}_G^{-0.278} \quad (5.14)$$

Therefore, the heat transfer coefficient is found as,

$$h = (0.191 \text{Re}_G^{-0.278}) \left(\frac{\dot{m}}{\epsilon A_t} \right) C_f Pr^{-2/3} \quad (5.15)$$

which is applicable for spherical objects in densely packed beds.

5.2.2 Packed beds correlation: Whitaker

Definition of Reynolds number

$$\text{Re} = \frac{D_p G}{\mu_b (1 - \epsilon)} \quad (5.16)$$

Definition of Nusselt number

$$\text{Nu} = \frac{h D_p}{k_f} \frac{\epsilon}{1 - \epsilon} \quad (5.17)$$

Definition of h

$$h_{\ln} = \frac{\dot{Q}}{a_v} V \Delta T_{\ln} \quad (5.18)$$

where $a_v = (A_p/V_p)(1 - \epsilon)$ is the surface area per unit volume. And δT_{\ln} is the log-mean temperature difference.

Reference temp, T^*

$$T^* = \frac{1}{2}(T_{f1} + T_{f2}) \quad (5.19)$$

Range of Reynolds number $22 - 8 \times 10^3$

Range of Prandtl number 0.7

Range of (μ_b/μ_0) 1

Correlation,

$$\text{Nu} = \left(0.5\text{Re}^{1/2} + 0.2\text{Re}^{2/3}\right) \text{Pr}^{1/3} \quad (5.20)$$

5.2.3 Single pebble correlations

For a sphere in an infinite, quiescent fluid where conduction is the only mode of heat transfer, the Nusselt number is identically 2. In all the single particle correlations, that value is the limit as $\text{Re} \rightarrow 0$.

Ranz & Marshall in 1952

Zhou, et al 2009

$$\text{Nu}_i = 2.0 + 1.2\text{Re}_i^{1/2} \text{Pr}^{1/3} \quad (5.21)$$

5.3 Radiative transfer with neighboring particles

The temperatures expected in the solid breeder are high enough that we can not a priori neglect radiation. The radiation exchange between contacting neighbors in a packed bed becomes extremely complex due to the local and semi-local nature of radiation. A standard approach to treat radiation exchange between surfaces is to consider the view factor between them. In a dense, randomly packed bed of spheres the computation of view factors between pebbles can be done via a method such as that proposed Feng and Han.²¹ Ideally, we could show this mode of heat transport is negligible compared to the others already discussed.

In ceramic breeder designs, the tritium breeding volume is rarely more than 2cm wide with pebbles that are, generally, 1mm in diameter. The maximum expected temperature in the breeding zone is about 1000K, roughly at the centerline of the 2cm width. The walls of the coolant must be held below the operable steel temperature of roughly 700K. This

works out to a 300K differences spanning 10 pebble diameters. From this we can make a first-order approximation of 30K difference between neighboring pebbles. At the elevated temperatures, an estimate for the radiation exchange between two pebbles (allowing them to act as black bodies for this approximation) is

$$\dot{Q}_{\text{radiation}} = \sigma A (T_{\max}^4 - (T_{\max} - 30)^4) \approx 0.022\text{W} \quad (5.22)$$

which is the highest amount of radiation exchange we might expect between pebbles. Even though we will neglect this mode of heat transfer for now, after reviewing some of the packed bed heat transfer results we may find that this quantity of energy transfer is not negligible and future versions of the model would have to account for it.

Part III

Methodology

CHAPTER 6

Modeling Discrete Element Method (DEM)

This chapter presents the motivations and background of this study. First, it discusses energy usage in our society and the inevitable production of waste mechanical and thermal energies and their ubiquitous nature. This is followed by a brief discussion of common methods of converting ambient mechanical energy and waste heat into useful electrical energy. This chapter concludes with the objectives of this study and the scope of the document.

6.1 Background

The observable, macroscopic behavior of particulate, or granular, systems is a complex function of the multitude of particle-scale interactions. Historically, empirical relationships have been used to describe these systems as if a continuous media. But with the advent of the discrete element method by Cundall and Strack¹⁵ and the acceleration of computing power, it became practical to investigate these particulate systems at the particle scale. With the discrete element method, we track all the particles in the system in a Lagrangian manner. In the ensemble, the kinematics of each particle is tracked and updated based on balances (or imbalances) of forces or energy acting upon the particle.

Experiments on packed beds are generally limited to measurements of statistically averaged, macroscopic responses. Unlike continuous materials, packed beds as yet can not be described by any State. For instance, with an ideal gas if we know two properties such as temperature or pressure, the State of the gas is known and its behavior predicted. Two packed beds with the same temperature, packing fraction, average particle diameter, and stress state may react wildly different. As researchers we create empirical fits to data on

the particular packed bed under investigation but then might have to dubiously apply the relationships to beds of different packing states.

DEM is emerging as a reliable method to remove speculation about the internal state of the packed bed as the simulations provide valuable information on the dynamics of particle interactions and how they relate to the macroscopic responses that are measured experimentally.

In this chapter we will lay out the formulas governing interaction of particles in the DEM framework, the methods of computation, and the code used for implementation. In § 14.4, we will use the derivation of the Hertz contact law described in § 3 to argue for a technique of accelerating the computational time without loss of physics via proper scaling of physical parameters. Lastly, in § 9.1, we use our DEM tools to investigate the thermo physics of representative packed beds for solid breeders in fusion reactors.

6.2 Particle dynamics

The particles in our system are allowed translational and rotational degrees of freedom. In a packed bed, we can restrict our attention to local forces between particles; neglecting, say, non-contact forces such as van der Waals or electrostatic forces. In the first construct, we will treat the particles as if in a vacuum and leave a derivation of fluid interaction forces for § 7.

6.2.1 Particle kinematics

Assuming we know the contact forces acting upon particle i , Newton's equations of motion describe the motion of the particle. The translational and rotational for the translation degrees of freedom:

$$m_i \frac{d^2 \mathbf{r}_i}{dt^2} = m_i \mathbf{g} + \mathbf{f}_i \quad (6.1a)$$

$$I_i \frac{d\omega_i}{dt} = \mathbf{T}_i \quad (6.1b)$$

where m_i is the mass of this particle, \mathbf{r}_i its location in space, \mathbf{g} is gravity, I_i is the particle's moment of inertia, and ω_i its angular velocity.

The net contact force, \mathbf{f}_i , represents the sum of the normal and tangential forces from the total number of contacts, Z , acting on this particle.

$$\mathbf{f}_i = \sum_{j=1}^Z \mathbf{f}_{n,ij} + \mathbf{f}_{t,ij} \quad (6.2)$$

and the net torque, \mathbf{T}_i , is similarly,

$$\mathbf{T}_i = -\frac{1}{2} \sum_{j=1}^Z \mathbf{r}_{ij} \times \mathbf{f}_{t,ij} \quad (6.3)$$

6.2.2 Linear spring-dashpot model

When Cundall and Strack first proposed the discrete element method, they used a linear spring-dashpot structure which saw the normal and tangential forces written as,

$$\mathbf{f}_{n,ij} = k_{n,ij} \delta_{n,ij} \mathbf{n}_{ij} - \gamma_{n,ij} \mathbf{u}_{n,ij} \quad (6.4a)$$

$$\mathbf{f}_{t,ij} = k_{t,ij} \delta_{t,ij} \mathbf{t}_{ij} - \gamma_{t,ij} \mathbf{u}_{t,ij} \quad (6.4b)$$

The fictive tangential overlap, $\delta_{t,ij}$, is truncated to so the tangential and normal forces obey Coulomb's Law, $\mathbf{f}_{t,ij} \leq \mu_i \mathbf{f}_{n,ij}$ with μ as the coefficient of friction of the particle. In the first model of Cundall and Strack, the stiffness coefficients k were constants and the local damping coefficients γ were proportional to them, $\gamma \propto k$ to allow dissipation of energy

and the system to reach an equilibrium. The relative normal and tangential velocities, respectively, are decomposed from the particle velocities,

$$\mathbf{u}_{n,ij} = (-(\mathbf{u}_i - \mathbf{u}_j) \cdot \mathbf{n}_{ij}) \mathbf{n}_{ij} \quad (6.5a)$$

$$\mathbf{u}_{t,ij} = (-(\mathbf{u}_i - \mathbf{u}_j) \cdot \mathbf{t}_{ij}) \mathbf{t}_{ij} \quad (6.5b)$$

with the unit vector \mathbf{n}_{ij} pointing from particle j to i

Similarly to the approach of Hertz (see § 3), the surfaces of the two particles are allowed to virtually pass through each other (no deformation) resulting in normal and tangential overlaps of,

$$\delta_{n,ij} = (R_i + R_j) - (\mathbf{r}_i - \mathbf{r}_j) \cdot \mathbf{n}_{ij} \quad (6.6a)$$

$$\delta_{t,ij} = \int_{t_{c,0}}^t \mathbf{u}_{t,ij} d\tau \quad (6.6b)$$

We have a relatively simple approach of calculating the interaction forces between particles with Eq. 6.4 based on the kinematics of velocity and position of the interacting particles from Eq. 6.5 and Eq. 6.6, respectively. As the DEM evolved and drew the attention of more researchers, more complex formulas governing the forces of Eq. 6.4 emerged. But the core approach remained the same and the models all fall into the same family of so-called ‘soft particle’ models of DEM. A well-composed summary of the different DEM force models is given by Zhu et al.⁷²

The method used in our work is fit into the computational skeleton of Cundall and Strack’s method but with non-linear spring-dashpot coefficients defined by simplified Hertz-Mindlin-Deresiewicz model; the details will be expressed in the next section.

6.2.3 Hertzian non-linear spring dashpot model

The normal-direction (Hertz) stiffness coefficient of Eq. 6.4a is based on the Hertzian contact laws given in § 3.1. The tangential-direction (Mindlin) stiffness coefficient follows from Brilliantov,^{6,37,72}

$$k_{n,ij} = \frac{4}{3} E_{ij}^* \sqrt{R_{ij}^* \delta_{n,ij}} \quad (6.7a)$$

$$k_{t,ij} = 8G_{ij}^* \sqrt{R_{ij}^* \delta_{t,ij}} \quad (6.7b)$$

with G_{ij}^* as the pair bulk modulus,

$$\frac{1}{G_{ij}^*} = \frac{2(2 + \nu_i)}{E_i} + \frac{2(2 + \nu_j)}{E_j} \quad (6.8)$$

The damping coefficients, γ , arise to account for the energy dissipated from the collision of two particles.^{18,57,58} Whether the damping coefficient is local or global and the exact form of the coefficient is more important for loosely confined granular systems and dictates the way the system approaches an equilibrium state.⁴¹ For the case of our tightly packed pebble beds, it suffices to use the efficient form of,^{6,41,51,66,72}

$$\gamma_n = \sqrt{5\beta_{\text{diss}} m^* k_{n,ij}} \quad (6.9a)$$

$$\gamma_t = \sqrt{\frac{10}{3}\beta_{\text{damp}} k_{t,ij} m^*} \quad (6.9b)$$

with β_{damp} as the damping ratio, and the pair mass, $\frac{1}{m^*} = \frac{1}{m_i} + \frac{1}{m_j}$. For a stable system with $\beta_{\text{damp}} < 1$, the damping ratio is related to the coefficient of restitution, e ,

$$\beta_{\text{diss}} = -\frac{\ln e}{\sqrt{\ln^2 e + \pi^2}} \quad (6.10)$$

6.2.4 Time integration

Having expressed the contact mechanics of the discrete element method, we now need a means of integrating the kinematics of the particles. The most common means of marching in time with DEM is the velocity-Verlet algorithm.³⁶ In this algorithm we integrate Eqs. 6.1 with half-steps in velocity, full steps in position, and then finally the complete step in velocity (the two half-steps in velocity are often compressed into a single, full step, as we will do below). Here we will explicitly show the integration for the translational degrees of freedom.

The force field defined by Eq. 6.1a is rewritten in terms of the acceleration of the particle. For clarity in expression, the per-particle subscripts (i , j , etc.) will be temporarily omitted. Instead, time-varying quantities will have a subscript to refer to their temporal location. Quantities measured or evaluated at the current timestep will have subscript t (note this does not refer to tangential directions!). Eq. 6.1a is rewritten as

$$\mathbf{a}_t = \mathbf{g} + \frac{\mathbf{f}_t}{m} \quad (6.11)$$

The first step in the velocity-Verlet algorithm is to integrate the position of the particle by a full timestep based on the current timestep's velocity and acceleration. Note that the initial condition of the particle must specify both position and velocity for this step to be evaluated at the start, from then on the velocity is explicitly updated.

$$\mathbf{r}_{t+\Delta t} = \mathbf{r}_t + \mathbf{v}_t \Delta t + \frac{1}{2} \mathbf{a}_t \Delta t^2 \quad (6.12)$$

The particles at new positions interact as a function of their overlaps (see Eqs. 6.4). Acceleration at the full timestep is then calculated from the updated forces (of Eq. 6.11). In the last computational step, the velocity at the full timestep is found from an average acceleration,

$$\mathbf{v}_{t+\Delta t} = \mathbf{v}_t + \frac{\mathbf{a}_t + \mathbf{a}_{t+\Delta t}}{2} \Delta t \quad (6.13)$$

The velocity-Verlet algorithm is an efficient means of explicitly integrating the kinematic equations for all the particles in the ensemble. The algorithm is stable with a global error of approximately $O(\Delta t^2)$ for displacement.³⁰ But, as an explicit method, the size of the timestep must be carefully chosen to avoid instabilities in the system. Stable, critical timesteps and means of circumventing unreasonably small timesteps will be addressed in § 14.4. Additionally, we have contended with the Lagrangian tracking of the particles momentum but we have still to deal with energy transfer through the packed beds which is just as important for our packed beds of ceramic breeder material. The heat transfer will be tackled in § 6.3.

In our work, we occasionally required a fully quiesced bed. To determine when this occurred, the total kinetic energy of the entire ensemble was monitored and a packed bed was considered to have completely settled once the kinetic energy of the system was less than 10^{-9} ; similar to the process described in Ref.⁵³

6.3 Granular heat transfer

In an analogous way we handled the momentum of every particle in DEM with Newton's laws of motion, the Lagrangian tracking of energy of each particle is obtained via the first law of thermodynamics. We treat each particle as a single distinct object and thus do not consider any internal temperature gradients (a point which we alluded to in § 14.2). The temperature of particle i is governed by

$$\rho_i V_i C_i \frac{dT_i}{dt} = Q_{s,i} + Q_i \quad (6.14)$$

where ρ , V , and C are the density, volume, and the specific heat of the solid, respectively. Heat generation inside the particle is input with Q_s and the total heat transferred to/from particle i via conduction to all, Z , neighboring particles,

$$Q_i = \sum_{j=1}^Z Q_{ij} \quad (6.15)$$

The conductive heat transfer to neighboring particles comes from the inter-particle conduction formulas we derived in § 5.1, given in Eq. 5.2 with conductance of Eq. 5.5. They are repeated here for reference,

$$Q_{ij} = H_c(T_i - T_j)$$

and

$$H_c = 2k^* \left[\frac{3F_{n,ij}R^*}{4E^*} \right]^{1/3} \quad (6.16)$$

6.3.1 Thermal expansion

The stresses predicted to act upon the solid breeder volume during operation of the fusion reactor arise from the differential rate of thermal expansion from the highly heated ceramic volume and the relatively cool structural container. Moreover, thermal creep motion is observed in pebble beds^{11, 19, 55, 63} and is behavior we must capture in our model. Both of those phenomena can be traced to the thermal expansion of individual particles in the ensemble. Therefore, we introduce a thermal expansion formula that updates the diameter of each particle after a chosen amount of timesteps,

$$d_i = d_{0,i} [1 + \beta_i (T_i - T_{\text{ref}})] \quad (6.17)$$

where β_i is the thermal expansion coefficient (in units of 1/K), T_i is the temperature of the pebble at the current step, and $d_{0,i}$ is the diameter of the pebble at temperature T_{ref} .

6.4 DEM solver

6.4.1 Numerical Implementation Overview

The primary computational tools used in this study is LAMMPS (Large-scale Atomic/Molecular Massively Parallel Simulator);⁴⁵ a classical molecular dynamics code. The package of code, maintained by Sandia National Labs (<http://lammps.sandia.gov>), has many features making it particularly attractive for our use on the simulation of pebble beds. LAMMPS is open-source and written in highly-portable C++ allowing customization of any feature used in modeling. LAMMPS runs with distributed-memory message-passing parallelism (MPI) and provides simple control (manual or automatic) of the spatial-decomposition of simulation domains for parallelizing. Perhaps most importantly, LAMMPS provides an efficient method for detecting and calculating pair-wise interaction forces; the largest consumer of run-time in the DEM algorithm.⁴⁵ We build the code as a library so that LAMMPS can be coupled to other numerical tools; we use the scripting language of Python (Python 2.7) as an umbrella code to call LAMMPS routines with the full availability of Python libraries.

LAMMPS by default provides a rudimentary method of modeling of granular particles (the term ‘granular’ here differentiates the ‘discrete element’ of molecules or atoms from larger-scale granular particles of powders or pebbles); LAMMPS has been used for studying granular material since at least 2001 when Silbert, et al.⁵⁴ studied granular flow on inclined planes. However, the usefulness of LAMMPS for studying granular systems was greatly enhanced by LIGGGHTS (LAMMPS Improved for General Granular and Granular Heat Transfer Simulations), a suite of modules included on top of LAMMPS. LIGGGHTS has many academic and industrial contributors from around the world, with the code maintained as open-source by DCS Computing, GmbH.

Briefly, some notable features the LIGGGHTS code brings to the LAMMPS environment include: Hertz/Hooke pair styles with shear history, mesh import for handling wall geometry, moving meshes, stress analysis of imported meshes, a macroscopic cohesion model, a heat transfer model, and improved dynamic load balancing of particles on processors.^{33,34} Both

LIGGGHTS and LAMMPS are distributed under the open-source codes under terms of the Gnu General Public License.

We will review some of the important physical models used in LAMMPS/LIGGGHTS as they relate to the important features we wish to investigate for packed beds of pebbles in fusion reactors.

CHAPTER 7

Modeling coupled computational fluid dynamics and discrete element method (CFD-DEM)

[talk about how lacking the DEM result is without the inclusion of helium in analysis. There are some Fusion papers on conductivity in vacuum and with helium]

We now consider the influence of helium on thermal transport of deposited nuclear energy as it is carried away by the cooled structural walls. We begin by considering the fluid in a continuum sense and the pebbles in a discrete one. The interactions of the fluid and solid are characterized by effective relationships in each discretized cell of fluid. We then consider an mesoscopic approach to the fluid-solid interaction with the Lattice-Boltzmann method.

The chapter begins with introduction of the coupled fluid dynamics - discrete element method (CFD-DEM) approach: governing equations, discretization techniques, and algorithms.

We then do LBM. And stuff.

7.1 Numerical Methodology

Models based on the discrete element method (DEM) are currently the only tools available that can extract information on individual pebble interactions. The DEM formulation provides information such as inter-particle forces and individual particle temperatures, which are necessary for predicting and simulating morphological changes in the bed (e.g. pebble cracking, sintering, etc.) However DEM alone is not able to capture the effects, neither on momentum nor energy, of an interstitial fluid. Therefore we present two fluid modeling

techniques to supplement the DEM computations. We will first discuss the fully dynamic coupling of the DEM model with a volume-averaged thermofluid model of helium. Then we will introduce the integration of our DEM packing structure into lattice-Boltzmann simulations of the entire bed-fluid system.

7.1.1 DEM

The discrete element framework introduced in § 6.2 is augmented with a drag force term to capture interaction with surrounding fluid velocity fields. To accomplish this, we simply include a drag force to the Newtonian balance of forces given in Eq. 6.1. The momentum balance now reads:

$$m_i \frac{d^2 \mathbf{r}_i}{dt^2} = m_i \mathbf{g} + \mathbf{f}_i + \beta_i V_i \Delta u_{if} \quad (7.1)$$

where $\Delta u_{if} = u_f - u_i$, is the relative velocity between the fluid and pebble, i , and the inter-phase momentum exchange coefficient, β_i , acts upon the pebble volume (not to be confused with the damping coefficient introduced in § 6.2). Similarly, the energy equation now includes

$$m_i C_i \frac{d^2 T_i}{dt^2} = Q_{n,i} + \sum_{j=1}^Z Q_{ij} + \beta_{E,I} A_i \Delta T_{if} \quad (7.2)$$

where $\Delta T_{if} = T_f - T_i$, is the relative temperature between the fluid and pebble, i , and the inter-phase energy exchange coefficient, $\beta_{E,i}$, acts upon the pebble surface area, A_i .

The trajectory of pebble i is updated based on the force terms on the right hand side of Eq. 7.1: gravity, contact forces between particles (or particle-wall), and a drag force. Similarly, the temperature of the particle updates with the terms from Eq. 7.2: nuclear heating rate, inter-particle conduction, and now a heat transfer with surrounding fluid.

Drag forces from fluid flows through packed beds are found from volume-averaged, empirical correlations of either numerical or experimental studies. Considering a small region

of a packed bed surrounding our particle of interest, i , the nondimensional drag force is found only as a function of the local packing fraction of that region. In the zero Reynolds number limit, the nondimensional drag force reduces to a Stokes flow correlation that is only a function of the local packing fraction value, ϕ . For the value of particle Reynolds numbers seen by the helium purge gas, this is the dominant term. However, for a complete discussion of the nondimensional drag terms see Refs. 5, 6. The correlation used in this study comes from the results of numerical studies of packed beds by Koch and Hill.^{5,29,35} To arrive at their relationships, they did many lattice-Boltzmann simulations of porous flow.

$$\beta_i = \frac{18\nu_f\rho_f}{d_i^2}(1 - \phi)F \quad (7.3)$$

where

$$F = \epsilon(F_0 + \frac{1}{2}F_3\text{Re}_{p,i}) \quad (7.4)$$

Stokes flow

$$F_0 = \begin{cases} \frac{1+3\sqrt{\phi/2}+(135/64)\phi\ln(\phi)+17.14\phi}{1+0.681\phi-8.48\phi^2+8.16\phi^3} & \text{if } \phi < 0.4 \\ 10\frac{\phi}{(1-\phi)^3} & \phi > 0.4 \end{cases} \quad (7.5)$$

and high Reynolds contribution

$$F_3 = 0.0673 + 0.212\phi + \frac{0.0232}{(1 - \phi)^5} \quad (7.6)$$

The packing fraction and void fraction in any fluid cell is calculated by summing through all the volumes of k particles located in that cell (or the complement thereof)

$$\phi = \sum_{i=1}^k \frac{V_{p,i}}{\Delta V_f} \quad (7.7)$$

Other forces, such as Magnus forces, are inconsequential on predominantly stationary packed beds and are not considered.

The inter-phase energy transfer coefficient is of the same form as a traditional heat transfer coefficient and is calculated from the Nusselt number for the helium flow (with conductivity k_f) through a packed bed.

$$\beta_{E,i} = \frac{\text{Nu}_i k_f}{d_i} \quad (7.8)$$

Li and Mason³⁸ summarize correlations for Nusselt number as a function of Reynolds number for packed beds with the following equations

$$\text{Nu} = \begin{cases} 2 + 0.6(1 - \phi)^n \text{Re}_p^{1/2} \text{Pr}^{1/3} & \text{Re}_p < 200 \\ 2 + 0.5(1 - \phi)^n \text{Re}_p^{1/2} \text{Pr}^{1/3} + 0.2(1 - \phi)^n \text{Re}_p^{4/5} \text{Pr}^{1/3} & 200 < \text{Re}_p \leq 1500 \\ 2 + 0.000045(1 - \phi)^n \text{Re}_p^{9/5} & \text{Re}_p > 1500 \end{cases}$$

where $n = 3.5$ was found to fit best for small particles in dilute flows. [we should find a new value for high packing fraction]

Thus we have a formulation whereby a known fluid flow field and temperature throughout the domain, we can calculate the influence of that fluid on every particle's position and temperature. Next we will cover how we can calculate the flow field based on a volume-averaged influence of particles on the fluid.

7.1.2 Volume-averaged CFD Helium

The technique of coupling CFD to DEM was first proposed by Tsuji, et al9. In this formulation of the helium flow, a fluid cell is much larger than the individual particles (in application, this meant approx. 5-6 particles per cell) and as such, the particles themselves are not resolved in the fluid space but are simply introduced via volume-averaged terms. Therefore momentum and energy of a fluid flow through a solid phase is governed by volume-averaged Navier-Stokes and energy equations¹⁰. These equations are applied to a discretized volume

of fluid space. For fluid cell, k, these are5:

$$\frac{\partial \epsilon_k \rho_f}{\partial t} + \nabla \cdot (\epsilon_k u_f \rho_f) = 0 \quad (7.9a)$$

$$\frac{\partial \epsilon_k u_f}{\partial t} + \nabla \cdot (\epsilon_k u_f u_f) = -\frac{\epsilon_k}{\rho_f} \nabla P_f + \nabla \cdot (\nu_f \epsilon_k \nabla u_f) - \frac{S_k}{\rho_f} \quad (7.9b)$$

$$\frac{\partial \epsilon_k T_f}{\partial t} + \nabla \cdot (\epsilon_k u_f T_f) = \nabla (\epsilon_k \epsilon \nabla T_f) - \frac{E_k}{\rho_f C_f} \quad (7.9c)$$

where the fluid void fraction is the complement of the solid packing fraction, $\epsilon = 1 - \phi$. The momentum and energy exchanges with the solid phase are represented in the source terms. They are volume-weighted sums of the drag forces and energy exchanges, respectively, for all particles in the discretized fluid cell:

$$S_k = \frac{1}{V_k} \sum_{\forall i \in k} \beta_i V_i \Delta u_{if} \quad (7.10a)$$

$$E_k = \frac{1}{V_k} \sum_{\forall i \in k} \beta_{E,i} A_i \Delta T_{if} \quad (7.10b)$$

The inter-phase momentum and energy exchange coefficients act as the communicators between the particle information from the DEM solver and the fluid fields from CFD. Thus the motion and energy of the fluid field are intimately coupled with the particle positions and energy, but computational time is preserved by only considering volume-averaged values in the fluid domain. The cross-communication between fluid and solid is accomplished with a coupling routine that is explained in detail in Refs. 11, 12.

7.1.3 Modeling Setup and Procedure

The pebble bed has dimensions in the x-y directions of $20d \times 15d$, respectively. There are structural walls, providing cooling, at the x-limits and periodic walls in the y-limits. 10 000 pebbles were loaded into the system which went to a height of approximately $24d$ after the bed was vibration packed. The pebble bed had a roof loaded at the upper limit of the

z-direction that was lowered by force-control up to 6 MPa. This bed is referred to as the ‘well-packed’ bed. This was meant to simulate a fresh, densely-packed bed that is under compressive load during fusion operation. As such, this would be when pebbles would be likely to crack during operation. Therefore, based on the well-packed bed, a second bed was generated by simulating crushed pebbles; crudely the extensive crushing is simulated by simply removing 10% of the pebbles at random from the ensemble and then allowing the bed to resettle, from the now-imbalanced gravity and inter-particle forces, to a new stable packing structure. This bed is then referred to as the ‘resettled’ bed for the rest of the analysis. The intent is to deduce changes in thermomechanical properties from an ideally packed bed to one where significant cracking has altered the ideal morphology of the bed.

CHAPTER 8

Modeling lattice-Boltzmann Method (LBM)

Part IV

Cases studied

CHAPTER 9

DEM studies

The discrete element method (DEM) is used by many ceramic breeder researchers to model the interaction of individual pebbles in an ensemble in an effort to obtain a more detailed understanding of pebble beds than is possible with experimental measurements of effective properties. For example see Refs.^{2,3,25,39,60,68}

9.1 DEM study: effective conductivity with disrupted packing

9.1.1 Model Setup & Methodology

We analyze a three-dimensional pebble bed consisting of mono-dispersed particles of diameter d_p . The particles are constrained by rigid $y - z$ -planes at locations of $\frac{x}{d_p} = \pm 10$ (the walls of our container). There are periodic boundary conditions in the y -direction located at $\frac{y}{d_p} = \pm 7.5$. Gravity acts in the negative z -direction and the particles are resting on a rigid $x - y$ -plane at $z = 0$ (the floor of the container) and held from the top by an $x - y$ -plane at $\frac{z}{d_p} = 30$ (the roof of the container). We pack to $\phi = 64\%$ and, given the volume, have 11000 particles. The volume was chosen to represent the long, tall, narrow channels seen in many solid breeder module designs.^{13,20,46}

For this study, the material properties were chosen to represent lithium metatinatate pebbles. All the properties come from Ref.²⁸ They are summarized in Table 9.1

In the first attempt at packing pebbles into the system, we begin with a common starting point of a filled, lightly packed volume of 10 550 pebbles. We simulate pouring the pebbles

Table 9.1: Maximum load and nominal tension.

E (GPa)	ν	k (W/m-K)	C (J/kg-K)	α (1/K)
126	0.24	2.5	1156	15×10^{-6}

into the volume by initializing them into the system from a height of $\frac{z}{d_p} \approx 50$ and allow them to fall under the influence of gravity (see Fig. 9.1). We pack the pebbles into a higher packing fraction by means of oscillating the walls as if the pebble bed were sitting on a vibrating plate. This was to imitate the vibration packing technique done in our experimental lab when testing pebble beds in the uniaxial compression test stand. The vibration scheme was able to slowly densify the packed bed but, owing to the very small timestep of the simulation, the simulation times were impractically large to approach a packing fraction greater than $\phi = 60\%$.

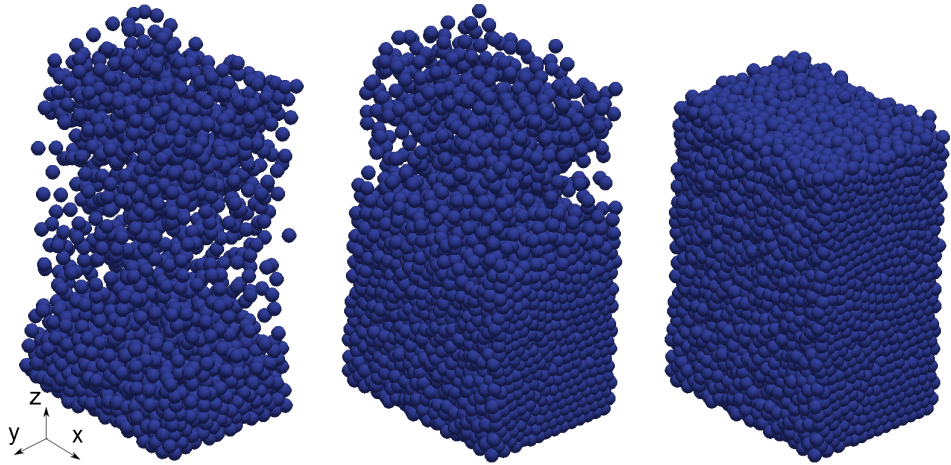


Figure 9.1: Demonstrating the pouring process of $N = 10550$ pebbles into the control volume with at an early time (left), when it is nearly filled (middle) and after the pebbles have settled to negligible kinetic energy (right).

In the end, a simpler pack-relax method was used instead. In this method N particles are inserted into the volume such that we have precisely the packing fraction we desire (in this

case, $\phi = 64\%$ so $N = 11000$). The pebbles are placed at random into the volume and are allowed to artificially overlap – often by a great deal ($\delta \sim R_p$). The overlap they experience would normally cause such an enormous force (integrating into an enormous velocity) that the pebbles would all explode out of the bed at the first step in time integration. We avoid such a catastrophic scenario with a relaxation scheme where we truncate the displacement of any pebble per timestep that is integrated from the force. The truncated displacement is very small and allows the pebbles to slowly move away from each other and into a static equilibrium as the artificial overlap is reduced. Once the pebble bed comes to rest, we remove the relaxation (limiting displacement command) and allow standard integration of contact forces with the velocity-Verlet algorithm (see § 6.2.4). The pack-relax scheme allowed for obtaining desireable, highly repeatable packing fractions for all pebble beds. Once the pebble bed was packed into an initial condition, the simulation state was saved and used as a starting point for the numerous ‘crushed’ cases to be described later.

In this first study, we model pebble crushing without considering why the particular pebble should be cracking. In the model we randomly select pebbles from the ensemble, regardless of forces acting upon the pebble, and delete them entirely from the system. When a pebble is removed, the neighboring pebbles react due to the imbalance of forces, and the bed settles into a new configuration. We differentiated the failed beds by their percentage of failed pebbles: $\eta = \text{number of failed pebbles per original ensemble size}$. For the baseline case and for beds after failing, we apply the heating routine described next.

To simulate the conditions of a solid breeder in a fusion reactor, where the heat is removed from the pebble bed via contact to the containing structure, we assigned a constant temperature of T_c to the vertical walls. Nuclear heating of the pebbles is simulated through a constant source term on each pebble. A representative heating rate of $Q_s = q''_p V_p$, where $q''_p = 8 \text{ MW/m}^3$. The heating cycle runs until a thermal steady state is reached. Based on a measurement of the total thermal energy of the bed, $E_T = \sum_i^N m_i C_i T_i$, steady-state is determined as $\frac{dE_T}{dt} = 0$ within a specified tolerance. Once at steady state, we analyzed thermal and mechanical characteristics of the pebble bed: effective thermal conductivity, average

coordination number, temperature profiles in the bed, and inter-particle contact forces.

Based on the boundary conditions to our system, we establish heat transfer that is symmetric and one-dimensional in the x -direction from $x = 0$ to the walls at $\frac{x}{d_p} = \pm 10$. As we will show, the pebble bed has very little variation of forces and temperatures in the y -direction due to the periodic boundary condition at the edges of the domain. Gravity effects are minor in the overall heat transfer and induce only a slight z -dependency to the results. We take advantage of this nature of our pebble bed to find the effective conductivity from an analytic, one-dimensional test case.

9.1.2 Effective Thermal Conductivity from Analytic Analogy

Assuming a one-dimensional pebble bed, to find an effective conductivity, we step back into a continuum mechanics formulation where the pebble bed can be represented as a slab of solid material. We can analytically solve for the temperature equation in a slab with heat generation, symmetry about the centerline, and a constant boundary temperature condition.

At steady-state, the temperature of a material with constant temperature boundary conditions ($T(L) = T_s$), constant thermal conductivity (k_{eff}), and nuclear heating (q'') obeys the following equation

$$0 = \frac{d^2T}{dx^2} + \frac{q''}{k_{\text{eff}}} \quad (9.1)$$

We introduce a non-dimensional temperature

$$\theta = \frac{T(x) - T_s}{T_0 - T_s} \quad (9.2)$$

where T_0 is the temperature at the centerline of this slab (a value we will find momentarily).

The length is non-dimensionalized as

$$x^* = \frac{x}{L} \quad (9.3)$$

Thus we can re-write Eq. 9.1 as

$$0 = \frac{d^2\theta}{dx^{*2}} + G \quad (9.4)$$

where

$$G = \frac{q'''L^2}{k_{\text{eff}}(T_0 - T_s)} \quad (9.5)$$

In the non-dimensionalized form, the solution is revealed to be purely geometric,

$$\theta = 1 - x^{*2} \quad (9.6)$$

. as $T_0 - T_s = \frac{q'''L^2}{2k_{\text{eff}}}$. We will use the non-dimensional temperature solution of Eq. 9.6 to prove our one-dimensional assumption of heat transfer is justified for the pebble beds.

We note that in this continuum mechanics formulation, we are assuming that the nuclear source, q''' term is applied evenly over the entire volume. In our DEM formulation, our source term applies to a single pebble. To find the effective thermal conductivity of our ‘slab’ of pebble bed, we must reconcile this discrepancy. This is accomplished with the exchange of

$$q''' = \frac{Q_{\text{tot}}}{V_{\text{tot}}} = \frac{Q_s N}{H \cdot L \cdot W \cdot d_p^2} \quad (9.7)$$

where the pebble bed volume is given by the height, H , width, W , and length, L , and Q_s is the source term on each pebble in the DEM ensemble.

From the solution of Eq. 9.4, we find the effective conductivity to be

$$k_{\text{eff}} = \frac{q'''L^2}{2(T_0 - T_s)} \quad (9.8)$$

and when we replace the heat generation term with Eq. 9.7, and use the bed dimensions as given in § 9.1.1, this is written as

$$k_{\text{eff}} = \frac{Q_s N}{180(T_0 - T_s)d_p} \quad (9.9)$$

We will use this formulation of Eq. 9.9 to analyze and compare the pebble beds of this study.

9.1.3 Results

The aim of this study was both to discover the impact of pebble failure on thermomechanical properties as well as determine the impact as a function of the number of failed pebbles. To satisfy the latter, we created beds with $\eta = 1\%, 3\%, 5\%, 10\%$, and 15% of pebbles failed.

We plot Eq. 9.6 against the non-dimensionalized temperature profiles coming from the steady-state DEM simulation in Fig. 9.2. We find that all our models had a nearly perfect match to a one-dimensional prediction, validating the calculation of effective thermal conductivity in this study. Furthermore, the profiles adhering to the one-dimensional curve also allows us to find the effective conductivity of each bed from applying Eq. 9.9, which was derived from the one-dimensional assumption.

One concern we had for pebble crushing, was the phenomenon of ‘jamming’ during resettling that would possibly leave pebbles isolated from their neighbors (apart from those they are resting upon). Jamming can happen when a bridge of pebbles have a balance for forces without strong or any contact to a pebble below them. The pebble under the bridge then only has light contact with the pebbles upon which it is resting. Such an isolated pebble would have no strong pathway for heat transfer and heat up much higher than that of its neighbors. Evidence of pebble isolation is apparent in hot individual pebbles above the grouped curve in Fig. 9.2.

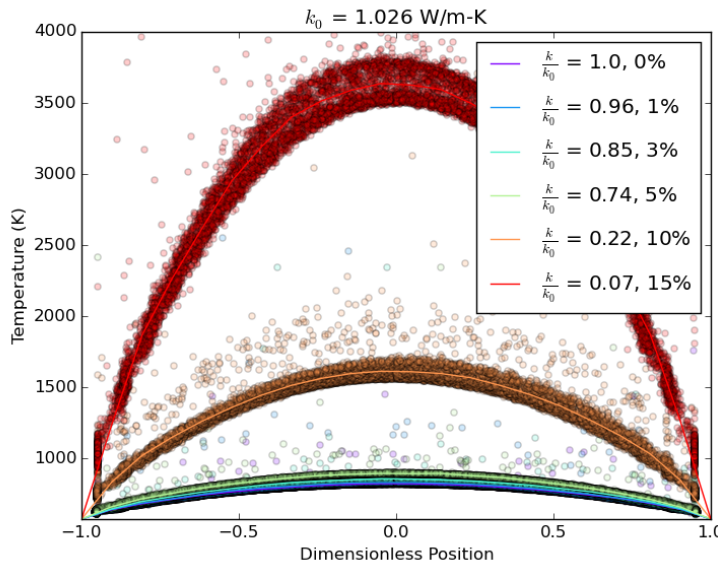


Figure 9.2: The nondimensional temperature profiles for each test case follow the theoretical shape of a one-dimensional, constant k , continuum solution.

Because the 10% and 15% cases have such high temperatures, we show only the 0-5%

crushed together in Fig. 9.3

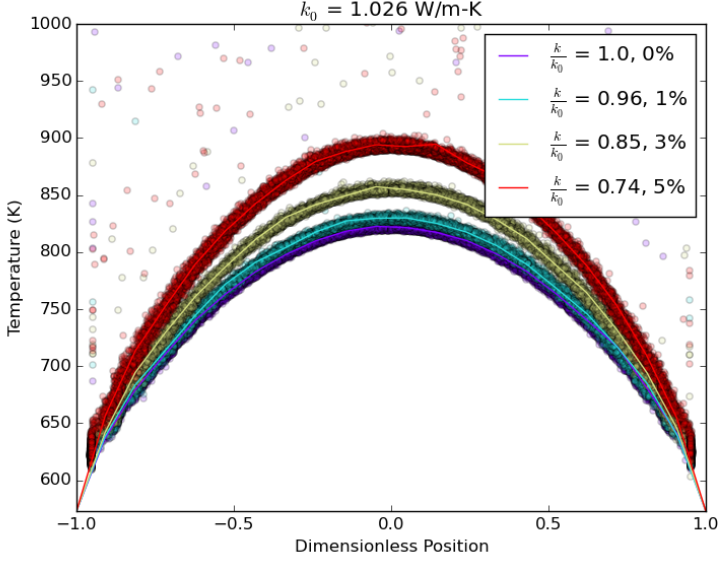


Figure 9.3: The nondimensional temperature profiles for the test cases up to 5% crushed pebbles.

The individual hot pebbles in Fig. 9.2 are also indicative of the shortcomings of the discrete element method for modeling solid breeders in fusion reactors. The flowing purge gas in actual solid breeders would likely not permit such thermal isolation of pebbles. Even if a pebble had no physical contact with neighboring ones, it would still transport energy via conduction and advection of the helium gas. This will be addressed again and in more detail in § 10.2.

In order to calculate an effective conductivity of the pebble bed, we must find an average temperature profile through the bed to compare with Eq. 9.6 and thus employ Eq. 9.9. We compare steady-state temperature profiles in the test beds against the one-dimensional, non-dimensional temperature profile. Average values of the bed, along the x direction, are generated via averaging temperatures in bins. We create bins that are volumes slices of width Δx that extend through the limits of the y - and z -directions. We then find the n pebbles residing in the slices and take the mean value of their temperatures. The average,

given by Eq. 9.10, is also given in Fig. 9.2. The binned average temperature is

$$\langle T \rangle = \frac{1}{n} \sum_i^n T_i \quad (9.10)$$

Using the volume slices, we also find the average coordination number,

$$\langle Z \rangle = \frac{1}{n} \sum_i^n Z_i \quad (9.11)$$

and average contact force,

$$\langle F^{1/3} \rangle = \frac{1}{n} \sum_i^n F_{n,ij}^{1/3} \quad (9.12)$$

In Eq. 6.14 of § 6.3, we see that at steady-state, the energy input by nuclear heating must be balanced by the transport of heat out of a pebble into its neighbors. Inter-particle heat transfer is dictated by the number of neighboring contacts, temperature difference between pebbles, and the thermal conductance, H_c , through the contact area. The thermal conductance (see Eq. 6.16) is itself a function purely of material properties (which are essentially constant here) and the force at the contact, going as $H_c \propto F_{n,ij}^{1/3}$. Thus, we write the net heat out of a pebble at steady state as a function of the three variables,

$$Q_{\text{net}} = f(Z, F_n^{1/3}, \Delta T) \quad (9.13)$$

The coordination number and contact forces are features of the packing structure in the packed bed that we can analyze to discover what happens to the heat flux between pebbles when the bed experiences crushed particles. Conversely, the ΔT between two pebbles is the effect of the thermal transport (i.e. leading to higher bed temperatures such as those of Fig. 9.2). We will first analyze the changes to the coordination numbers of pebbles in the ensemble as pebbles crush.

In Fig. 9.4 we plot the data for all pebbles in the ensemble as well as the binned average (Eq. 9.11). Clearly, there are fewer average contacts per pebble in the ensemble after failure; At 15% crushed the coordination number drops by roughly 30%. But this alone can not account for the reduction in k_{eff} by 93% for the same amount of crushed pebbles. Next we look to the normal contact forces between pebbles in the bed.

The normal contact forces between pebbles are plotted in Fig. 9.5. A dramatic reduction in the normal forces is seen after many of their neighbors are crushed and are removed from the system. From the baseline down to the 15% failed case, the contact forces are reduced by about a factor of 10 - similar to the reduction in effective conductivity.

The effective thermal conductivity was found for all of our pebble beds, via Eq. 9.9, then normalized against the conductivity of the baseline ensemble ($k^* = k/k_0$). The average coordination number of the beds and average normal contact forces were also found. Another way of describing a pebble bed is with the packing fraction, ϕ . In Fig. 9.6, we collect all these values (and normalize them against the baseline case) to provide a direct comparison to their changes as a function of crushed pebbles. When 15% of the pebbles are crushed in a pebble bed, the effective conductivity has fallen all the way to only $k^* = 0.07$. This large reduction is especially important in light of the already poor thermal management of virgin pebble beds that, even in helium environments, have been experimentally measured at only approximately 1 W/m-K (see, e.g., Refs.^{44,49}). The only parameter to have similar reductions in value is the average normal contact force, a value which is seen to follow closely to the curve of effective conductivity. Thus we conclude that the single most important factor for determining the effective thermal conductivity in these pebble beds is the normal contact forces between pebbles; a force which decreases sharply as pebbles are crushed in the system.

The large reduction in normal contact force (which leads to a large reduction in effective conductivity) is explainable based on the experimental setup of our numeric model. In our system, we had rigid walls in the x and z directions. These walls did not change after the substantial number of pebbles were crushed and removed. After the 15% crushing event, the pebble bed appeared as Fig. 9.7a. A massive re-arrangement proceeds from the crushing event. As the pebble bed heats up, the thermal expansion of the pebbles is unconstrained as there exists an average of two pebble diameter gap above the pebbles to the top of the container. Numerically there is no limit to the pebble temperatures (phase change and sintering is not incorporated into the DEM calculations) so the pebbles heat and swell until coming into contact with the top wall, at which time they begin to press into one another

(though lightly) to allow thermal conduction. The pebble bed after swelling is shown in Fig. 9.7b.

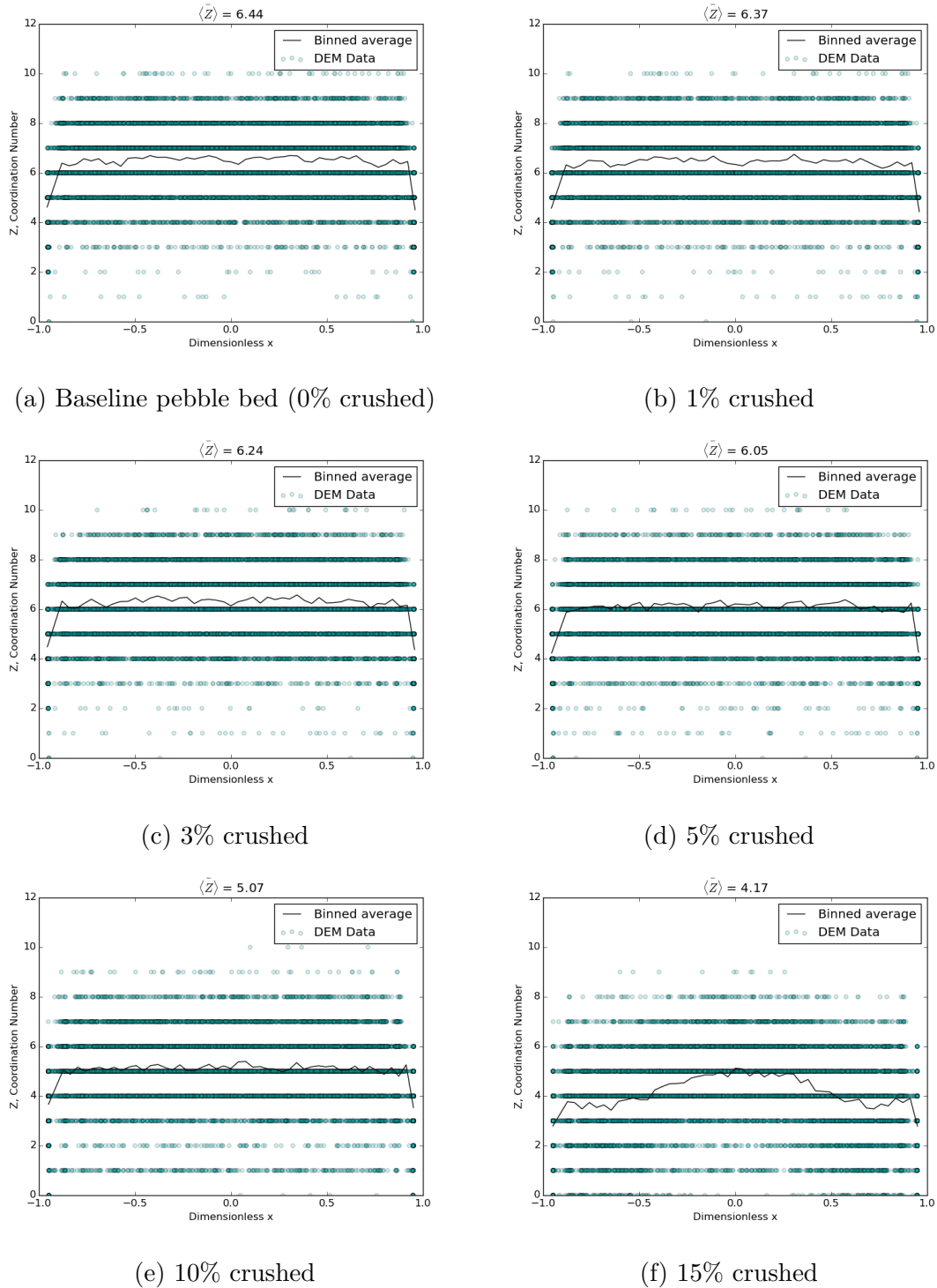


Figure 9.4: The average coordination number decreases slowly as the number of broken pebbles in the ensemble increases.

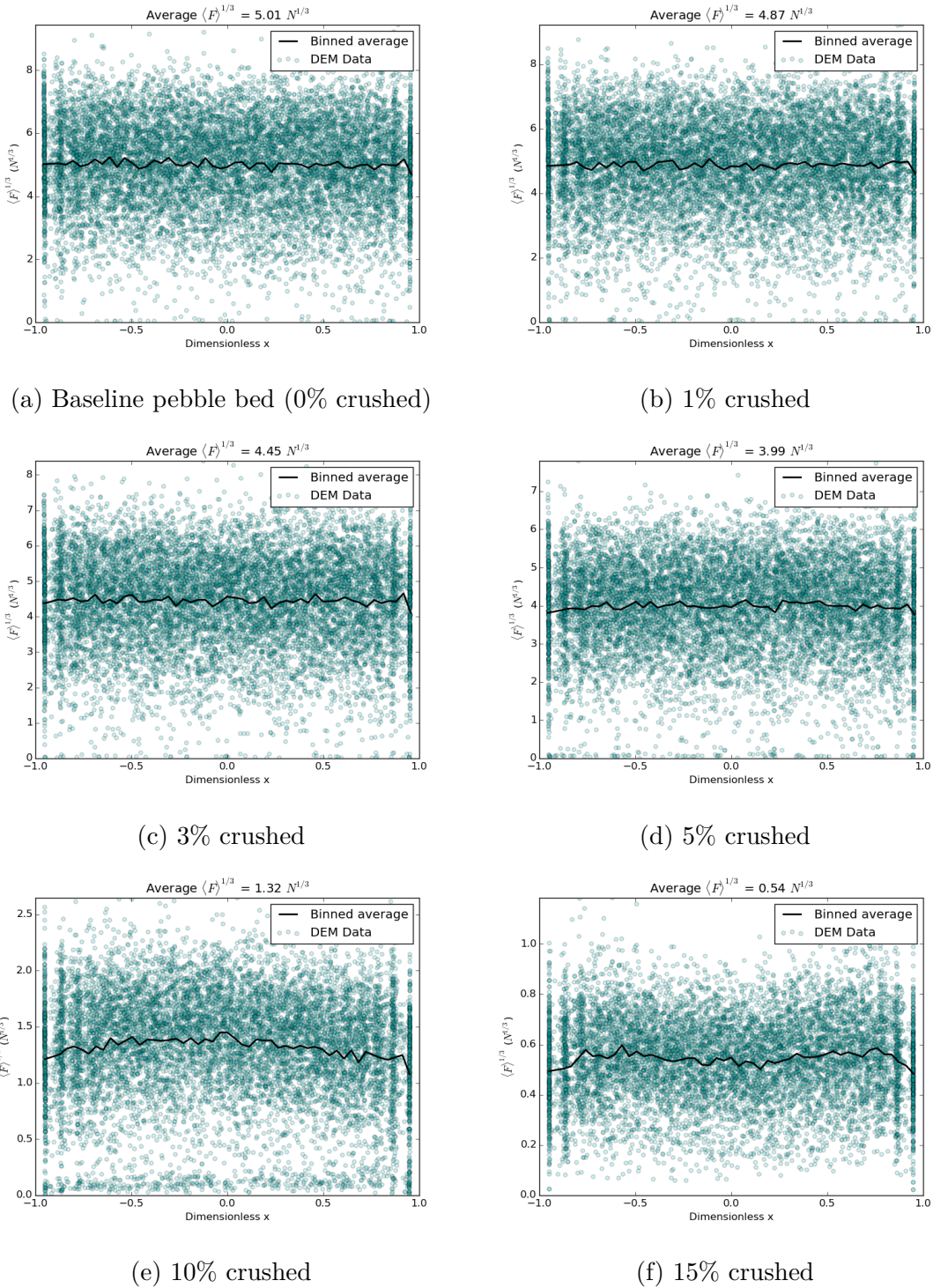


Figure 9.5: As pebble beds experience massive amounts of crushed pebbles ($>5\%$), the contact forces in the ensemble (after heating to steady-state) show dramatic reductions in value. Note the change of scale on the figures from the baseline case to the 15% crushed case.

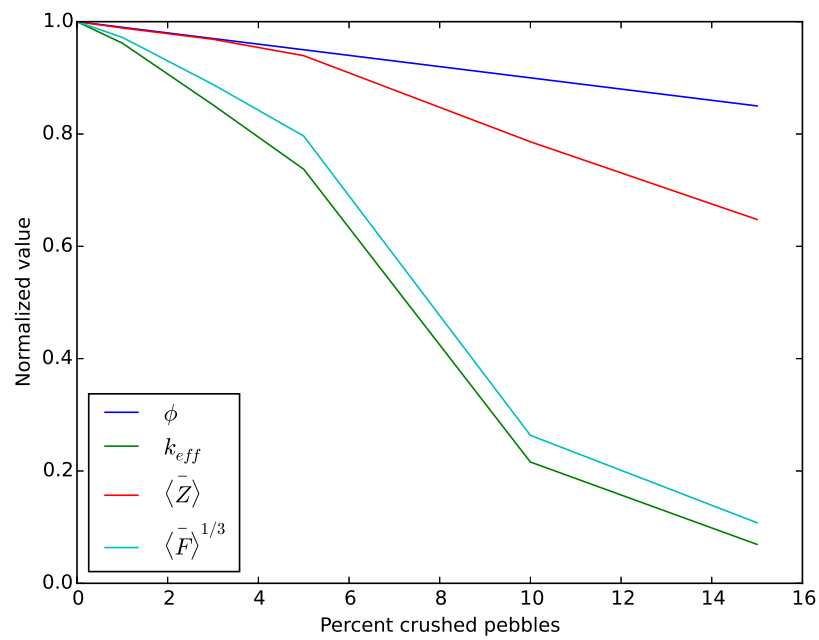
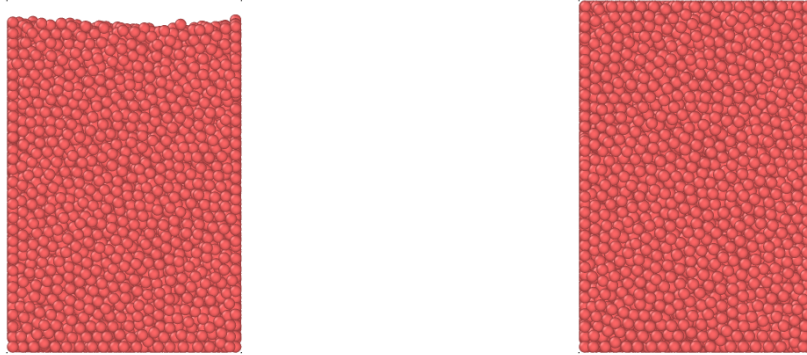


Figure 9.6: The normalized effective conductivity drops much more rapidly than the normalized packing fraction, ϕ , while pebbles are crushed. The effective conductivity follows with reduced normal contact forces.



(a) Side-view of the pebble bed after reset- (b) Side-view of the pebble bed after heating
tling from the crushing event, before heating.

Figure 9.7: In (a) we see the pebble bed after 15% of the pebbles have been crushed (removed) and then after the heating cycle in (b). The gap formed after crushing is completely filled by swelling pebbles.

9.2 Conclusions

The results shown in Figs. 9.5 and 9.4 demonstrate that the heat transfer through a pebble bed is simultaneously a function of both the coordination number and inter-particle contact forces. The average values of both of these parameters reduced as pebbles in the bed were crushed. Interestingly, when a pebble bed has lower overall inter-particle contact forces such as what we see when pebbles are crushed, we would predict fewer pebbles are likely to break. This result implies that pebble breakage is self-dampening; as pebbles begin to break the ensemble quickly relaxes and avoids future pebble failure. So while in this study we induced failure up to $\eta = 15\%$ without a concern for predicting if such a large amount would break, such large values may not occur in real beds during operation of a fusion reactor.

The first study of this dissertation established the groundwork of the DEM modeling to be carried out in the other studies. We simulated a pebble bed with a specified fraction of the pebbles crushing during operation; then determining the repercussions of the missing pebbles as they affect the macroscopic property of effective thermal conductivity. We used the assumption of homogeneous, random locations of pebble failure to induce a failure routine without requiring external loads on the bed to actually induce the pebble crushing. After heating to a steady-state, an effective thermal conductivity was calculated for the pebble bed. The results show that large amounts of pebble failure correspond to large decreases in the conductive transport of energy through the pebble bed. The increase was due primarily to a drop in the inter-particle forces which lead to a large increase in temperature differences between neighboring pebbles.

As the first step in the modeling effort, there were many simplifications that had to be made in this study. We must note here the shortcomings of the assumptions and simplifications of this study before drawing any major conclusions from the results.

First, the ‘container walls’ surrounding the pebble bed in this model are completely rigid and do not react as the swelling pebble bed presses into them while heating. The confined thermal expansion leads to very high contact forces in the pebble bed that may not be

realistic. The abnormally high contact forces are most likely to be the source of the abnormally high baseline effective thermal conductivity, $k_0 = 1.03 \text{ W/m-K}$. In experiments on the effective thermal conductivity of lithium ceramics in vacuum, the beds are often allowed to expand freely while heating (in at least one direction) and in vacuum were measured to be closer to $k_0 = 0.5 \text{ W/m-K}$ [FIND THE REAL VALUES TO PUT HERE!]. We note, however, that this value has been calculated in the absence of interstitial gas so the results apply only to the reduction in energy transferred via inter-particle conduction.

Second, we saw from Fig.9.2 that the majority of the pebbles in the ensemble have their temperatures close fitting to an average curve but a number of the pebbles had less thermal contact with neighboring particles and consequently had much larger temperatures. This was true even in the baseline case of a tightly packed ($\phi = 64\%$) pebble bed. This phenomena is only possible because the contribution to heat transfer of the interstitial gas was not considered in this model. The flowing helium gas is expected to prevent any runaway temperatures of individual pebbles as it provides another route of energy transfer in the bed. This will be addressed in § 10.

Lastly, the pebble crushing did not conserve mass and did not have predictive whatever.

CHAPTER 10

CFD-DEM studies

The numerical implementation of fluid-solid interaction was outlined in § 7. Although we are most interested in the thermal response of the packed beds to the interstitial gas, we will begin by comparing the results of momentum interaction.

10.1 Pressure Drop

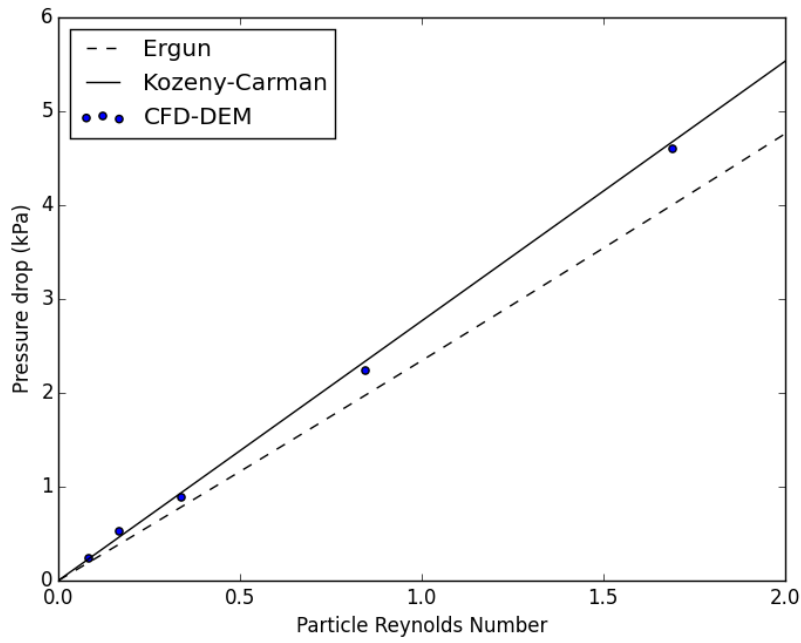
Before analyzing thermal results from the CFD-DEM coupling, the system was run at various particle Reynolds numbers and the overall pressure drop of the packed bed was measured. This value was compared against the well-known Kozeny-Carman and Ergun equations. The Kozeny-Carman is known to fit better with experimental data at very small Reynolds numbers. In Fig. 10.1 we see the CFD-DEM coupling model is providing bed-scale pressure drops that match very well with Kozeny-Carman over the Reynold's numbers applicable to helium purge flow in fusion reactors.

The flow is visualized in Fig. 10.2. The pebble bed is clipped at the centerline to allow viewing of the helium streamlines. Apparent in the figure is temperature profiles in the helium from centerline to wall that qualitatively mirror temperature profiles in the pebble bed.

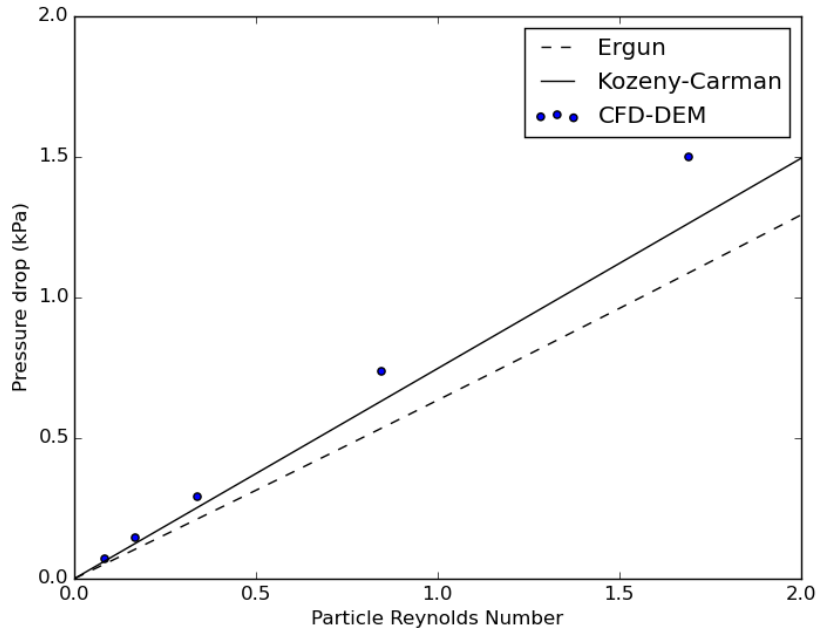
10.2 Effective thermal conductivity from CFD-DEM

10.2.1 Stagnant interstitial fluid

can use correlations for stagnant gas in packed bed.



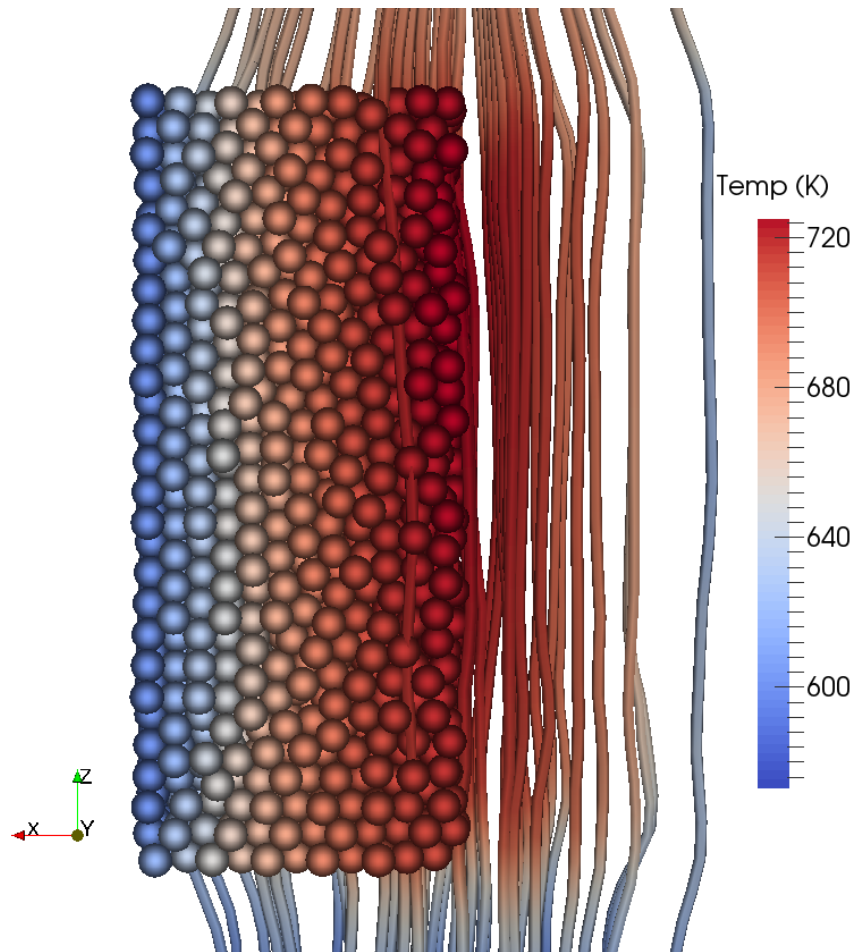
(a) Well-packed bed



(b) Re-settled bed

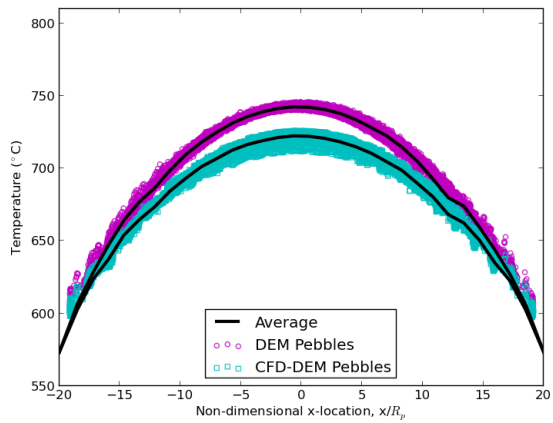
Figure 10.1: Pressure drop calculations across packed beds, solved by CFD-DEM, fit well to the Kozeny-Carman empirical relation.

Figure 10.2: Cut-away view of the pebble bed with streamlines of helium moving in generally straight paths from inlet to exit.

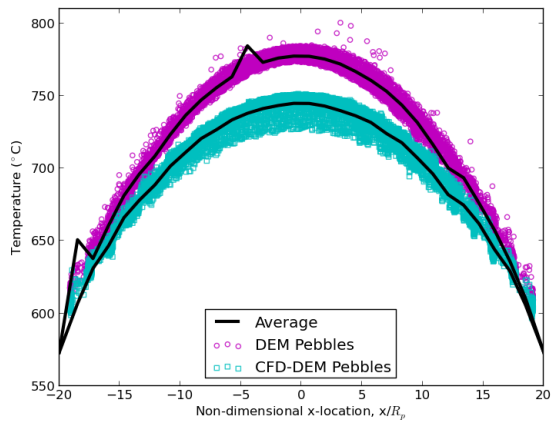


10.2.2 Purge gas

The well-packed and resettled pebble beds were run to thermal steady-state with nuclear heating and wall cooling in both pure DEM and coupled CFD-DEM simulations for comparison. From steady-state temperature distributions, seen in the pebble scatter plots in Fig. 3, an average profile is calculated and an effective thermal conductivity computed. The values are tabulated in Table I. In the case of pure DEM, energy is transported solely along conduction routes in the ensemble. When the packing of the bed is disturbed, this results in a substantial drop in effective conductivity (a drop of 31%). The details of the conductivity reduction were studied extensively in Ref. 23. Perhaps more important than the reduction



(a) Well-packed bed



(b) Re-settled bed

Figure 10.3: Scatter temperature profiles of pebbles in a bed that is: well-packed (left) and resettled after 10% of pebbles were removed from crushing (right). The introduction of helium into the simulation contributes to both lower overall temperatures (higher effective conductivity) and the smoothing out of high temperatures of isolated pebbles.

in effective conductivity, is the appearance of isolated pebbles. Because heat deposition is volumetrically applied, pebbles with poor conduction routes become much hotter than their neighbors. This is evident in the high temperatures seen in many of the pebbles in the right figure of Fig. 3. Over-heating of isolated pebbles could induce sintering and impact their tritium release even when the average temperatures measured in the bed are well below sintering values. When CFD-DEM beds are analyzed, there is still a large reduction in effective conductivity (22% drop), but interesting to note is the lack of isolated pebbles with high temperatures. In the CFD-DEM scatter plot of the right image in Fig. 3, there is evidence of the reduced heat transfer in the same region as the isolated pebbles from the DEM bed, but the temperatures are much closer to the average values of neighboring pebbles. The helium purge gas has effectively smoothed out the temperatures and provided heat transport paths for any pebbles that have loose physical contact with neighbors. In spite of the 22% decrease in effective conductivity, the maximum temperature of the pebble bed only increased 6.2% (from 725 to 751 K) when helium is included in the model. This result is significant for solid breeder designers. They may choose a solid breeder volume such that in the event of extensive pebble cracking, the maximum temperature of the bed would remain within the ideal windows dictate for the lithium ceramics.

Table 10.1: Pebble bed values from the test matrix of the beds analyzed in this study.

	k_{eff} (W/mK)		T_{\max} (K)		$\frac{Q_h}{Q_{\text{nuc}}}$
	DEM	CFD-DEM	DEM	CFD-DEM	CFD-DEM
Well-packed	0.96	1.09	745	725	1.15
Resettled	0.66	0.85	800	751	1.52

An accompanying result is the increased amount of energy carried out of the system by the helium purge gas. In Table I, the last column provides the ratio of energy carried out of the system to the nuclear energy deposited into the bed. The amount of energy carried out by the helium increased from 1.15% to 1.52% from ‘well-packed’ to ‘resettled’. evap-x-T-

color. The CFD-DEM formulation maintains calculations of pebble-pebble interactions while dynamically coupling to the helium flow. The model demonstrates the ability of helium gas to smooth out any hot spots predicted by pure-conduction DEM formulations. Further, the lattice-Boltzmann simulation, while not fully coupled to DEM, revealed important features of helium flow in volumetrically heated pebble beds – mainly the smearing of temperature profiles along the paths of cooling.

CHAPTER 11

LBM studies

CHAPTER 12

CFD-DEM Application

CHAPTER 13

Background experimental studies

Many experiments were carried out on individual ceramic pebbles. While there are some measures from experiments that are immediately useful for qualitative comparisons, such as the crush strength between different batches of ceramics, most values are not obviously connected to analysis of the pebbles nor the pebble bed assemblies they make up. In this section we will show had careful examination of single pebble experiments can lead to predictions of not only strength in ensembles but also modifications of the fundamental properties of the ceramic pebbles.

In section § 13.1, we use single pebble experiments to validate the use of Hertz theory for contacting ceramic pebbles, but also determine the proper Young's modulus to use for the ceramics. In section § 13.2 we use the theory we developed in section § 13.2 along with experimental data to begin to make predictions for survivability of pebbles in ensembles.

13.1 Elasticity reduction factor

In the study of individual pebble crush force (see § 13.1), the force-travel response curves of ceramic materials consistently exhibit distributions in the stiffness of the pebbles. For example, see the results of different lithium ceramic pebbles in Fig. 13.7. For DEM studies, we claim that interaction between these pebbles is well-represented by the Hertzian normal force as derived in § 3. For the discussion, we rewrite Eq. 3.16 here,

$$F_{n,ij} = \frac{4}{3} E_{ij}^* \sqrt{R_{ij}^*} \delta_{n,ij}^{3/2} \quad (13.1)$$

where δ is the overlap between contacting spheres and $\frac{1}{E^*} = \frac{1-\nu_i^2}{E_i} + \frac{1-\nu_j^2}{E_j}$, $\frac{1}{R^*} = \frac{1}{R_i} + \frac{1}{R_j}$. The contact force is directly proportional to the pair Young's modulus, E^* . Thus an accurate value of pebble Young's modulus is critical for an accurate calculation of contact force. For brevity, we do not include many details on DEM, but refer the reader to the original paper by Cundall and Strack¹⁵ upon which all modern models are based.

We now present Hertz equation as it applies to a pebble, diameter of d_p , being pressed between two flat anvils with measured travel of one anvil as s :

$$F_n = \frac{1}{3} E^* \sqrt{d_p s^3} \quad (13.2)$$

and $\frac{1}{E^*} = \frac{1-\nu_p^2}{E_p} + \frac{1-\nu_a^2}{E_a}$. Where the subscript p refers to pebbles and a the anvils.

From Eq. 13.2, we see that standard Hertz theory, where we use a single value for Young's modulus from literature, is not appropriate for pebbles studied in ceramic breeders. If single values of E_p and ν_p are employed, then variation in pebble diameters can not alone explain the variation of curves of Fig. 13.7.

13.1.1 Elasticity reduction factor

We propose to explain the behavior of individual pebbles (as in Fig. 13.7) with an assumption that the production technique yields pebbles with slightly different internal structures. The differences in internal structure then cause the pebble to have a different apparent modulus of elasticity; which will vary from some strong limit value. The strong value is the elastic modulus of highly sintered pellets reported in literature for the material, E_{bulk} . Assuming this strong value is the upper limit, imperfections in the pebbles will lead only to a reduction in this value. To quantify the deviation from the bulk, we introduce a k factor, defined as the elasticity reduction factor:

$$k = \frac{E_{\text{peb}}}{E_{\text{bulk}}} \quad (13.3)$$

where $k \in [0, 1]$.

If each pebble has a unique k value, this would quantify the spread in elastic responses seen in the experiments. The value is found by assuming that the pebbles are, in fact, behaving in a Hertzian manner, allowing us to back-out its k value, or in other words the unique E^* of that pebble by finding a best fit to the experimental curves.

From room temperature, we take the sintered pebble value for these Li_4SiO_4 pebbles to be $E_{\text{bulk}} = 90 \text{ GPa}$ and $E_{\text{bulk}} = 124 \text{ GPa}$ for Li_4SiO_4 pebbles. Then we iterate over all values of $k \in [0, 1]$ and compare the Hertzian response to that pebble's force-displacement curve.

The data of Fig. 13.7a is fit in the manner described and the pebbles are all plotted against Hertzian curves with their own unique modified Young's modulus in Fig. 13.1. The modified Hertzian curves with apparent Young's modulus fits well with most of the pebbles' curves. Similar data is obtained for the pebbles of Fig. 13.7b but the results are omitted for conciseness.

One of the benefits of using DEM simulations is the ability to predict pebble cracking in an ensemble based on knowledge of the interaction forces. If we are over-predicting the contact forces based on inaccurate material properties, we are going to be over-predicting the impact of pebble cracking as well. An accurate description of the material properties is an important feature for ceramic breeder designers.

We will apply the modified Young's modulus distributions to pebble beds and compare the results to pebble beds simulated with standard Young's modulus from literature.

We introduced Hertz theory in § 3, and now we apply it to experiments for analysis of ceramic pebbles. The derivation of Hertz force can be found on page 48 but is given again here for reference.

$$F = \frac{4}{3} E^* \sqrt{R^*} \delta^{3/2} \quad (13.4)$$

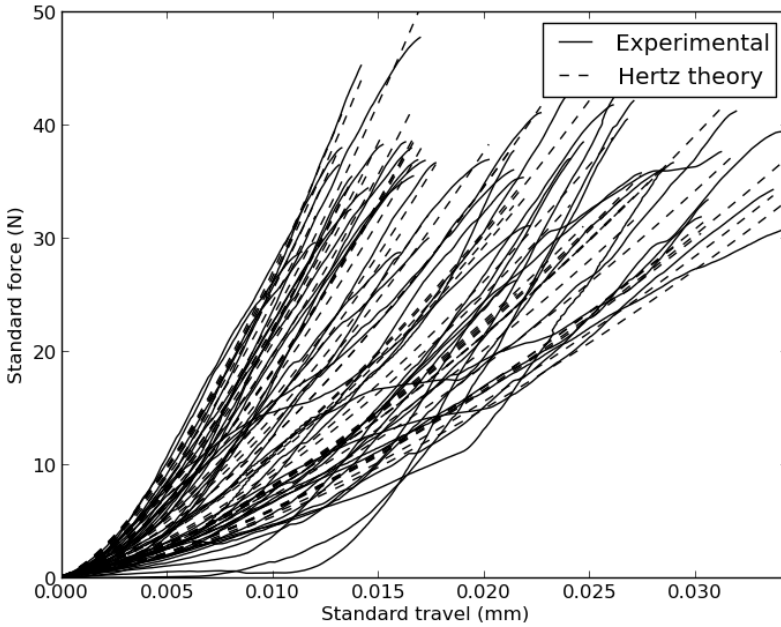


Figure 13.1: Experimental responses (solid) and fit curves of Hertzian equivalent with apparent Young's modulus (dashed).

and, again, the relative Young's modulus and radius are

$$\begin{aligned}\frac{1}{E^*} &= \frac{1 - \nu_i^2}{E_i} + \frac{1 - \nu_j^2}{E_j} \\ \frac{1}{R^*} &= \frac{1}{R_i} + \frac{1}{R_j}\end{aligned}$$

In experiments where we press a ceramic pebble between two platens, we measure the travel, s , rather than the pebble overlap, so we modify Eq. 3.16 to be represented in terms of travel ($s = 2\delta$). Furthermore, for a pebble ($R_i = R_p$) in contact with a smooth plane ($R_j \rightarrow \infty$), the relative radius is simply $R^* = R_p = d_p/2$.

The Hertz force is now expressed as

$$F = \frac{1}{3} E^* \sqrt{d_p s^3} \quad (13.5)$$

Let's take a moment to discuss Eq. 13.5. The Young's modulus of the test stand platen

is a constant value. One might assume the Young's modulus of the ceramic is also a known, constant value. In that case, there should be only a single force response for every pebble of a given diameter. Using the material properties given in Ref.²⁸ for Li_2TiO_3 , we plot a set of parametric curves based on diameter. The properties used for an nickel-alloy platen and Li_2TiO_3 are given in Table 13.1. The curves are given in Fig. 13.2.

Table 13.1: Material properties used for Li_2TiO_3 and nickel-alloy platen

E_{peb} (GPa)	ν_{peb}	E_{stand} (GPa)	ν_{stand}
126	0.24	220	0.27

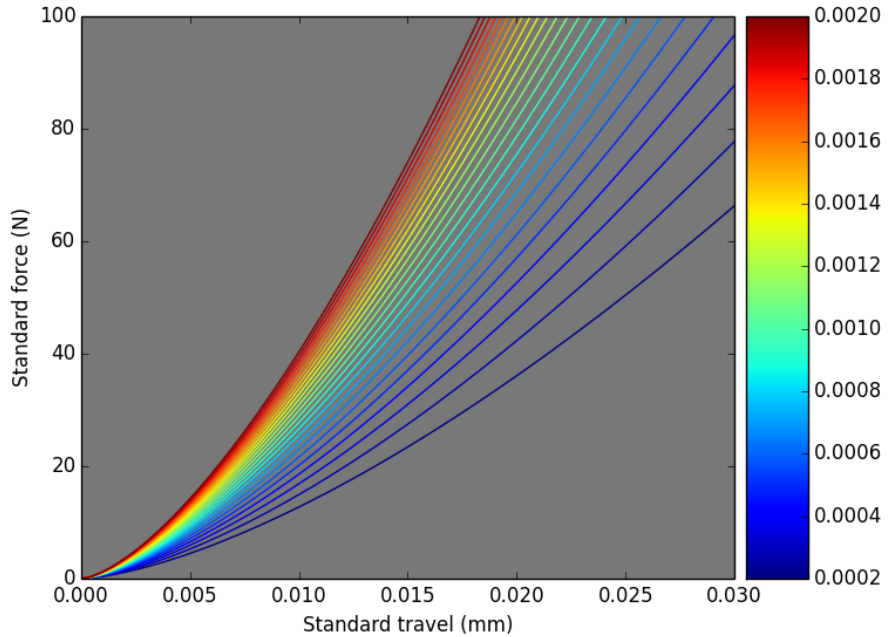


Figure 13.2: Hertzian responses of Li_2TiO_3 pebbles compressed between platens. The colormap shows pebble diameters in m. The diameters span an order of magnitude from $d_p = 0.2\text{mm}$ to $d_p = 2\text{mm}$.

Figure 13.2 clearly shows that if a pebble of a given diameter is strictly obeying Hertz

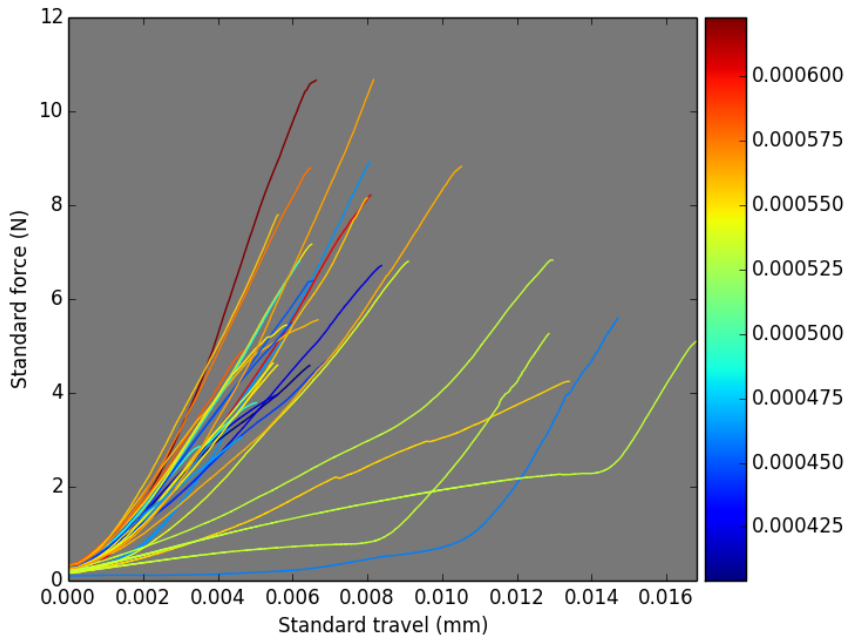
theory, there is only a single force-displacement curve it can follow. However, when experiments are performed on single pebbles we see quite different behavior for the F-s curves, see the curves of Fig. 13.3.

Figure 13.3a shows Li_4SiO_4 pebbles as they are compressed between platens. Neglecting the handful of pebbles with very low force responses to high strain, there is a grouping of pebbles where there is a general trend that matches Fig. 13.2. The smaller diameter pebbles, in blue colors, have lower force responses for a given strain. Larger pebble diameters, in yellow-orange, are slightly higher overall in their force response. Finally, the largest diameter pebble in dark red has the highest force response for a given diameter. However, while the trends are *generally* similar to the theoretical Hertzian curves, there are noticeable spreads in responses. The responses of Li_2TiO_3 pebbles of Fig. 13.3b, on the contrary, show almost no adherence to the expected diameter dependence of Hertz theory.

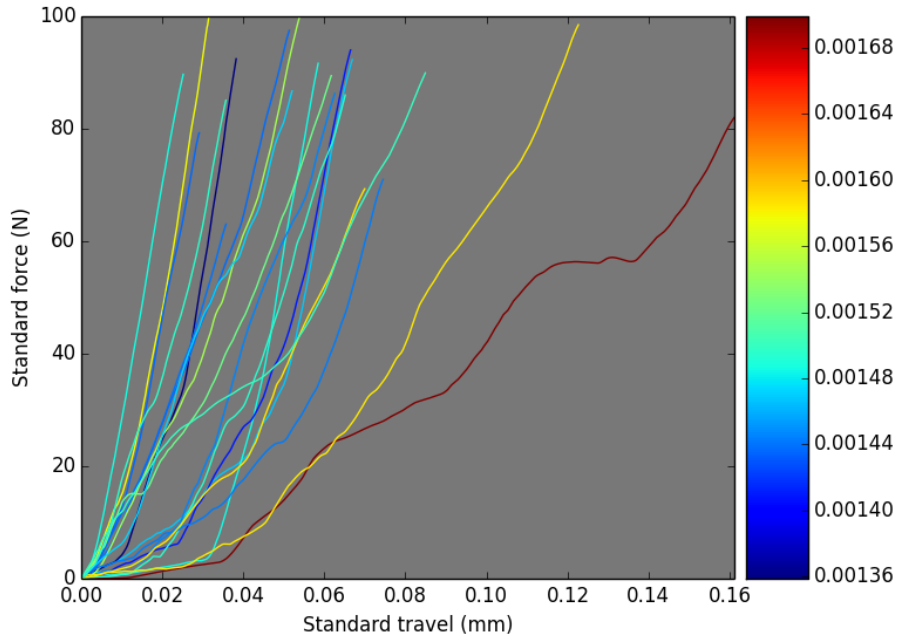
The behavior of pebbles observed in Fig. 13.3 lead us to conclude that variations in pebble diameter can not alone account for the variation in the F-s curves. The most reasonable source for a variation is in the Young's modulus of pebbles in a batch. Such a conclusion is important for implementation of Hertz theory in DEM algorithms.

We hypothesize that variation in the apparent Young's modulus of each pebble is rooted in the production of the pebbles which yields pebbles with slightly different internal structures. The differences in internal structure then cause the pebble to behave with different stiffnesses than the value expected from measurements of sintered pellets of lithium ceramics. In fact, we consider the sintered pellet Young's modulus, E_{sp} , as the upper limit for the pebbles and that most will emerge with values less than E_{sp} . To quantify the deviation of each pebble's E_{peb} from the sintered pellet, we introduce a k factor, defined as the elasticity reduction factor:

$$k = \frac{E_{\text{peb}}}{E_{\text{sp}}} \quad (13.6)$$



(a) Li_4SiO_4 pebbles of approximately 0.5mm diameter.



(b) Li_2TiO_3 pebbles of approximately 1.5mm diameter.

Figure 13.3: Force-displacement curves for two sets of experimental data, a batch of Li_4SiO_4 pebbles and a batch of Li_2TiO_3 pebbles. The colormap shows pebble diameters in m.

where

$$k \in [0, 1]$$

If each pebble has a unique k value, this would quantify the spread in elastic responses seen in the experiments. We find the value by assuming that the pebbles are, in fact, behaving in a Hertzian manner. This allows us to back-out a k value, or in other words the unique E_{peb} of that pebble by finding a best fit to the experimental curves.

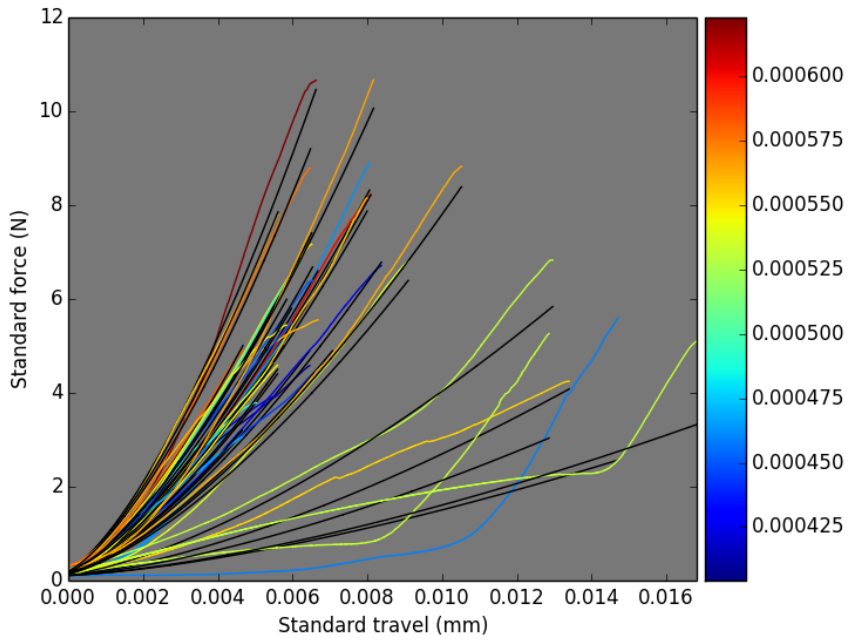
We take the sintered pebble value of Young's modulus for Li_4SiO_4 to be $E_{\text{sp}} = 90\text{GPa}$ and the value for Li_2TiO_3 to be $E_{\text{sp}} = 124\text{GPa}$. Then we iterate over all values of $k \in [0, 1]$ and compare the Hertzian response to that pebbles force-displacement curve. At each iteration, the L2-norm of the difference between Hertzian and experimental curves is used as the 'error'. The L2 norm, A for a given array, a is

$$\|A\|_F = \left[\sum_{i,j} \text{abs}(a_{i,j})^2 \right]^{1/2} \quad (13.7)$$

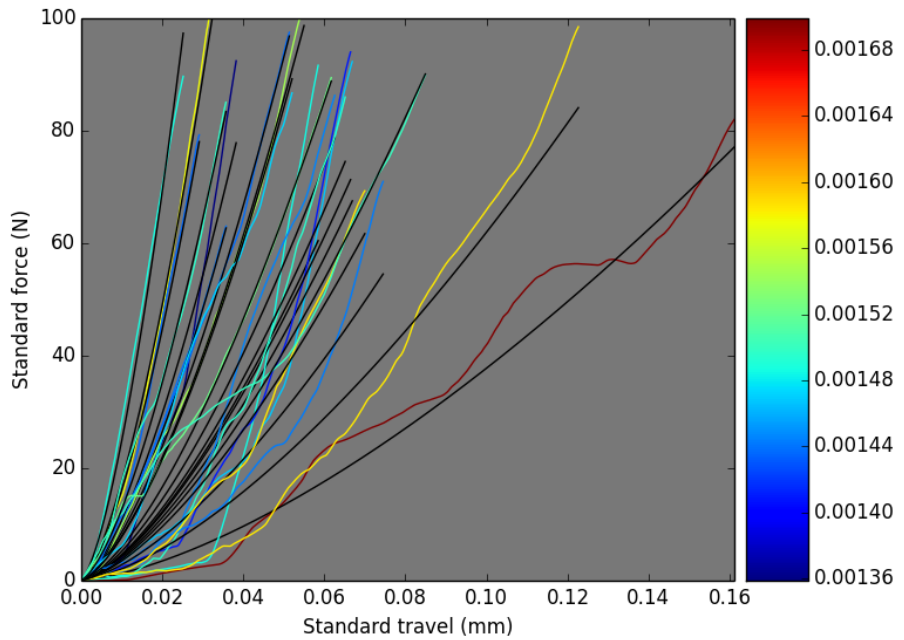
This is a convenient way to compare the error at every point along the force-displacement curves. When the error is minimized, the elasticity reduction value corresponding the minimum is recorded for that pebble. The Hertzian curves (in black) for each pebble are plotted in green against the experimental curves in Fig. 13.4.

Many of the curves in Fig. 13.4a seem to be fit well with a Hertzian curve with modified Young's modulus. The value of Young's modulus found for each pebble is plotted in Fig. 13.5. The Young's modulus of pebble numbers 0 to 4 are the very 'soft' pebbles seen with very low forces on Fig. 13.4a. The majority of pebbles behave with a Young's modulus between 30 and 70 GPa. On the upper end, a few pebbles acted very similar to their sintered pellet counterpart with approximate value of 90GPa.

What remains is actually using these modified Young's modulus in DEM simulations to see if they more accurately reflect pebble bed macroscopic behavior. If so, it is assumed they will more accurately reflect the contact forces between pebbles in the ensemble.



(a) Li_4SiO_4 pebbles of approximately 0.5mm diameter.



(b) Li_2TiO_3 pebbles of approximately 1.5mm diameter.

Figure 13.4: Force-displacement curves for two sets of experimental data, a batch of Li_4SiO_4 pebbles and a batch of Li_2TiO_3 pebbles. The colormap shows pebble diameters in m.

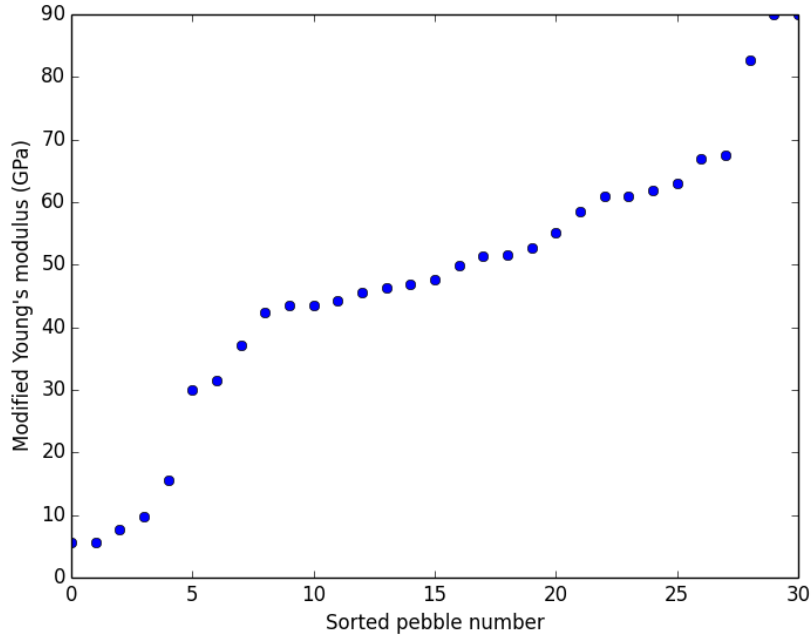


Figure 13.5: Distribution of modified Young's modulus for a batch of Li_4SiO_4 pebbles. Most pebbles responded to compression with a Young's modulus well below the sintered pellet value of 90GPa.

13.2 Strain energy measurements

13.3 Linking interactions with strain energy

Hertz theory is applicable to any two contacting elastic objects. In practice, we cannot probe the contacts of small particles and rely on experiments where we press pebbles between flat platens. Here we will develop a theory for connecting the results of the experiments with the interaction of two spherical objects.

To relate the situation in the lab to two particles, we first integrate the Hertzian force along the overlap to find the strain energy, W_ϵ , of that contact.

$$W_\epsilon = \int_0^{\delta_c} F_n(\delta') d\delta' \quad (13.8)$$

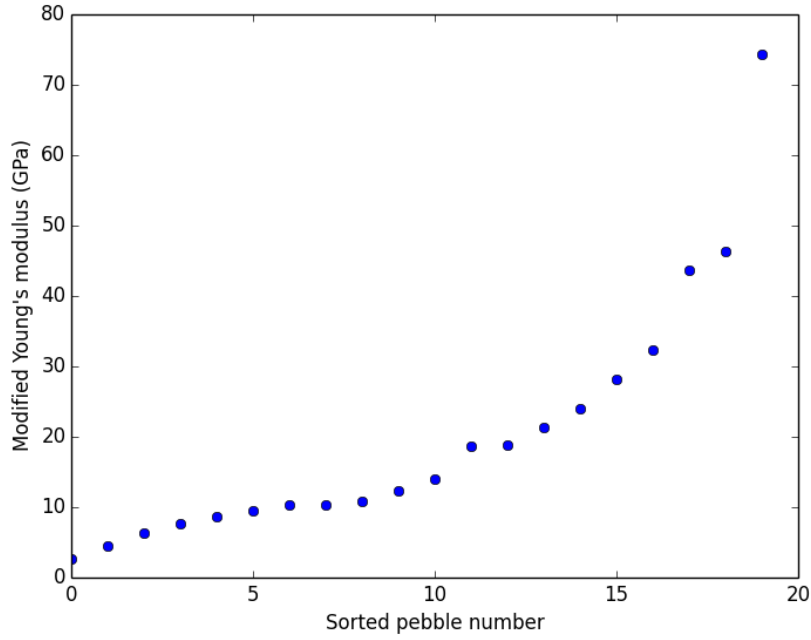


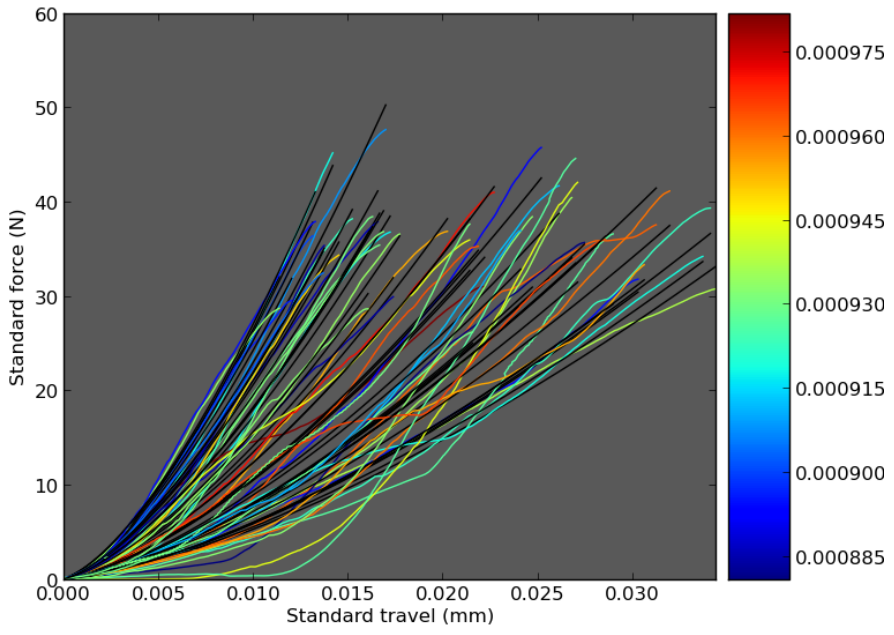
Figure 13.6: Distribution of modified Young's modulus for a batch of Li_2TiO_3 pebbles. All pebbles responded to compression with a Young's modulus well below the sintered pellet value of 126GPa.

where the upper limit of the integration is the critical overlap δ_c (the meaning of this value will be explained in detail later). With the force defined from Eq. 3.16, this is straightforward to integrate.

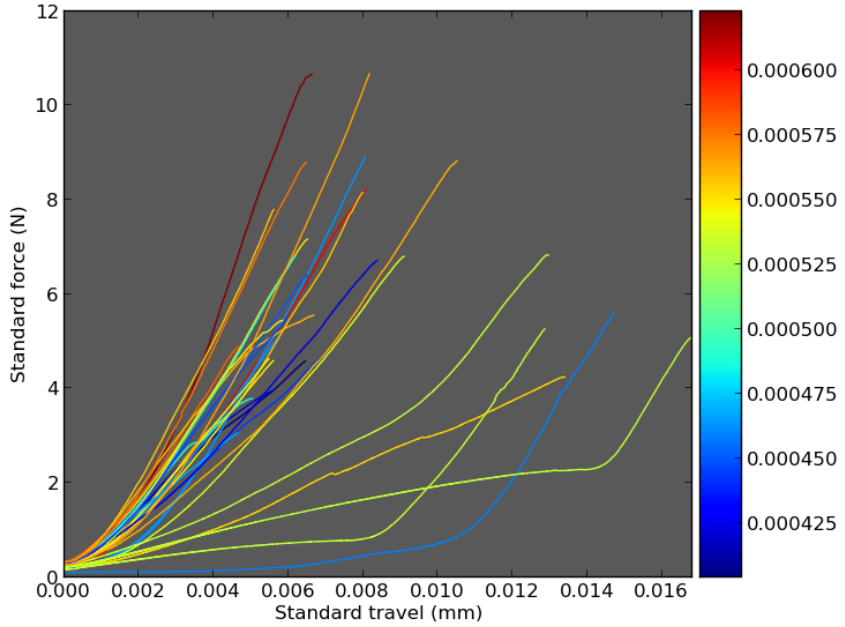
$$W_\epsilon = \int_0^{\delta_c} \frac{4}{3} E^* \sqrt{R^*} \delta'^{3/2} d\delta' \quad (13.9)$$

$$W_\epsilon = \frac{8}{15} E^* \sqrt{R^*} \delta_c^{5/2} \quad (13.10)$$

We will call the strain energy of the pebble compressed between platens as the lab strain energy, $W_{\epsilon,L}$. The strain energy of two particles in contact will be $W_{\epsilon,B}$. The assumption we make is that, if each interaction is integrated to the proper critical overlap, the strain energies will be equal at that point.



(a) Li_2TiO_3 pebbles of $d_p = 1 \text{ mm}$.



(b) Li_4SiO_4 pebbles of $d_p = 0.5 \text{ mm}$.

Figure 13.7: Force-travel responses of various lithiated ceramic pebbles of disparate diameters show similar behavior in distributions of responses. The colormaps differentiate the pebbles by diameter (in meters).

$$W_{\epsilon,L} = W_{\epsilon,B} = \frac{8}{15} E_B^* \sqrt{R_B^*} \delta_{c,B}^{5/2} \quad (13.11)$$

We solve for the interacting particle overlap as a function of the lab strain energy as

$$\delta_{c,B} = \left[\frac{15W_{\epsilon,L}}{8E_B^* \sqrt{R_B^*}} \right]^{2/5} \quad (13.12)$$

This overlap can be reinserted to Eq. 3.16 to find the critical force of the interacting particles as a function of the critical strain energy of the lab. Doing this, we find:

$$F_{c,B} = C E_B^{*2/5} R_B^{*1/5} W_{\epsilon,L}^{3/5} \quad (13.13)$$

where $C = \frac{4}{3} \left(\frac{15}{8} \right)^{3/5}$.

In this analysis we have referred to a ‘lab’ and ‘particle’ for the two situations. In fact, the result is more general and can be used to relate any two scenarios. The only requirement is that both conditions adhere to the assumptions of Hertz theory. The ramifications of this relationship will be explored in more detail in § 13.

13.3.1 Pebble crushing predictions

Along with proper material properties, we present a relationship to translate between the experimental data of crush force to a value that can be applied to DEM simulations. We relate crush force experimental data to predictions of crushing pebbles in an ensemble with:

$$F_{c,B} = \frac{4}{3} \left(\frac{15}{8} \right)^{2/5} (R_B^*)^{1/5} (W_{\epsilon,L})^{3/5} \quad (13.14)$$

where $W_{\epsilon,L}$ is measured strain energy at the point of crushing from the experiment. This value follows a probability distribution and therefore imparts a distribution shape to the $F_{c,B}$ prediction. At the peak load of 6 MPa we use the above prediction to determine how many pebbles would be cracking at this state of external pressure

CHAPTER 14

Background numerical studies

14.1 Study of Young's Modulus

The discrete element method is used by many ceramic breeder researchers to model the interaction of individual pebbles in an ensemble in an effort to obtain a more detailed understanding of pebble beds than is possible with experimental measurements of effective properties. For example see Refs.^{2,3,25,39,60,68} A major assumption in the DEM formulation is that each pebble acts perfectly elastically and adheres to Hertz theory for contacting spheres. With Hertz theory, one finds contact forces as a simple function of: the virtual overlap between two objects, the Young's modulus of the contacting material (and Poisson ratio), and radii of the two. In past studies, the Young's modulus of the ceramic materials used in DEM simulations was taken from historical data, for instance lithium metatitanate from Ref.²⁸

The fundamental assumption in the DEM formulation is that each pebble acts perfectly elastically and thereby adheres to Hertz theory for contacting spheres. With Hertz theory, one finds contact forces as a simple function of: the virtual overlap between two objects, the Young's modulus of the contacting material (and Poisson ratio), and radii of the two. In past studies, the Young's modulus of the ceramic materials used in DEM simulations was taken from historical data, for instance lithium metatitanate from Ref.²⁸

Based on observations of experimental data from single pebble crush data, in this study we propose a new method of obtaining the Young's modulus for a batch of ceramic pebbles as the historical values from literature are not always appropriate. Details of the motivation

and physics are in § 13.1.

14.1.1 Numerical experiments setup

We model our pebble beds undergoing a standard stress-controlled uni-axial compression up to 6 MPa. We will measure the macroscopic stress-strain for some parametrically varied pebble beds and compare the curves. At the moment of maximum stress, we can investigate the differences in contact forces of those pebble beds.

Our pebble ensemble is composed of 0.5mm diameter lithium orthosilicate pebbles. The pebble beds are initiated and packed in the same manner as § 9.1. There are two main bed groups. Set A: the first set of three beds (A.1-3) contain a single type of pebble with $E = 90\text{GPa}$. Set B: the second set of four beds (B.1-4) contain ten types of pebbles with their Young's modulus assigned in a discrete, random way to satisfy the distribution seen from experimental data. For the DEM study, we fit to lithium orthosilicate pebbles where the average stiffness was $\bar{E} = 49 \text{ GPa}$. The description of the two sets of pebble beds is visually represented in Fig. 14.1. The pebble bed geometry was also the same used in the study of Ref.;⁶⁰ two virtual walls in the x-direction located at $x_{\lim} = \pm 20R_p$, periodic boundaries at the limits of $y_{\lim} = \pm 15R_p$, and a total of 8000 pebbles packed into the volume to an approximate height of $z_{\lim} = 20R_p$.

Among both sets, a parametric study was done on pebble radius and coefficient of friction. The radii of pebbles in beds A.1, A.2, B.1, and B.2 were constant at $R_p = .25 \text{ mm}$. The radii of pebbles in beds A.3, B.3, and B.4 followed a Gaussian distribution about $\bar{R}_p = 0.25 \text{ mm}$: $\mu_d = R_p$ and $\sigma_d = R_p$. The coefficient of friction was set at $\mu = 0.2$ for beds A.1, A.3, B.1, and B.3; the coefficient of friction was $\mu = 0.3$ for beds A.2, B.2, and B.4.

14.1.2 Results

A constant-velocity, uniaxial compression was applied to the pebble beds. A single cycle up to 6 Mpa was used on all the beds. The macroscopic measurements of stress-strain are

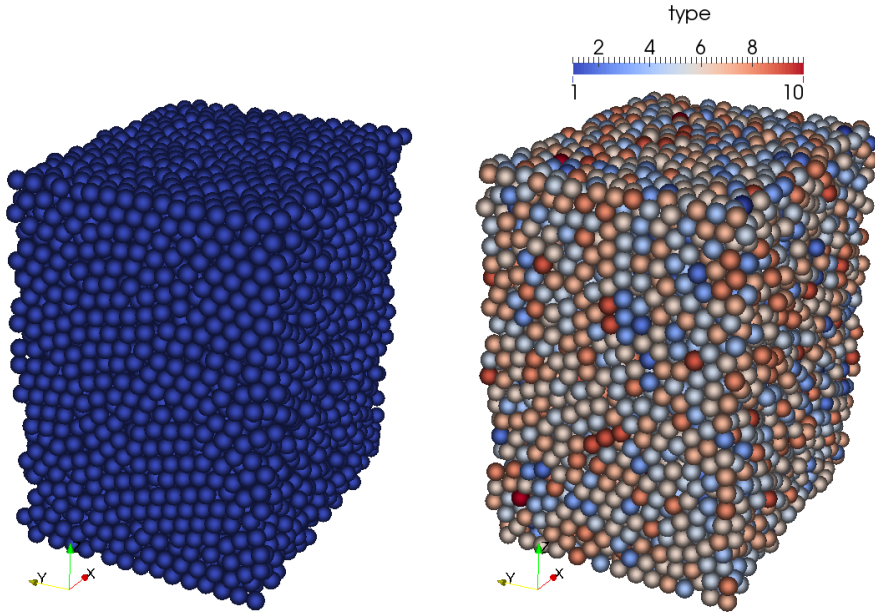


Figure 14.1: [color online] On the left, set A, a pebble bed with a single type, of $E = 120$ GPa. On the right, set B, is a pebble bed with 10, randomly distributed types; each type corresponds to a reduced, apparent Young's modulus as derived from experimental data.

shown for all the pebble beds in Fig. 14.2.

Naturally, the pebble beds with smaller Young's modulus (with circle markers) are more compliant to external loads. The result is true regardless of the coefficient of friction or distribution of pebble radius studied here. Group B moved to an average strain of about 2.6% at 6 MPa, by comparison the beds of Group A only had strained 1.9 % on average to reach the same stress. Among the beds of each group, pebble beds with constant radius pebbles behaved virtually the same as similar pebble beds with a Gaussian distribution on radius. An increase in the coefficient of friction had a moderate impact on the overall stress-strain response.

The parametric study here shows that the largest contributor to stress-strain response is the Young's modulus. The coefficient of friction and radius distribution had comparatively insignificant influence. A pebble bed geometry more directly comparable to oedometric

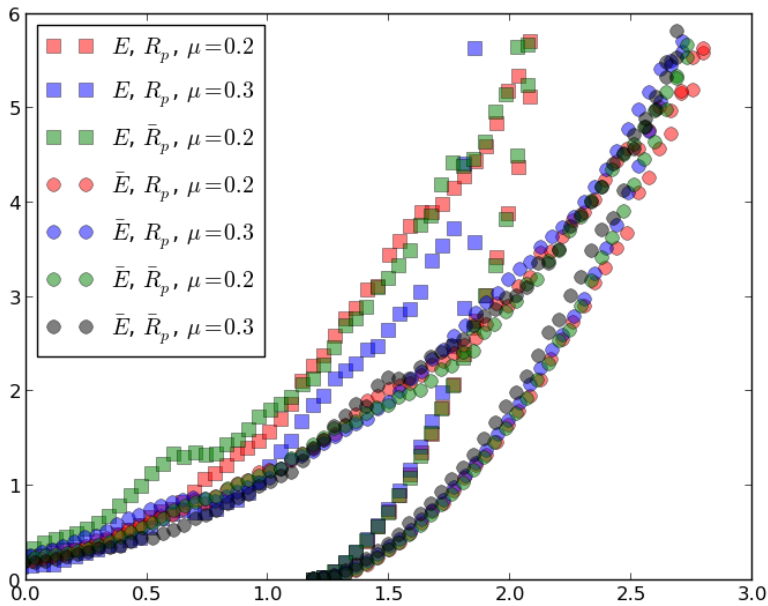


Figure 14.2: [color online] Stress-strain responses of pebble beds with: squares, constant Young's modulus; and circles, Gaussian distribution of Young's modulus. The constant Young's modulus beds all had much firmer responses for all parametric cases studied here.

compression experiments should be used to allow direct comparison and validation of the numerical models.

At the point of peak stress for each bed, we use DEM results to visualize the distribution of contact forces among all pebbles in the ensemble. A plot of the probability distributions of all the beds together, Fig. 14.3, shows that the majority of the contacts in all the beds are equally small. There are a few overall trends we observe from the results however. The pebble beds with the constant Young's modulus are always higher for their comparable version with distributed Young's modulus. For pebble beds with comparable Young's moduli and radii, higher coefficients of friction generally have higher peak contact forces. Pebble beds' radius distributions have much less impact on peak contact forces than either coefficient of friction or Young's modulus. Another method of comparing overall contact force distributions is to consider predictions on pebble cracking which assigns a strength value at random to pebbles

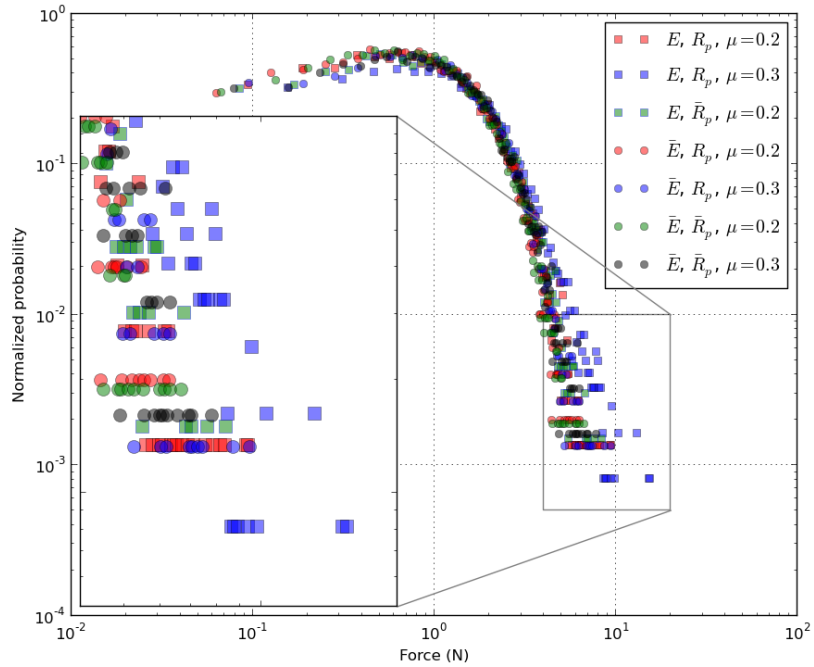


Figure 14.3: [color online] Probability distribution of contact forces in all the pebble beds studied here. Elastic moduli value is the largest contributor to higher peak contact forces among pebbles.

in the bed, according to Eq. 13.14. At the point of maximum stress, this is done and the results are shown in Tab. 14.1.

While overall the predicted number of broken pebbles is small, we compare similar parameteric pebble beds and in each case pebble beds with modified Young's modulus overall predict smaller percentages of broken pebbles. Pebble crushing is a major topic for the overall evaluation of the feasibility of ceramic pebble beds in fusion reactors. This study reveals that past DEM work on pebble crushing was likely over-predicting the extent of crushing if the Young's modulus used in the study was much larger than the realistic response of individual pebbles.

Table 14.1: Comparisons for the two styles of Young’s modulii used in the study.

Bed label	Parameters	Predicted crushed %
A.1	$E, R_p, \mu = 0.2$	0.3
A.2	$E, R_p, \mu = 0.3$	1.0
A.3	$\bar{E}, \bar{R}_p, \mu = 0.2$	0.9
B.1	$\bar{E}, R_p, \mu = 0.2$	0.6
B.2	$\bar{E}, R_p, \mu = 0.3$	0.8
B.3	$\bar{E}, \bar{R}_p, \mu = 0.2$	0.4
B.4	$\bar{E}, \bar{R}_p, \mu = 0.3$	0.7

14.1.3 Conclusions

Models based on the discrete element method have received considerable attention by ceramic breeder researchers. The method is attractive as it is based on material properties and forgoes many of the assumptions necessary in empirical equations of effective properties for continuum models. Variation in production techniques for ceramic pebbles lead to changes in ceramic microstructure, as evident in the wide distribution of crush loads reported in past studies, *e.g.* Refs.^{43,70} By the same token, the different microstructures should naturally lead to variation in Young’s modulus. However up to now values of Young’s modulus used in numerical models are taken from values measured for large sintered pellets of ceramic materials. Based on single pebble experiments and the application of Hertz theory, a technique for introducing a modified Young’s modulus into DEM models has been proposed here. DEM simulations show the impact of modified pebble elasticity on both macroscopic measurements of stress-strain curves as well as mesoscopic measures of inter-pebble contact force – with major implications for prediction of pebble crushing in ceramic pebble beds. The models applying the elasticity reduction factor, k , predict more compliant pebble beds

and smaller peak contact forces in beds and thus fewer crushed pebbles.

14.2 Jeffeson correction to lumped capacitance method

In § 5.2, we discuss correlations for heat transfer coefficients of spheres in a packed bed. Then those correlations are utilized with CFD-DEM computational routines in eq. (7.2). When implemented in the DEM-based modeling, we make the lumped capacitance assumption for each particle in the ensemble. The assumption eases the computational efforts of solving for the temperature distribution inside each particle; each particle is treated as isothermal. The accuracy of the lumped capacitance method is described by the Biot number,

$$\text{Bi} = \frac{hd_p}{k_r} \quad (14.1)$$

and for $\text{Bi} \ll 1$ the lumped capacitance method accurately models the behavior of a solid interacting with a fluid. For $\text{Bi} \approx 0.1$, the error from the lumped capacitance method is only about 5%. In solid breeder volumes, the particles are generally small, solid conductivity low, and heat transfer coefficient generally also low. This leads to small-to-moderate Biot numbers expected in the packed bed. In this section we will analyze the accuracy of the lumped capacitance and introduce a correction method to account for inaccuracies of the method at moderate Biot numbers.

We simplify the case of a packed bed and only consider a single sphere with volumetric heat generation submerged in and thermally interacting with a fluid. The sphere will be of radius $R = d_p/2$, as shown in Fig. 14.4. The sphere will initially be at a uniform temperature of T_i . The fluid temperature will remain constant at T_f

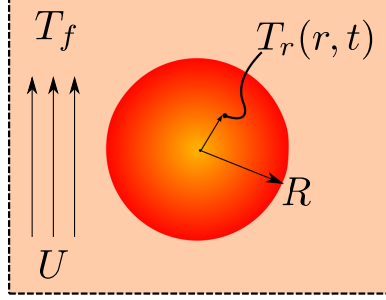


Figure 14.4: CONTROL VOLUME OF A SINGLE SPHERICAL PARTICLE IN A PACKED BED

14.2.1 Lumped capacitance solution for sphere

We will solve for a single sphere interacting with a passing fluid, as shown in Fig. 14.4. We make the lumped capacitance assumption for this sphere. The solid is initially at temperature T_0 , with constant volumetric heat generation, cooling in a fluid with constant heat transfer coefficient. The fluid will remain constant at T_f .

The time response of the sphere's temperature is dictated by the balance of energy to/away from the solid,

$$\rho_r C_r V \frac{dT}{dt} = -hA(T - T_f) + gV \quad (14.2)$$

Eq. 14.2 is solved in dimensionless form with the following nondimensional parameters of temperature and time,

$$\theta = \frac{T(t) - T_f}{T_0 - T_f} \quad (14.3a)$$

$$\tau = \frac{t}{R^2/\alpha} \quad (14.3b)$$

where α is the thermal diffusivity of the sphere, T_0 is the initial isothermal temperature of the sphere, and T_f is the constant fluid temperature. The resulting temperature distribution is,

$$\theta_{LC} = \left(1 - \frac{G}{3\text{Bi}}\right) \exp(-3\text{Bi}\tau) + \frac{G}{3\text{Bi}} \quad (14.4)$$

where we define a dimensionless heat generation,

$$G = \frac{gR^2}{k(T_0 - T_f)} \quad (14.5)$$

The energy of the sphere, relative to the fluid, in nondimensional terms is

$$E^*(\tau) = \frac{E(\tau)}{E_0} \quad (14.6)$$

where E_0 is the initial energy of the sphere,

$$E_0 = \rho_r C_r V (T_0 - T_f) \quad (14.7)$$

Thus for a sphere with the lumped capacitance model, in nondimensional form, is simply

$$E_{LC}^*(\tau) = \theta_{LC}(\tau) \quad (14.8)$$

The nondimensional energy profile of Eq. 14.8 is plotted over the nondimensional time of $\tau \in [0, 1/\text{Bi}]$ in Fig. 14.5.

Reviewing Eq. 14.4 we see that the speed of decay is dictated by the term in the exponential, 3Bi . Meanwhile, the steady-state value being approached is given by $\frac{G}{3\text{Bi}} = \frac{gR}{h(T_0 - T_f)}$. It is important for this discussion to point out that because both the nondimensional heat generation and Biot number terms contain the solid conductivity, the steady-state value of the lumped capacitance model will not change for varying solid conductivity even if it leads to different Biot numbers. We will return to this point in the next section when we compare the lumped capacitance model to the exact solution when internal conduction of the solid is considered.

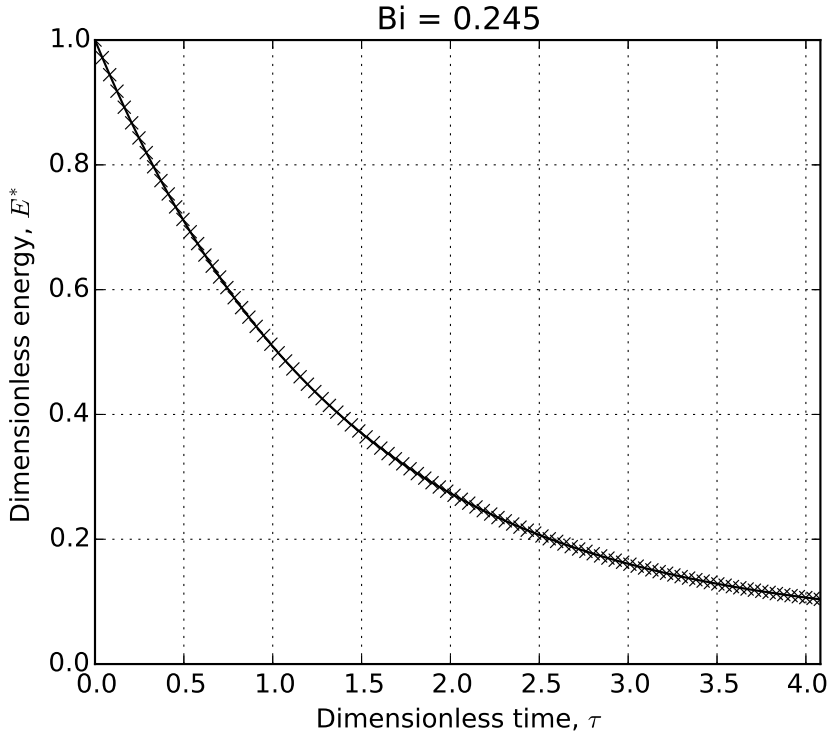


Figure 14.5: Lumped capacitance model: Sphere energy profile decaying from an initial value to a time of $1/Bi$

14.2.2 Exact solution for sphere

We again analyze the sphere of Fig. 14.4 but now will account for internal temperature gradients inside the sphere. The details of the analytic solution for a sphere with heat generation interacting with a fluid is given in Appendix A. We again solve in terms of the nondimensional temperature and time introduced in § 14.2.1 as well as a nondimensional radius,

$$\begin{aligned}\theta &= \frac{T}{T_0} \\ \rho &= \frac{r}{R} \\ \tau &= \frac{t}{R^2/\alpha}\end{aligned}$$

The energy conservation equation for the sphere with internal temperature gradient, in nondimensional form θ_{TG} , is

$$\frac{1}{\rho} \frac{\partial^2}{\partial \rho^2} (\rho \theta_{TG}) + G = \frac{\partial \theta_{TG}}{\partial \tau} \quad (14.9)$$

With the initial condition and boundary conditions outlined in Appendix A, the nondimensional temperature distribution inside the sphere is

$$\theta_{TG}(\rho, \tau) = \left(\frac{G}{6} + \frac{G}{3Bi} - \rho^2 \right) + \sum_{n=1}^{\infty} \exp(-\zeta_n^2 \tau) \frac{\sin(\zeta_n \rho)}{\rho} \frac{Z(\zeta_n)}{N(\zeta_n)} \quad (14.10)$$

where ζ_n are the eigenvalues of the equation and the functions of ζ_n (Z, N, C) are given in Appendix 14.2.2.

The accompanying nondimensional energy of the sphere is integrated to,

$$E_{TG}^*(\tau) = \left(\frac{G}{15} + \frac{G}{3Bi} \right) + 3 \sum_{n=1}^{\infty} \exp(-\zeta_n^2 \tau) \frac{Z(\zeta_n)}{N(\zeta_n)} C_n(\zeta_n) \quad (14.11)$$

We now compare the exact solution from Eq. 14.11 to the solution of energy given by the lumped capacitance model of Eq. 14.8. The two profiles are given in Fig. 14.6.

For the value of Biot number here, $Bi < 0.5$, the profile of the analytic solution of the sphere is well-captured by the lumped capacitance model. The maximum relative error over the time span, as defined by

$$\text{error} = \frac{|E_{TG}^*(\tau) - E_{LC}^*(\tau)|}{E_{TG}^*(\tau)} \quad (14.12)$$

is always less than 10%.

We consider now the same size sphere but with the Biot number increased by an order by: a) a conductivity of $k = k_r/10$ and b) a heat transfer coefficient of $h = 10h_f$. The two physical changes to the system result in the same Biot number but as we can see in Fig. 14.7, there are drastic changes in the results.

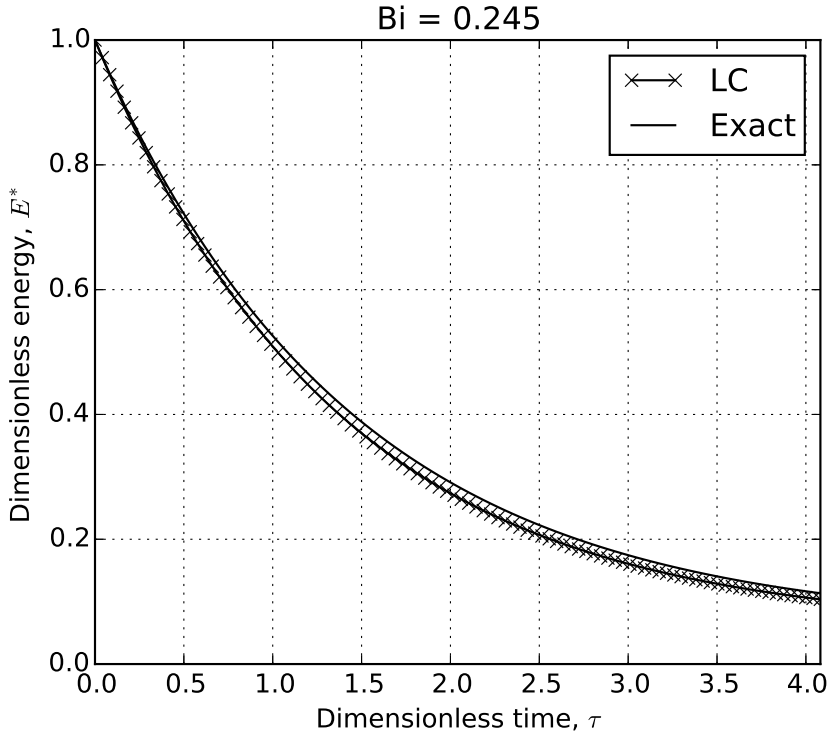


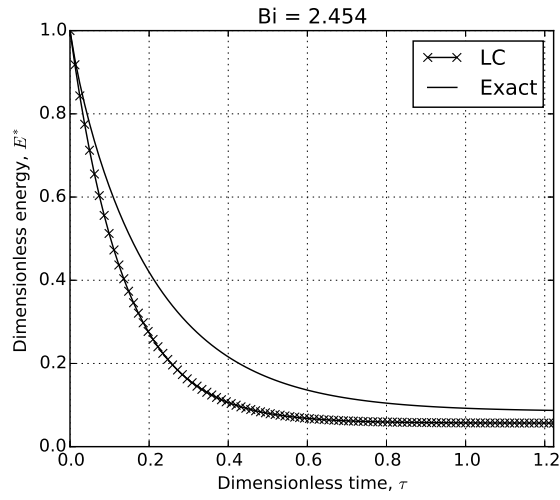
Figure 14.6: Analytic and lumped capacitance models: Sphere energy profile decaying from an initial value to a time of $1/\text{Bi}$

Seen in Fig. 14.7a, the lumped capacitance solution both over-predicts the speed at which the sphere reaches a thermal steady-state as well as the value of the steady-state. Comparatively, in Fig. 14.7b, for the same Biot number the lumped capacitance solution again over-predicts the speed to thermal steady-state by the same rate but is relatively accurate for the steady-state value itself.

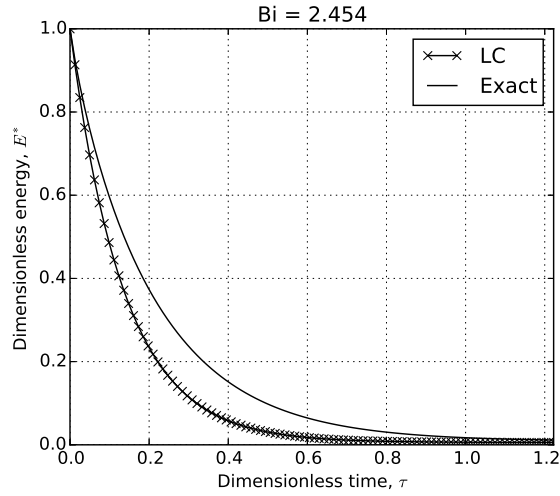
To first address the source of error on the steady-state value, we view the steady-state terms of the two solutions. From Eq. 14.11, we write the steady-state term of the exact solution as

$$E_{TG,ss}^* = \frac{G}{15} + \frac{G}{3\text{Bi}} \quad (14.13)$$

Comparatively, we write the steady-state term of the lumped capacitance solution from



(a) The Biot number increased from a decrease in the solid conductivity.



(b) The Biot number increased from an increase in the heat transfer coefficient.

Figure 14.7: Analytic and lumped capacitance models: Sphere energy profile decaying from an initial value to a time of $3/\text{Bi}$. The same Biot number produces different results for the exact solution of a sphere with heat generation.

§ 14.2.1 as,

$$E_{LG,ss}^* = \frac{G}{3\text{Bi}} \quad (14.14)$$

We clearly see that the two steady-state values differ by the contribution of $\frac{G}{15}$ on the exact solution. This term does not appear in the lumped capacitance solution because it does not account for the temperature difference through the sphere. The nondimensional heat generation term is given in Eq. 14.5; it is importantly a function of thermal conductivity but not the heat transfer coefficient. This explains the difference between steady-state values in Fig. 14.7 when we modified the two parameters.

To address the inaccuracies in the time-dependent response of the lumped capacitance method with large Biot number, we will make use of the so-called Jeffreson Correction described by Van Lew⁵⁹ and Xu et al.⁶⁵ In their work, they considered a heated heat transfer fluid interacting with a low conductivity thermal storage material. The solar thermal storage systems they analyzed often had moderate-to-large Biot numbers but they could continue to apply the lumped capacitance model by applying the Jeffreson Correction.³¹ The details of the Jeffreson correction as applied to a system with volumetric heat generation will be discussed next.

14.2.3 Jeffreson correction for sphere

In Fig. 14.7, the lumped capacitance model predicted a much faster decay to steady-state than the exact solution. Jeffreson summarized a correction to the lumped capacitance model via a reduction in the heat transfer coefficient as a function of the Biot number. The smaller heat transfer coefficient effectively slowed the decay to steady-state as predicted by the lumped capacitance method. The correlation to correct the heat transfer coefficient due to solids with large Biot number is given by Jeffreson.³¹ The Jeffreson correction for a sphere is,

$$h_p = \frac{h}{1 + Bi/5} \quad (14.15)$$

where h_p is the modified heat transfer coefficient of the particle with an internal temperature gradient. An increase in the Biot Number (or increase of thermal gradient inside the solid) results in a decrease in the heat transfer coefficient h_p . A modified Biot number can then also be written as

$$Bi_p = \frac{h_p d}{k_r} = \frac{Bi}{1 + Bi/5} \quad (14.16)$$

Applying the Jeffreson Correction to Eq. 14.4,

$$\theta_{JC} = \left(1 - \frac{G}{3Bi_p}\right) \exp(-3Bi_p\tau) + \frac{G}{3Bi_p} \quad (14.17)$$

and thereby Eq. 14.8 gives

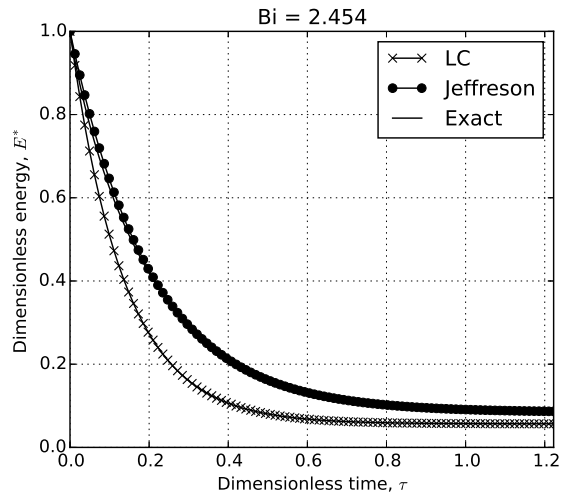
$$E_{JC}^*(\tau) = \theta_{JC}(\tau) \quad (14.18)$$

We then plot the energy profiles from the lumped capacitance model (LC), the Jeffreson correction (JC), and the exact solution together in Fig. 14.8

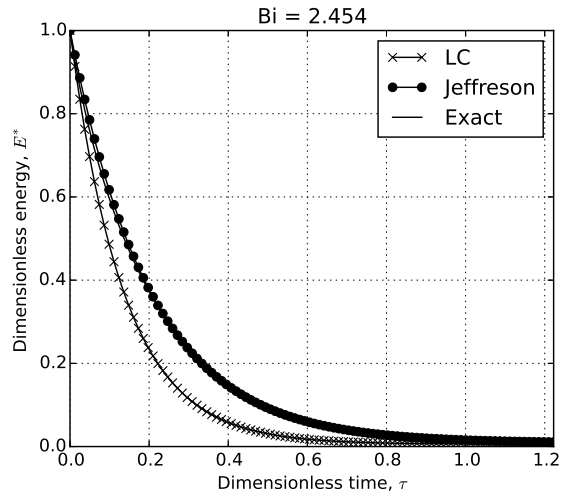
The Jeffreson correction to the lumped capacitance method allows the simple model to capture the proper transient as well as steady-state values for this sphere with a moderately sized Biot number. To look more closely, we view the instantaneous error (see Eq. 14.12) in Fig. 14.9.

For the value of $Bi > 1$ due to either low conductivity (Fig. 14.9a) or high heat transfer coefficient (Fig. 14.9b), the error in the Jeffreson correction is always under 10%; often closer to only 1%. This is in opposition to the standard lumped capacitance method which has 50-80% error for both transient and steady-state values.

The lumped capacitance method allows researchers to simplify transient, conjugate heat transfer problems with an isothermal solid. In the discrete element method, the assumption

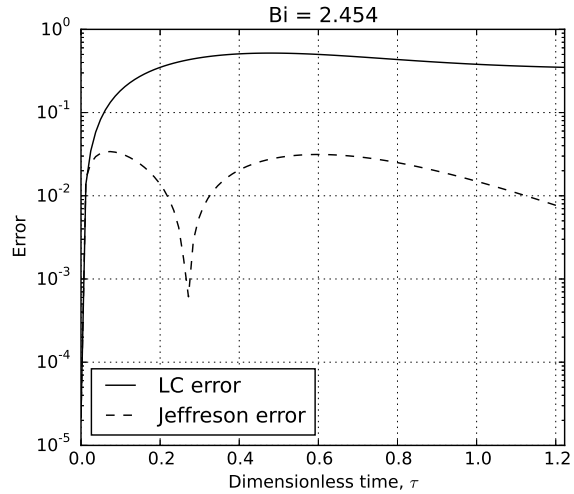


(a) The Biot number increased from a decrease in the solid conductivity.

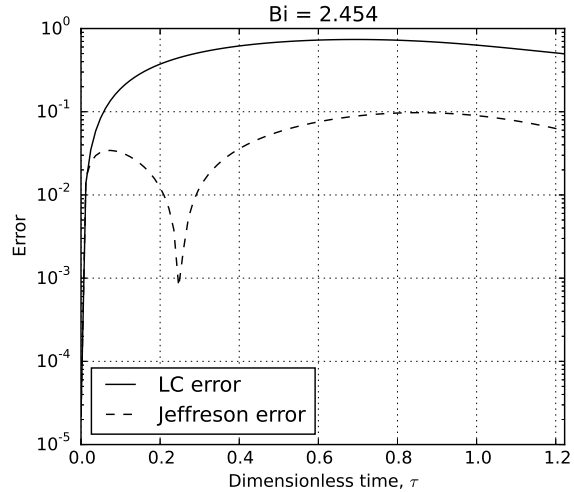


(b) The Biot number increased from an increase in the heat transfer coefficient.

Figure 14.8: Analytic, lumped capacitance model, and LC model with Jeffreson correction: Jeffreson correction corrects for transient and steady-state errors of lumped capacitance.



(a) The Biot number increased from a decrease in the solid conductivity.



(b) The Biot number increased from an increase in the heat transfer coefficient.

Figure 14.9: Error of lumped capacitance and reduced error of the model with Jeffreson correction for moderate Biot number.

of isothermal solid is innate in the framework of the method. With the implementation of the Jeffreson correction in the discrete element method, we have confidence in the fidelity of the heat transfer in for moderately sized Biot numbers. The Jeffreson correction will be implemented into the DEM computations via Eq. 14.16.

14.3 Pebble failure modeling

Research on pebble failure has been taken up by others in the fusion community (see § 14.3) to predict the onset of pebble crushing as a function of an external pressure and the resulting changes to mechanical properties such as the stress-strain of the pebble bed.

The discrete element method has been used for studies in a variety of fields for studying inter-particle forces and the homogeneously distributed force networks that arise in packed beds (for example, see Ref.⁴²). The discrete element method was also used in the fusion community to attempt to model failure initiation and propagation.^{3,69,70} They too observed that a relatively few number of high-force networks, distributed throughout the bed supported the external mechanical loads. The even distribution of the force networks was used to defend the development of a probability-based predictor for failure. We make use of the probability argument of Zhao, et al. for the current study.⁶⁹ Their basic premise is that probability distributions of strength curves for pebble crushing have been observed (see, for example crush loads of Ref.⁵⁶). Then in DEM models, a probability distribution of inter-particle forces are also observed. Overlaying the two probabilities resulted in seemingly random locations of pebbles satisfying the failure criteria – not strictly along the high-force chains running through packed beds.

We apply the theory of Zhao, et al. in the following manner. If pebbles fail at random locations, we may de-couple the task of predicting pebble failure (i.e. finding the mechanical or thermal load that causes a pebble to fail) from the task of modeling the ramifications of pebble failure. In our model, we begin with a starting point of a packed bed and then simply flag pebbles at random for ‘failing’. For our first model of failure, after a pebble has been flagged it is removed from the system entirely. The removal disrupts the meta-static state of

the ensemble and the remaining pebbles re-settle. In reality, the ceramic pebbles generally break into just a few large pieces that remain in the system. Under development is a method for recreating that behavior in the DEM domain, it will be reported in future studies.

14.4 Stability study

As mentioned when the integration algorithm was introduced in § 6.2, the velocity-Verlet algorithm is a computationally efficient, second-order accurate means of updating the kinematics of all the particles in the ensemble.³⁶ The timestep of the integration, however, must often be very small to ensure that it is less than the time taken for a pressure wave to propagate through the particle. The timestep is further constrained by the quasistatic assumption used to derive the Hertzian contact force such that inertial and relaxation effects may be neglected.⁶ We will also show that, in order to avoid heat energy to propagate further than a single pebble during a single timestep, the thermal timestep requirement is orders of magnitude larger than the mechanical timestep equivalent. And that the overall minimum timestep is thus driven by the mechanical stability.

In tandem with the requirement on very small timestep, the thermal time-constants in the ceramic breeder zones can be many hundreds of seconds. These two conditions seem to conspire to force an unacceptably large requirement on the number of timesteps for a thermal DEM simulation and thus make numerical experiments impractical.

In this section we will analyze the calculation of a critical timestep based on the speed of a Rayleigh wave propagating along the surface of a particle. Then, with that knowledge in hand, we will argue for scaling certain physical properties to allow for faster simulations without sacrificing fidelity to the real physics of the problem.

14.4.1 Critical dynamic timestep

If we wish to choose a timestep sufficiently small such that a pressure wave originating from the contact of one particle does not propagate to other neighboring particles during the

timestep, we must choose a timestep smaller than the critical timestep defined by Rayleigh wave traveling through the solid.

When a force is applied to the surface of an elastic body, the force propagates along the surface at the wave speed first solved by John William Strutt, 3rd Baron Rayleigh⁴⁷ (when he wasn't discovering the scattering phenomenon explaining why the sky is blue or winning the Nobel prize for discovering Argon),

$$u_{\text{Ra}} = K \sqrt{\frac{G}{\rho}} \quad (14.19)$$

where, again, G is the shear modulus and ρ is the density of the elastic material. The K coefficient is a complicated function coming from Rayleigh's solution but can be approximated as⁵²

$$K = 0.1631\nu + 0.876605 \quad (14.20)$$

which is valid for realistic values of Poisson's ratio, ν , of elastic materials. From the inverse of the Rayleigh wave frequency, we can directly find a timestep for Rayleigh waves on a sphere of radius, R ,

$$\delta t_{\text{Ra}} = \frac{\pi R}{u_{\text{Ra}}} \quad (14.21)$$

When we write this for any particle, i in the ensemble (exchanging the shear for elastic modulus),

$$(\delta t_{\text{Ra}})_i = \frac{\pi R_i}{0.1631\nu_i + 0.876605} \sqrt{\frac{2(1 + \nu_i)\rho_i}{E_i}} \quad (14.22)$$

We allow for the particles in the system to have varying density, elastic modulus, and size. Therefore the critical timestep for the entire system is governed by the minimum value of any particle's Rayleigh timestep.

$$\delta t_c = \min_{\forall i} [(\delta t_{Ra})_i] \quad (14.23)$$

The ceramic materials identified for breeders have relatively high Young's moduli, on the order of 10^{10} Pa. The smallest radius will be on the order of 10^{-4} m. The ceramic density is approximately on the scale of 10^4 kg/m³. These values lead to a necessary timestep of

$$\delta t_c \propto 10^{-7}\text{s} \quad (14.24)$$

For a simulation that may last several hundreds of seconds of real time, this then requires more than 10^9 timesteps. If we have 10^4 particles in the simulation, each having their position integrated over a billion times, it becomes obvious that computational time is a major issue for our simulations of nuclear heating of ceramic breeder pebbles. If we are able to reduce the critical timestep (while perhaps decreasing the simulation time), the simulations will be much more practical for research use.

14.4.2 Critical thermal timestep

In § 5.1, we introduced the dynamics of heat transfer between contacting particles in an ensemble. As we integrate the energy of an individual particle in time, we must also ensure that energy would not propagate through a particle faster than a single timestep can capture. In analogy to the critical timestep for mechanical stability (e.g. Eq.14.21), we write for particle i ,

$$\delta t_{Bi} = \frac{\rho_i C_i V_i}{H_c} \quad (14.25)$$

where $\rho_i C_i V_i$ represents the inertial resistance to changing the temperature of T_i and the conductance, H_c represents the speed at which energy is delivered to T_i from contact conduction. Then from the definition of H_c we have given for smooth elastic spheres, this is also written as

$$\delta t_{\text{Bi}} = \frac{(4/3)\pi R_i^2 \rho_i C_i}{2k^*} \frac{R_i}{a} \quad (14.26)$$

For the material properties of lithium ceramics, as discussed for mechanical stability, we can expect

$$\frac{(4/3)\pi R_i^2 \rho_i C_i}{2k^*} \approx \frac{(10^{-4})^2 10^4 10^3}{10^0} = 10^{-1}$$

But from the requirements on Hertz theory in § 3.1, we have required that $\frac{a}{R_i} \ll 1$. Thus the timestep for stability in the energy calculation is utterly negligible compared to the mechanical stability.

Vargas and McCarthy⁶¹ make similar arguments, giving the criteria as,

$$\frac{dT_i}{T_i - T_j} \ll 1 \quad (14.27)$$

and too note that the timestep requirement for thermal calculations are orders of magnitude less restrictive than the analogous restriction of the particle dynamics.

Thus we can be confident that any timestep chosen for dynamic stability in the DEM simulation will automatically satisfy the timestep for thermal stability.

14.4.3 Simulation acceleration with scaled material properties

We rewrite Eq. 14.22 to facilitate a discussion on the parameters. Isolating each material term (neglecting the Poisson ratio) gives,

$$\delta t_c \propto R_i \times \rho_i^{1/2} \times E_i^{-1/2} \quad (14.28)$$

Part V

Future Work

Part VI

Appendices

APPENDIX A

Sphere with heat generation

We solve for the temperature distribution inside a single sphere of constant thermal conductivity with constant heat generation with a convective heat transfer boundary condition. To simplify to homogeneous boundary conditions, the temperature we solve for will be in reference to the fluid temperature, $\mathbb{T} = T - T_f$.

The energy equation in spherical coordinates with axial symmetry is,

$$\frac{1}{r} \frac{\partial^2}{\partial r^2} (r \mathbb{T}) + \frac{g}{k} = \frac{1}{\alpha} \frac{\partial \mathbb{T}}{\partial t} \quad (\text{A.1})$$

which is subject to the boundary conditions of a constant heat transfer coefficient at the surface, h ,

$$\left[\frac{\partial \mathbb{T}}{\partial r} + \frac{h}{k} \mathbb{T} \right]_{r=b} = 0 \quad (\text{A.2})$$

and an axisymmetry at the center,

$$\left[\frac{\partial \mathbb{T}}{\partial r} \right]_{r=0} = 0 \quad (\text{A.3})$$

The sphere will be at an isothermal initial temperature,

$$\mathbb{T}(r, 0) = \mathbb{T}_0 \quad (\text{A.4})$$

A.1 Transformations

We first transform the system into the nondimensional forms as defined in § 14.2,

$$\begin{aligned}\theta &= \frac{T}{T_0} \\ \rho &= \frac{r}{b} \\ \tau &= \frac{t}{b^2/\alpha}\end{aligned}$$

The energy equation is then,

$$\frac{1}{\rho} \frac{\partial^2}{\partial \rho^2} (\rho \theta) + G = \frac{\partial \theta}{\partial \tau} \quad (\text{A.5})$$

$$\text{where } G = \frac{gb^2}{kT_0}$$

The next transformation will be to introduce $U(\rho, \tau) = \rho\theta(\rho, \tau)$ as a transformation variable to simplify the differential equation of energy conservation. In the new variable formulation, the energy equation is,

$$\frac{\partial^2 U}{\partial \rho^2} + G\rho = \frac{\partial U}{\partial \tau} \quad (\text{A.6})$$

The boundary conditions are likewise transformed into,

$$\left[\frac{\partial U}{\partial \rho} + (\text{Bi} - 1) U \right]_{\rho=1} = 0 \quad (\text{A.7})$$

and

$$U|_{\rho=0} = 0 \quad (\text{A.8})$$

with initial condition

$$U(\rho, 0) = U_0 = \theta_0 r^* = r^* \quad (\text{A.9})$$

A.2 Solution

Because of the non-homogeneous form of the energy equation (due to the heat generation term), we will solve Eq. A.6 by breaking it up into two simpler problems,

1. A non-homogeneous, steady-state problem defined by $U_{ss}(r)$
2. A homogeneous, time-dependent problem defined by $U_h(r, t)$

The steady-state distribution U_{ss} is found from the solution of

$$\frac{\partial^2 U_{ss}}{\partial \rho^2} + G\rho = 0 \quad (\text{A.10})$$

subject to the same boundary condition given by Eqs. A.7,A.8. Separation and integration gives.

$$U_{ss} = -\frac{G}{6}\rho^3 + C_1\rho + C_2 \quad (\text{A.11})$$

Applying Eq. A.8 directly gives $C_2 = 0$ and, with some algebra Eq. A.7 gives,

$$C_1 = \left(\frac{G}{6} + \frac{G}{3\text{Bi}} \right)$$

valid for $\text{Bi} > 0$. Thus the steady-state distribution of our transformed variable is

$$U_{ss} = \left(\frac{G}{6} + \frac{G}{3\text{Bi}} - \rho^2 \right) \rho \quad (\text{A.12})$$

The next step is to find the homogeneous solution of

$$\frac{\partial^2 U_h}{\partial \rho^2} = \frac{\partial U_h}{\partial \tau} \quad (\text{A.13})$$

Again, subject to Eqs. A.7,A.8, but now with a modified initial condition of

$$\begin{aligned} U_{h,0} &= U_0 - U_{ss} \\ &= \left[1 - \left(\frac{G}{6} + \frac{G}{3\text{Bi}} - \rho^2 \right) \right] \rho \end{aligned} \quad (\text{A.14})$$

This is a standard homogeneous partial differential equation. The solution is of the form

$$U_h = R(\rho)\Gamma(\tau) \quad (\text{A.15})$$

The solution for Γ is given as

$$\Gamma = \exp(-\zeta^2\tau) \quad (\text{A.16})$$

The space-variable function $R(\zeta, \rho)$ satisfies the following eigenvalue problem:

$$\frac{d^2R}{d\rho^2} + \zeta^2 R = 0 \quad (\text{A.17})$$

subject to

$$R_{\rho=0} = 0 \quad (\text{A.18})$$

and

$$\left[\frac{dR}{d\rho} + (\text{Bi} - 1)R \right]_{\rho=1} = 0 \quad (\text{A.19})$$

This eigenvalue problem is a special case of the Sturm-Liouville problem. The solution for U_h can be constructed from known eigenvalue solutions,

$$U_h(\rho, \tau) = \sum_{n=1}^{\infty} c_n R(\zeta_n, \rho) \exp(-\zeta_n^2 \tau) \quad (\text{A.20})$$

Application of the initial condition gives,

$$F(\rho) = \sum_{n=1}^{\infty} c_n R(\zeta_n, \rho) \quad (\text{A.21})$$

where $F(\rho)$ is the initial condition defined from Eq A.9,

$$F(\rho) = \left[1 - \frac{G}{6} \left(1 + \frac{2}{\text{Bi}} - \rho^2 \right) \right] \rho \quad (\text{A.22})$$

The coefficients of c_n can be determined by applying the operator $\int_0^1 R(\zeta_n, \rho) d\rho$ and utilizing the orthogonality property of eigenfunctions. The coefficients are found in the form

$$c_n = \frac{1}{N(\zeta_n)} \int_0^1 R(\zeta_n, \rho') F(\rho') d\rho' \quad (\text{A.23})$$

The norm, N is a function of the eigenvalues,

$$N(\zeta_n) = \int_0^1 [R(\zeta_n, \rho)]^2 d\rho \quad (\text{A.24})$$

The eigenfunctions for Eq. A.17 are

$$R(\zeta_n, \rho) = \sin(\zeta_n \rho) \quad (\text{A.25})$$

where the eigenvalues are the root of the following transcendental equation,

$$\zeta_n \cot(\zeta_n) = -H \quad (\text{A.26})$$

the roots of which will be found numerically. The normalization integral is then solved as

$$\frac{1}{N(\zeta_n)} = 2 \frac{\zeta_n^2 + H^2}{\zeta_n^2 + H^2 + H} \quad (\text{A.27})$$

where $H = (\text{Bi} - 1)$.

We substitute the coefficients of Eq. A.23, they can be substituted back into Eq. A.20 and we have a solution for the homogeneous, transient distribution,

$$U_h(\rho, \tau) = \sum_{n=1}^{\infty} \exp(-\zeta_n^2 \tau) \frac{R(\zeta_n, \rho)}{N(\zeta_n)} \int_0^1 R(\zeta_n, \rho') F(\rho') d\rho' \quad (\text{A.28})$$

In order to explicitly express the solution, we will first set the integral equal to a function $Z(\zeta_n)$ and evaluate as,

$$\begin{aligned} Z(\zeta_n) &= \int_0^1 R(\zeta_n, \rho') F(\rho') d\rho' \\ &= \int_0^1 \sin(\zeta_n \rho') \left[1 - \left(\frac{G}{6} + \frac{G}{3\text{Bi}} - \rho'^2 \right) \right] \rho' d\rho' \\ &= \left[1 - \left(\frac{G}{6} + \frac{G}{3\text{Bi}} \right) \right] \int_0^1 \sin(\zeta_n \rho') \rho' d\rho' + \frac{G}{6} \int_0^1 \sin(\zeta_n \rho') \rho'^3 d\rho' \end{aligned} \quad (\text{A.29})$$

The two unique integrals are evaluated as

$$\begin{aligned} C_n &= \int_0^1 \sin(\zeta_n \rho') \rho' d\rho' = \frac{\sin \zeta_n - \zeta_n \cos \zeta_n}{\zeta_n^2} \\ K_n &= \int_0^1 \sin(\zeta_n \rho') \rho'^3 d\rho' = \frac{3(\zeta_n^2 - 2) \sin \zeta_n - \zeta_n(\zeta_n^2 - 6) \cos \zeta_n}{\zeta_n^4} \end{aligned}$$

Thus our Z function is

$$Z(\zeta_n) = \left[1 - \left(\frac{G}{6} + \frac{G}{3\text{Bi}} \right) \right] C_n + \frac{G}{6} K_n \quad (\text{A.30})$$

The homogeneous solution is then written in a compact form as,

$$U_h(\rho, \tau) = \sum_{n=1}^{\infty} \exp(-\zeta_n^2 \tau) \sin(\zeta_n \rho) \frac{Z(\zeta_n)}{N(\zeta_n)} \quad (\text{A.31})$$

The complete solution is then a superposition of Eq. A.12 and Eq. A.31,

$$U(\rho, \tau) = \left(\frac{G}{6} + \frac{G}{3\text{Bi}} - \rho^2 \right) \rho + \sum_{n=1}^{\infty} \exp(-\zeta_n^2 \tau) \sin(\zeta_n \rho) \frac{Z(\zeta_n)}{N(\zeta_n)} \quad (\text{A.32})$$

We now transform back to our dimensionless temperature,

$$\theta(\rho, \tau) = \left(\frac{G}{6} + \frac{G}{3\text{Bi}} - \rho^2 \right) + \sum_{n=1}^{\infty} \exp(-\zeta_n^2 \tau) \frac{\sin(\zeta_n \rho)}{\rho} \frac{Z(\zeta_n)}{N(\zeta_n)} \quad (\text{A.33})$$

A.3 Energy

We will want to compare the solution of Eq. A.33 to that of a sphere with the lumped capacitance assumption. To facilitate comparison, we look to a measure of the energy of the sphere (with radial dependence removed via integration of Eq. A.33). The energy will be nondimensionalized as,

$$E^*(\tau) = \frac{E(\tau)}{E_0} \quad (\text{A.34})$$

where E_0 is the initial energy of the sphere,

$$E_0 = \rho_r C_r V \mathbb{T}_0 \quad (\text{A.35})$$

Thus the nondimensional energy of the sphere at a given time, τ is

$$\begin{aligned} E^*(\tau) &= \int \frac{\rho_r C_r \mathbb{T}(\rho, \tau) dV}{\rho_r C_r V \mathbb{T}_0} \\ E^*(\tau) &= \frac{1}{V} \int \theta(\rho, \tau) dV \end{aligned} \quad (\text{A.36})$$

For a circle in spherical coordinates:

$$dV = r^2 \sin(\phi) dr d\phi d\theta \quad (\text{A.37})$$

For our sphere, this becomes:

$$dV = 4\pi b^3 \rho^2 d\rho = 3V \rho^2 d\rho \quad (\text{A.38})$$

The integral for dimensionless energy of our sphere is then,

$$E = 3 \int_0^1 \left[\frac{G}{6} \left(1 + \frac{2}{\text{Bi}} - \rho^2 \right) + \sum_{n=1}^{\infty} \exp(-\zeta_n^2 \tau) \frac{\sin(\zeta_n \rho)}{\rho} \frac{Z(\zeta_n)}{N(\zeta_n)} \right] \rho^2 d\rho \quad (\text{A.39})$$

This ultimately reduces to,

$$E^* = \left(\frac{G}{15} + \frac{G}{3\text{Bi}} \right) + 3 \sum_{n=1}^{\infty} \exp(-\zeta_n^2 \tau) \frac{Z(\zeta_n)}{N(\zeta_n)} C_n(\zeta_n) \quad (\text{A.40})$$

APPENDIX B

History of solid breeder design

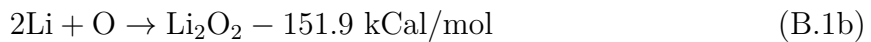
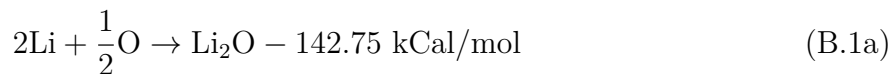
A design was proposed by Abdou et al⁷ in 1975 wherein the plasma would be surrounded by a blanket of nonmobile, solid lithium. To exist in solid form at high temperatures, pure lithium, which has a melting temperature of only about 180 °C, must be combined with refractory materials (melting temperatures >1000 °C). To date, most parties researching solid breeder blankets have settled on lithium orthosilicate (Li_4SiO_4) or lithium metatitanite (Li_2TiO_3) as candidate ceramics.

As nuclear energy is deposited into the solid breeder, large thermal gradients in the solid lithiated ceramics will induce thermal stresses across large characteristic lengths. Avoiding thermal stress has led to most solid breeder designs implementing packed beds of small, spherical (or near-spherical) pebbles.^{14, 40, 43, 56} Moreover, tritium diffusion and release considerations for solid lithium ceramic support the choice of short characteristic lengths of individual pebbles. From an engineering design standpoint, the choice of packed bed has other desirable characteristics. For instance, the ensemble of small spherical pebbles can be filled into many complex shapes with relatively uniform porosity. The uniform packing of spheres permits a well-distributed flow of purge gas for tritium extraction.

The advantages of the pebble bed design include ease of uniformly assembling the solid into complex geometries, ease of tritium extraction from the porous bed via an interstitial purge of helium, and with the small size of pebbles being more resilient to thermal stresses than a solid brick of lithiated ceramic.[?]

Lithium oxide had been considered because of its favorable lithium density, among other attractive features, though the reaction of lithium with elemental oxygen is a concern. Pure

lithium reacts with oxygen exothermically in reactions such as



Of primary concern in lithium fires is the peak flame temperature. This will determine, to a large extent, whether many radioactive species become air-borne by vaporization. The flame temperature depends on many variables. Some investigations found it to be about 2500 K which would cause some materials to melt but not vaporize. [cite Abdou's class notes?]

REFERENCES

- [1] Ali Abou-Sena, Alice Y. Ying, and Mohamed A Abdou. Effective Thermal Conductivity of Lithium Ceramic Pebble Beds for Fusion Blankets: A Review. *Fusion Science and Technology*, 47(4):1094–1100, 2005.
- [2] Zhiyong An, Alice Ying, and Mohamed A Abdou. Numerical characterization of thermo-mechanical performance of breeder pebble beds. *Journal of Nuclear Materials*, 367-370:1393–1397, 2007.
- [3] Ratna Kumar Annabattula, Yixiang Gan, Shuo Zhao, and Marc Kamlah. Mechanics of a crushable pebble assembly using discrete element method. *Journal of Nuclear Materials*, 430(1-3):90–95, November 2012.
- [4] G.K. Batchelor and R.W. O'Brien. Thermal or Electrical Conduction Through a Granular Material. *Proceedings of the Royal Society of London. Series A, Mathematical and Physical Sciences*, 355(1682):313–333, 1977.
- [5] Sofiane Benyahia, Madhava Syamlal, and Thomas J. O'Brien. Extension of Hill–Koch–Ladd drag correlation over all ranges of Reynolds number and solids volume fraction. *Powder Technology*, 162(2):166–174, March 2006.
- [6] Nv Brilliantov, F Spahn, Jm Hertzsch, and T Pöschel. Model for collisions in granular gases. *Physical review. E, Statistical physics, plasmas, fluids, and related interdisciplinary topics*, 53(5):5382–5392, May 1996.
- [7] Chang-sheng Bu, Dao-yin Liu, Xiao-ping Chen, Cai Liang, Yu-feng Duan, and Lun-bo Duan. Modeling and Coupling Particle Scale Heat Transfer with DEM through Heat Transfer Mechanisms. *Numerical Heat Transfer, Part A: Applications*, 64(1):56–71, July 2013.
- [8] L. Bühler and Jörg Reimann. Thermal creep of granular breeder materials in fusion blankets. *Journal of Nuclear Materials*, 307-311:807–810, December 2002.
- [9] P. Calderoni, Alice Ying, Tomas Sketchley, and Mohamed A Abdou. Experimental study of the interaction of ceramic breeder pebble beds with structural materials under thermo-mechanical loads. *Fusion Engineering and Design*, 81(1-7):607–612, 2006.
- [10] Bodhisattwa Chaudhuri, Fernando J. Muzzio, and M. Silvina Tomassone. Modeling of heat transfer in granular flow in rotating vessels. *Chemical Engineering Science*, 61(19):6348–6360, October 2006.
- [11] K Chen, A. Harris, J. Draskovic, and P. Schiffer. Granular fragility under thermal cycles. *Granular Matter*, 11(4):237–242, May 2009.
- [12] G.J. Cheng, A.B. Yu, and P. Zulli. Evaluation of effective thermal conductivity from the structure of a packed bed. *Chemical Engineering Science*, 54(4199):4209, 1999.

- [13] Seungyon Cho, Mu-Young Ahn, Duck Hoi Kim, Eun-Seok Lee, Sunghwan Yun, Nam Zin Cho, and Ki Jung Jung. Current status of design and analysis of Korean Helium-Cooled Solid Breeder Test Blanket Module. *Fusion Engineering and Design*, 83(7-9):1163–1168, December 2008.
- [14] Seungyon Cho, Mu-Young Ahn, In-Keun Yu, Yi-Hyun Park, Duck Young Ku, Sang-Jin Lee, Han-Ki Yoon, and Tae-Gyu Kim. R&D progress of Korean HCSB TBM. *Fusion Engineering and Design*, 87(5-6):386–391, August 2012.
- [15] Peter A Cundall and Otto D L Strack. A discrete numerical model for granular assemblies. *Geotechnique*, 29(1):47–65, 1979.
- [16] Francesco Paolo Di Maio, G. Dell’Orco, R. Giammusso, A Malavasi, I. Ricapito, A. Tincaani, and G. Vella. Experimental tests and thermo-mechanical analyses on the HEX-CALIBER mock-up. *Fusion Engineering and Design*, 83(7-9):1287–1293, December 2008.
- [17] Francesco Paolo Di Maio, R. Giammusso, and G. Vella. On the hyperporous non-linear elasticity model for fusion-relevant pebble beds. *Fusion Engineering and Design*, 85(7-9):1234–1244, 2010.
- [18] Alberto Di Renzo and Francesco Paolo Di Maio. Comparison of contact-force models for the simulation of collisions in DEM-based granular flow codes. *Chemical Engineering Science*, 59(3):525–541, February 2004.
- [19] Thibaut Divoux, Hervé Gayvallet, and Jean-Christophe Géminard. Creep Motion of a Granular Pile Induced by Thermal Cycling. *Physical Review Letters*, 101(14):148303, October 2008.
- [20] Mikio Enoda, Y. Kosaku, Toshihisa Hatano, T. Kuroda, N. Miki, T. Honma, Masato Akiba, S. Konishi, H. Nakamura, Y. Kawamura, S. Sato, K. Furuya, Y. Asaoka, and Kunihiko Okano. Design and technology development of solid breeder blanket cooled by supercritical water in Japan. *Nuclear Fusion*, 43:1837–1844, 2003.
- [21] Y.T. Feng and K. Han. An accurate evaluation of geometric view factors for modelling radiative heat transfer in randomly packed beds of equally sized spheres. *International Journal of Heat and Mass Transfer*, 55(23-24):6374–6383, November 2012.
- [22] Yixiang Gan and Marc Kamlah. Identification of material parameters of a thermo-mechanical model for pebble beds in fusion blankets. *Fusion Engineering and Design*, 82(2):189–206, February 2007.
- [23] Yixiang Gan and Marc Kamlah. Thermo-mechanical analysis of pebble beds in HELICA mock-up experiments. *Fusion Engineering and Design*, 83(7-9):1313–1316, December 2008.
- [24] Yixiang Gan and Marc Kamlah. Thermo-mechanical analyses of HELICA and HEX-CALIBER mock-ups. *Journal of Nuclear Materials*, 386-388:1060–1064, April 2009.

- [25] Yixiang Gan and Marc Kamlah. Discrete element modelling of pebble beds: With application to uniaxial compression tests of ceramic breeder pebble beds. *Journal of the Mechanics and Physics of Solids*, 58(2):129–144, February 2010.
- [26] Yixiang Gan and Marc Kamlah. Thermo-mechanical modelling of pebble bed-wall interfaces. *Fusion Engineering and Design*, 85(1):24–32, January 2010.
- [27] Yixiang Gan, Marc Kamlah, and Jörg Reimann. Computer simulation of packing structure in pebble beds. *Fusion Engineering and Design*, 85(10-12):1782–1787, 2010.
- [28] Paul J Gierszewski. Review of properties of lithium metatitanate. *Fusion Engineering and Design*, 39-40:739–743, September 1998.
- [29] Klemens Gruber. *Sediment transport in open channel flows - Experimental investigation and numerical simulation of local scour development downstream of a weir*. PhD thesis, 2012.
- [30] H. Grubmuller, H. Heller, A Windemuth, and K. Schulten. Generalized verlet algorithm for efficient molecular dynamics simulations with long-range interaction. *Molecular Simulation*, 6:121–142, 1991.
- [31] C.P. Jeffreson. Prediction of Breakthrough Curves in Packed Beds: 1. Applicability of Single Parameter Models. *American Institute of Chemical Engineers*, 18(2):409–416, March 1972.
- [32] KL Johnson. *Contact Mechanics*. 1985.
- [33] Christoph Kloss and Christoph Goniva. LIGGGHTS - Open Source Discrete Element Simulations of Granular Materials Based on LAMMPS. *Supplemental Proceedings: Materials Fabrication, Properties, Characterization, and Modeling*, 2:781–788, 2011.
- [34] Christoph Kloss, Christoph Goniva, Alice Hager, Stefan Amberger, and Stefan Pirker. Models, algorithms and validation for opensource DEM and CFD-DEM. *Progress in Computational Fluid Dynamics*, 12(2/3):140–152, 2012.
- [35] Donald L Koch and Reghan J. Hill. Inertial Effects in Suspension and Porous-Media Flows. *Annual Review of Fluid Mechanics*, 33(1):619–647, January 2001.
- [36] H. Kruggel-Emden, M. Sturm, S. Wirtz, and V. Scherer. Selection of an appropriate time integration scheme for the discrete element method (DEM). *Computers & Chemical Engineering*, 32(10):2263–2279, October 2008.
- [37] P A Langston, U Tlrlzon, and D M Heyes. Discrete element simulation of granular flow in 2D and 3D hoppers: dependence of discharge rate and wall stress on particle interactions. *Chemical Engineering Science*, 50(6):967–987, 1995.
- [38] Jintang Li and D.J. Mason. A computational investigation of transient heat transfer in pneumatic transport of granular particles. *Powder Technology*, 112(3):273–282, October 2000.

- [39] Zi Lu. *Numerical Modeling and Experimental Measurement of the Thermal and Mechanical Properties of Packed Beds*. PhD thesis, University of California Los Angeles, 2000.
- [40] J D Lulewicz and N. Roux. Fabrication of Li₂TiO₃ pebbles by the extrusion–spheronisation–sintering process. *311*:803–806, 2002.
- [41] Hernán Makse, Nicolas Gland, David Johnson, and Lawrence Schwartz. Granular packings: Nonlinear elasticity, sound propagation, and collective relaxation dynamics. *Physical Review E*, 70(6):061302, December 2004.
- [42] Hernán Makse, David Johnson, and Lm Schwartz. Packing of compressible granular materials. *Physical review letters*, 84(18):4160–3, May 2000.
- [43] D. Mandal, D. Sathiyamoorthy, and V. Govardhana Rao. Preparation and characterization of lithium–titanate pebbles by solid-state reaction extrusion and spherodization techniques for fusion reactor. *Fusion Engineering and Design*, 87(1):7–12, January 2012.
- [44] G Piazza, Jörg Reimann, E Günther, Regina Knitter, N. Roux, and J D Lulewicz. Characterisation of ceramic breeder materials for the helium cooled pebble bed blanket. *Journal of Nuclear Materials*, 307-311(0):811–816, December 2002.
- [45] Steve Plimpton. Fast Parallel Algorithms for Short-Range Molecular Dynamics. *Journal of Computational Physics*, 117(1):1–19, March 1995.
- [46] Y Poitevin, Lorenzo Boccaccini, M Zmitko, I Ricapito, J.F. Salavy, E. Diegele, F. Gabriel, E. Magnani, H. Neuberger, R. Lässer, and L. Guerrini. Tritium breeder blankets design and technologies in Europe: Development status of ITER Test Blanket Modules, test & qualification strategy and roadmap towards DEMO. *Fusion Engineering and Design*, 85(10-12):2340–2347, December 2010.
- [47] J. W. S. Rayleigh. On waves propagated along the plane surface of an elastic solid. *Proceedings of the London Mathematical Society*, 17:4–11, 1885.
- [48] Jörg Reimann, Lorenzo Boccaccini, Mikio Enoeda, and Alice Ying. Thermomechanics of solid breeder and Be pebble bed materials. *Fusion Engineering and Design*, 61-62:319–331, November 2002.
- [49] Jörg Reimann and S Hermsmeyer. Thermal conductivity of compressed ceramic breeder pebble beds. *Fusion Engineering and Design*, 61-62:345–351, November 2002.
- [50] Jörg Reimann and G. Wörner. Thermal creep of Li₄SiO₄ pebble beds. *Fusion Engineering and Design*, 58-59:647–651, November 2001.
- [51] J. Shafer, S Dippel, and D. E. Wolf. Force Schemes in Simulations of Granular Materials. *Journal de Physique I*, 6(1):5–20, January 1996.

- [52] Y. Sheng, C.J. Lawrence, B.J. Briscoe, and C. Thornton. Numerical studies of uniaxial powder compaction process by 3D DEM. *Engineering Computations*, 21(2/3/4):304–317, 2004.
- [53] Leonardo Silbert, Deniz Ertaş, Gary Grest, Thomas Halsey, and Dov Levine. Geometry of frictionless and frictional sphere packings. *Physical Review E*, 65(3):031304, February 2002.
- [54] Leonardo E. Silbert, Deniz Ertaş, Gary Grest, Thomas Halsey, Dov Levine, and Steven Plimpton. Granular flow down an inclined plane: Bagnold scaling and rheology. *Physical Review E*, 64(5):051302, October 2001.
- [55] Hisashi Tanigawa, Yuichiro Tanaka, and Mikio Enoeda. Packing behaviour of a Li₂TiO₃ pebble bed under cyclic loads. *Journal of Nuclear Materials*, 417(1-3):2010–2012, December 2010.
- [56] Kunihiko Tsuchiya, Hiroshi Kawamura, Katsuhiro Fuchinoue, Hiroshi Sawada, and Kazutoshi Watarumi. Fabrication development and preliminary characterization of Li₂TiO₃ pebbles by wet process. *Journal of Nuclear Materials*, 258-263:1985–1990, October 1998.
- [57] Y. Tsuji, T. Kawaguchi, and T. Tanaka. Discrete particle simulation of two-dimensional fluidized bed. *Powder Technology*, 77(1):79–87, October 1993.
- [58] Y. Tsuji, T. Tanaka, and T. Ishida. Lagrangian numerical simulation of plug flow of cohesionless particles in a horizontal pipe. *Powder Technology*, 71(3):239–250, September 1992.
- [59] Jon T. Van Lew. *Transient Heat Delivery, Storage Process, and Optimization of a Packed Bed Thermocline Thermal Energy Storage System*. Master's thesis, University of Arizona, 2010.
- [60] Jon T. Van Lew, Alice Ying, and Mohamed Abdou. A discrete element method study on the evolution of thermomechanics of a pebble bed experiencing pebble failure. *Fusion Engineering and Design*, 89(7-8):1151–1157, October 2014.
- [61] Watson L Vargas and J J Mccarthy. Heat Conduction in Granular Materials. *AICHE Journal*, 47(5), 2001.
- [62] Watson L Vargas and J J Mccarthy. Conductivity of granular media with stagnant interstitial fluids via thermal particle dynamics simulation. *International Journal of Heat and Mass Transfer*, 45(24):4847–4856, November 2002.
- [63] Watson L Vargas and J J Mccarthy. Thermal expansion effects and heat conduction in granular materials. *Physical Review E*, 76(4):1–8, October 2007.

- [64] Jin Tao Wu, Yu Qiang Dai, Ze Wu Wang, and Feng Xia Liu. Study on the Heat Transfer in Granular Materials by DEM. *Advanced Materials Research*, 233-235:2949–2954, May 2011.
- [65] Ben Xu, Peiwen Li, and Cho Lik Chan. Extending the validity of lumped capacitance method for large Biot number in thermal storage application. *Solar Energy*, 86(6):1709–1724, June 2012.
- [66] H. Zhang and Hernán Makse. Jamming transition in emulsions and granular materials. *Physical Review E*, 72(1):011301, July 2005.
- [67] H.W. Zhang, Q. Zhou, H.L. Xing, and H. Muhlhaus. A DEM study on the effective thermal conductivity of granular assemblies. *Powder Technology*, 205(1-3):172–183, January 2011.
- [68] Shuo Zhao. *Multiscale Modeling of Thermomechanical Properties of Ceramic Pebbles*. PhD thesis, Karlsruhe Institute of Technology, 2010.
- [69] Shuo Zhao, Yixiang Gan, and Marc Kamlah. Failure initiation and propagation of Li₄SiO₄ pebbles in fusion blankets. *Fusion Engineering and Design*, 88(1):8–16, January 2013.
- [70] Shuo Zhao, Yixiang Gan, Marc Kamlah, Tobias Kennerknecht, and Rolf Rolli. Influence of plate material on the contact strength of Li₄SiO₄ pebbles in crush tests and evaluation of the contact strength in pebble-pebble contact. *Engineering Fracture Mechanics*, 100:28–37, March 2013.
- [71] Z.Y. Zhou, A.B. Yu, and P. Zulli. Particle scale study of heat transfer in packed and bubbling fluidized beds. *AICHE Journal*, 55(4):868–884, April 2009.
- [72] H.P. Zhu, Z.Y. Zhou, R.Y. Yang, and A.B. Yu. Discrete particle simulation of particulate systems: Theoretical developments. *Chemical Engineering Science*, 62(13):3378–3396, July 2007.
- [73] H.P. Zhu, Z.Y. Zhou, R.Y. Yang, and A.B. Yu. Discrete particle simulation of particulate systems: A review of major applications and findings. *Chemical Engineering Science*, 63(23):5728–5770, December 2008.